Investigating the influence of particle dispersion on the electromechanical properties of nanoparticle-based conductive polymer composites

by

Tyler Bryce Albright

B.S., Kansas State University, 2017

AN ABSTRACT OF A DISSERTATION

submitted in partial fulfillment of the requirements for the degree

DOCTOR OF PHILOSOPHY

Alan Levin Department of Mechanical and Nuclear Engineering
Carl R. Ice College of Engineering

KANSAS STATE UNIVERSITY
Manhattan, Kansas

2022

Abstract

Nanoparticle-based conductive polymer composites (CPCs) are an attractive solution to many engineering problems due to their advantageous electromechanical and structural properties. CPC-based strain and fatigue sensing transducers have generated tremendous interest in recent decades, especially in the fields of smart materials and structural health monitoring. The viability of deploying CPC transducers for strain and fatigue sensing has been demonstrated repeatedly, yet a lack of fundamental understanding of underlying electromechanical phenomena, such as percolation, piezoresistivity, and the influence of preparation methods on such phenomena, has limited the widespread adoption of CPC-based transducers in real-world applications. An attempt to reduce necessary experimental characterization efforts, the task of predicting electromechanical properties of CPC-based transducers for engineering applications presents a unique challenge considering the multi-scale nature of nanoparticle-based CPCs. Traditional bulk property prediction models can effectively describe basic CPC behaviors, but the stochastic nature of CPC materials requires more complex models to elucidate the relationship between nanoparticle dispersion and CPC electromechanical characteristics at various length scales. In this dissertation, the influence of stochastic particle dispersion on the electromechanical properties of spherical nanoparticle-based CPCs is investigated through a combination of multi-scale stochastic modeling and experimental validation. The development of a high-fidelity, numerical, stochastic modeling algorithm, capable of generating representative volume elements (RVEs) for electromechanical interrogation, with nanoscale feature resolution and primary particle agglomeration control is discussed in great detail. Investigations of various algorithms for efficiently populating RVEs with primary particles are presented. The need for and efficacy of spanning multiple length scales (nanometer to millimeter) via the aforementioned

stochastic model placement algorithms is explored. CPC thin film samples, composed of epoxy and carbon black, are experimentally manufactured via spin coating. The translucent properties of the spun thin films are favorable for optical microscopy imaging, which is then conducted to validate and improve stochastic model fidelity. Quantification of experimental CPC mixture dispersion is achieved via post-processing of optical micrographs. Statistical analysis of agglomeration shape and size descriptors (average agglomerate area, roundness, circularity, etc.) from stochastically generated RVE images are directly compared to experimental datasets, and model parameter tuning methods are presented. Bulk CPC samples are electromechanically characterized via uniaxial tensile and fatigue testing. Stochastically generated RVEs are subjected to simulated uniaxial strain, and changes in the resulting simulated random resistor networks are interrogated by applying Kirchhoff's Laws and the theory of tunneling conductivity. Analytical models for predicting the piezoresistive response of spherical particle CPC volumes under uniaxial compression are adapted to agree with experimentally realized behaviors. Results from simulated, analytically modeled, and experimentally derived datasets are compared. The implications of this research, avenues for improvement, and recommendations for future work are discussed.

Investigating the influence of particle dispersion on the electromechanical properties of nanoparticle-based conductive polymer composites

by

Tyler Bryce Albright

B.S., Kansas State University, 2017

A DISSERTATION

submitted in partial fulfillment of the requirements for the degree

DOCTOR OF PHILOSOPHY

Alan Levin Department of Mechanical and Nuclear Engineering
Carl R. Ice College of Engineering

KANSAS STATE UNIVERSITY
Manhattan, Kansas

2022

Approved by:

Major Professor
Jared D. Hobeck, Ph.D.

Copyright

Abstract

Nanoparticle-based conductive polymer composites (CPCs) are an attractive solution to many engineering problems due to their advantageous electromechanical and structural properties. CPC-based strain and fatigue sensing transducers have generated tremendous interest in recent decades, especially in the fields of smart materials and structural health monitoring. The viability of deploying CPC transducers for strain and fatigue sensing has been demonstrated repeatedly, yet a lack of fundamental understanding of underlying electromechanical phenomena, such as percolation, piezoresistivity, and the influence of preparation methods on such phenomena, has limited the widespread adoption of CPC-based transducers in real-world applications. An attempt to reduce necessary experimental characterization efforts, the task of predicting electromechanical properties of CPC-based transducers for engineering applications presents a unique challenge considering the multi-scale nature of nanoparticle-based CPCs. Traditional bulk property prediction models can effectively describe basic CPC behaviors, but the stochastic nature of CPC materials requires more complex models to elucidate the relationship between nanoparticle dispersion and CPC electromechanical characteristics at various length scales. In this dissertation, the influence of stochastic particle dispersion on the electromechanical properties of spherical nanoparticle-based CPCs is investigated through a combination of multi-scale stochastic modeling and experimental validation. The development of a high-fidelity, numerical, stochastic modeling algorithm, capable of generating representative volume elements (RVEs) for electromechanical interrogation, with nanoscale feature resolution and primary particle agglomeration control is discussed in great detail. Investigations of various algorithms for efficiently populating RVEs with primary particles are presented. The need for and efficacy of spanning multiple length scales (nanometer to millimeter) via the aforementioned

stochastic model placement algorithms is explored. CPC thin film samples, composed of epoxy and carbon black, are experimentally manufactured via spin coating. The translucent properties of the spun thin films are favorable for optical microscopy imaging, which is then conducted to validate and improve stochastic model fidelity. Quantification of experimental CPC mixture dispersion is achieved via post-processing of optical micrographs. Statistical analysis of agglomeration shape and size descriptors (average agglomerate area, roundness, circularity, etc.) from stochastically generated RVE images are directly compared to experimental datasets, and model parameter tuning methods are presented. Bulk CPC samples are electromechanically characterized via uniaxial tensile and fatigue testing. Stochastically generated RVEs are subjected to simulated uniaxial strain, and changes in the resulting simulated random resistor networks are interrogated by applying Kirchhoff's Laws and the theory of tunneling conductivity. Analytical models for predicting the piezoresistive response of spherical particle CPC volumes under uniaxial compression are adapted to agree with experimentally realized behaviors. Results from simulated, analytically modeled, and experimentally derived datasets are compared. The implications of this research, avenues for improvement, and recommendations for future work are discussed.

Table of Contents

List of Figures

Acknowledgements

First, I would like to give my sincerest thanks to Dr. Jared D. Hobeck for his guidance, advisement, mentorship, and friendship. The time, energy, and patience you spent on me have taught me invaluable lessons have enabled me to become a more competent, capable, and caring person. It has truly been a pleasure working with and learning from you. I would also like to thank Dr. Gurpreet Singh, Dr. Youqi Wang, Dr. Suprem Das, and Dr. Christine Aikens for serving on my Ph.D. committee and for offering their experiences and perspectives in developing my dissertation. I would like to thank the many teachers and professors over the years that have challenged me academically and instilled in me the value of dedicating oneself to lifelong learning. A special thank you to Dr. Kevin Wanklyn and Dr. Gurpreet Singh for seeing the potential in me for post-graduate scholastic achievement, and for urging me to join the graduate program.

I would like to thank the Kansas State University, Carl R. Ice College of Engineering for funding the research presented in this dissertation. I would also like to thank Professor Greg Spaulding for the guidance/experiences shared over the years, and for being a joy to work with in my teaching assistantship assignments.

I would like to thank the undergraduate students who contributed to the research presented in this dissertation. Josiah Satzler – an undergraduate mechanical engineering student who was a member of the Multifunctional Structures Lab (MSL) from 2018-2020 and contributed to experimental research detailed in Chapters 3 and 4. Timber Hinson – an undergraduate mechanical engineering student who became a member of the MSL in 2019 and designed, built, and tested the spray apparatus detailed in Chapter 4 in collaboration with Josiah. Nick Mignano – an undergraduate mechanical engineering student who became a member of the

MSL in the summer of 2019 and helped develop the early film characterization experimental efforts detailed in Chapter 4. Anthony Lopez – an undergraduate mechanical engineering student who became a member of the MSL in 2020 and contributed to the development of batch processing codes for microscopy image analysis. It was a joy getting to work with you all, and I am grateful for the time and energy you dedicated to our research projects.

Thanks to all of my friends and colleagues in the Mechanical and Nuclear Engineering Department, especially my lab mates in the MSL. A special thank you to my friend and colleague Dr. Khalid Abdelaziz, with whom I shared many late nights in the lab and trying academic experiences.

Finally, this dissertation would not be complete without a special thank you to my friends and family. I would not have been capable of getting this far without them. Through their endless love and support I found renewed strength when faced with tough times. Thank you to the Steele's and Unruh's for accepting me into their families, and for investing time and energy into my development as a scholar and as a person. I would like to thank my sister, Emma Andersen, for always being there to cheer me up and to motivate me to be the best version of myself. I would like to give a special thanks to my father, Andrew Albright, for instilling in me the values of hard work and dedication to one's responsibilities, especially those responsibilities one has to his family and loved ones. Also, a special thanks to my mother, Jenifer Albright, for teaching me how to be compassionate, caring, creative, and to understand the value of building deep and meaningful relationships with others. I am forever indebted to you two, and cannot express how thankful I am to have been blessed with such fantastic parents.

Dedication

~ To my friends and family ~

CHAPTER 1

INTRODUCTION AND LITERATURE REVIEW

1.1. Introduction

Fiber-reinforced-polymer composites (FRPC) have become commonplace across many industries, and likewise their implementation has become a regularly exercised tool in the structural engineer's toolbox. The realization of composite material advantages dates to World War II with the invention of fiber-reinforced plastic wound rocket motors [1]. Since its inception, the idea of advanced composite structures has developed into an invaluable resource for high-performance and weight-critical applications. Tailorability of FRPC structures allows designers to optimize structural configurations to meet application-specific needs such as maximizing strength-to-weight ratio, tuning thermal and electrical conductivities, and improving corrosion resistivity. Manipulation of the physical properties of a composite structure can be achieved by varying the contents thereof. A vast number of configurations have been utilized across numerous industries: Including but not limited to aerospace, automotive, agricultural, and household items including the viewing window on a microwave oven. While the benefits of these seemingly unlimited configurations have been regularly utilized, the scientific validation of each product follows an exceptionally unique process. This is due to the fact that slight variations

in the build process, materials used, and environmental factors can greatly affect the performance of the resulting composite structure. A better understanding of composites at the micro and nanoscale is essential for more accurate prediction and tailoring of their macroscale characteristics.

1.2. SHM of aerospace composites

In a futuristic world, engineering materials will be able to withstand any cyclic loading, changes in environmental stresses, and most traumatic damaging events. These advanced structures will fail only in limited and the most extreme circumstances. In the event of these catastrophic failures, how will we know that the structure has been compromised? How will the health of a structure be assessed and realized prior to its inevitable ultimate structural failure? These conceptual questions can also be asked of composite structural designs of the present. To better understand the general physics behind composite failure modes, modern research is focusing on the detection of composite defects and the determination of their influence on the strength and life expectancy of the structure. This field of research is commonly referred to as structural health monitoring (SHM). SHM has been a popular topic both in industry and academia over the past few decades. While the benefits of composite designs are numerous, their complex mechanical response to fatigue gives rise to engineering uncertainties that are often overcompensated for via mechanical fasteners and/or additional laminate layers. SHM research aims to supplant those overcompensations with informed analytics on the integrity of the structure in question without compromising the structure via obtrusive sensor networks.

Like the development of well-understood and nearly unified metallic failure mode analysis, the development of a unified composite failure analysis will require extensive empirical data to accompany theoretical interpretation and modeling. Research has uncovered a large

variety of methods for collecting and analyzing useful data to inform failure models. Identification and quantification of barely visible damage (BVID) has been heavily researched in the aerospace industry where certification of primary structures is closely monitored. Non-destructive techniques (NDT) such as acoustic emission and electromagnetic inspection can precisely and consistently locate damage in composite materials. These systems are often very large, and take a significant amount of time to perform their inspection. The result of these limitations is an increasing cost of performing routine inspections during in-service life of these major primary structures. Subsequently, service-life inspection is performed so sparsely that it isn't guaranteed that a major defect will be observed and corrected prior to failure. The cost of taking a structure out of service for inspection could be mitigated by the implementation of an on-board SHM system that could perform similar BVID inspection while the structure is in service. Many SHM systems and sensing technologies have been proposed in the literature for this purpose [2]. A high-level overview of current and common SHM systems will be outlined in the following sections. While each system is inherently different based on the principle of its operation, one commonality should be acknowledged when comparing these vastly different systems: The systems do not measure damage directly, instead they measure physical qualities whose change over time can be correlated to damage accumulation.

1.3. Types of SHM transducers

The information of most value to a structural technician or service manager are (i) the remaining life of a structure, (ii) the probability of structural failure during normal operating conditions, and (iii) the location and severity of existing damage in a structure. It is impossible to directly measure (i) or (ii), but the quantification of these properties can be achieved with knowledge of (iii). Research in the area of structural degradation sensing has developed greatly

in the last few years. Still, the challenge of engineering a precise and unobtrusive SHM system remains. While controlled laboratory experimentation can provide insight into simple static and fatigue failure modes, degradation of composite structures deployed in the field cannot be fully understood without acquiring working-life empirical evidence.

The potential effectiveness of existing SHM methods has been demonstrated extensively in the literature. Unfortunately, commercial development of many of these SHM techniques has been hindered by their complexity of implementation and their sensitivity to extraneous factors such as temperature, vibration, etc. Generally, the complexity of the SHM system is dependent on the complexity of the physical measurement acquired from transducers fixed on or inside the structure being monitored. This complexity can arise from manufacturing methods, data processing requirements, data acquisition and signal generation requirements, structural performance impacts, environmental considerations, and other factors. For example, it has been shown that nondestructive testing (NDT) techniques such as lamb-wave propagation can accurately locate and characterize damage within composite structural components [3]. In aircraft structural design, weight is a dominating engineering requirement that is consequently tracked down to the last nut and hi-lock bolt. To embed a SHM system on a composite aircraft skin panel, the panel must be equipped with transducers as well as their respective wire leads and data acquisition units. Embedding such transducers and leads to allow for the SHM system's deployment in an aircraft skin panel would drastically change current manufacturing processes. Also, the effect of the system's contribution to the overall structural integrity of the panel must be considered, especially around bonded composite joints where delamination is most probable [1].

1.3.1. Piezoelectric wafer sensors

Piezoelectric wafer sensors (PWS) have proven to be an effective tool for quantifying changes in structural integrity. Giurgiutiu describes the deployment of PWS for SHM as following three main paths: (a) modal analysis and transfer function; (b) electromechanical E/M impedance; (c) wave propagation [4]. Each mode uses a varying approach to record a structural response signature from a PWS coupled to the structure. By applying bending stress to a PWS, an electrical potential is created about the transducer that can be directly measured. By adhering a PWS to a structure, it is assumed that the PWS and structure will have a coupled mechanical response. Through this assumption, one can quantify the dynamic structural response of the host structure through the response of the transducers output voltage measurements. By observing this response over time, variations in the PWS response indicate changes in structural integrity and possible damage accumulation.

There are multiple methods by which PWS have been used in practice. In Pitch-Catch sensing systems, a high frequency voltage is applied to a PWS adhered to a structure, resulting in the propagation of guided surface waves through the structure, otherwise known as Lamb Waves [4]. A separate PWS, coupled at a known distance from the excitation site, then measures and characterizes this wave. Further reading on damage indexing and statistical methods for pitch-catch systems can be found in Giurgiutiu's comprehensive text [4]. An alternative to this forced excitation method is passive monitoring. In passive monitoring systems excitations of the structure due to in-service conditions take the place of excitation sensors. For passive monitoring systems to be effective, the loading of the structure in question must be cyclic and of consistent amplitude to produce useful data for damage indexing. De Souza Rabelo *et al.* demonstrated passive monitoring techniques using PWS [5]. Studies by Nasrollahi *et al.* explored the potential

of coupled piezoelectric transducer systems that combine active and passive techniques [6]. The resulting system was shown to provide accurate damage indexing and precise damage triangulation ability while requiring large computational resources and application specific frequency operating ranges. Furthermore, it is important to note that measurements in this study were obtained at static states of mean applied loads.

In PWS-based SHM systems, the distribution of sensor elements is subject to the researchers discretion. Research has been performed on both surface mounted PWS systems as well as embedded PWS systems. Tang *et al.* found that glass-fiber reinforced polymer composite (GFRPC) specimens under axial loading equipped with embedded PWS experienced stress concentrations and subsequent failure near the transducer leads. This failure was determined to be the result of matrix voids caused by the obtrusive nature of the transducers, which ranged from 0.19mm to 1.14mm in through thickness [7].

1.3.2. Optical sensors

The development of optical sensors in the past two decades has spawned great interest in the development of strain sensing transducers for SHM application. Fiber Bragg Grating (FBG) sensors were developed for this purpose and have been proven effective in practical SHM applications. These sensors operate under the principles of light-wave propagation utilizing the diffractive properties of varying elements. These fibers can be manufactured continuously with the ability to multiplex incoming data. The reflected light waves, known as the Bragg signal, are recorded and compared to the signature of a pristine and pre-strained sample. The shift in the returned signal can then be converted directly into a localized strain measurement. For a detailed explanation of FBG sensor operating principles, the readers are directed to the works of Kersey *et al* [8].

By embedding FBG sensors into a structure, one can measure in situ strain in multiple locations using a single fiber element. This makes FBG sensors a favorable SHM choice due to the lack of mechanical splicing and coupling required during manufacture. High electrical isolation, total electrical passivity, environmental stability, and non-distance restricted measurement capabilities make FBG systems favorable for many applications [9]. One unfavorable characteristic of this system is the equipment and signal processing required for such strain quantification, especially at high frequencies [1]. Regardless, these embedded FBG systems have proven effective for monitoring quasi-static civil engineering structures. While embedded FBG systems have made their way into civil structures, these systems haven't yet been adopted by FRPC using industries. A major limitation in FBG development for SHM is the obtrusive nature of FBG sensors. Typical telecom optical fiber diameters range from 120 to 250 micrometers. Embedding these FBG transducers in FRPC results in matrix pockets about the transducer [10]. More recent studies have shown the use of specialty FBG transducers that have been constructed with diameters as small as 56 micrometers [11]. These specialty fibers are more difficult to manufacture and consequently more expensive than traditional FBG transducers. Another important factor in the aerospace industry's hesitance to adopt FBG transducer systems is the emphasis on weight reduction in all areas of engineering aerospace structures. While the sensors themselves are extremely lightweight, their obtrusive nature drives primary structure weight increases to compensate for stress concentrations about the embedded system.

1.3.3. Self-sensing composites

In response to the widespread adoption of FRPC structures across multiple industries, SHM research has been focused on building a SHM system that utilizes the unique characteristics of common composite constituents, such as carbon fibers. The electromechanical

characteristics of carbon fibers have been exploited for measuring strain in CFRP structures. Conductive and piezoresistive carbon fibers within a composite can be manufactured so as to create conductive networks spanning the structure, typically interrogated via integrated surface electrodes. Piezoresistivity is defined as the resistivity change in a material when mechanical strain is applied. Wang and Chung observed this phenomenon in a 24-lamina quasi-isotropic carbon FRPC layup. They found that compressing the structure resulted in measurable through thickness resistivity change in both reversible and irreversible forms [12].

One of the most dangerous forms of FRPC failure is matrix crack propagation, commonly referred to as delamination. Delamination inhibits the ability of the matrix to perform its most basic function: load transfer. Delamination results in high stress concentrations about laminate voids caused by matrix cracking. These stress concentrations accelerate the growth of such cracks, which can grow to critical length quickly if left unattended. Angelidis *et al.* demonstrated a method of detecting delamination in a carbon fiber-based FRPC by measuring laminate piezoresistivity before and after impact damage through arrays of individual electrodes at opposite ends of the laminate. Their experimentation showed that the change of measured piezoresistivity of the FRPC after controlled impact damage was dependent on the magnitude of the applied damage, and the location of the input currents applied to the sample [13]. Swait *et al.* also demonstrated the ability to detect delamination via through-thickness electrical potential analysis of a CFRP panel following a controlled impact event [14].

1.3.4. Nanoparticle-based conductive polymer composite sensors

One of the greatest benefits of piezoresistivity-based SHM transducers is the simplicity of signal conditioning and analysis. In a basic piezoresistivity SHM system, a voltage is applied by a continuous source to the sensor element that is part of or bound to a structure. A pristine

resistance measurement is taken when the structure is unloaded in pristine condition. Subsequent deformation or damage is expected to produce a change of resistance of the sensing element when returned to an unloaded state [15]. In contrast to self-sensing conductive FRPC, which rely solely on the load-bearing constituents of the composite, piezoresistive FRPC have been achieved by incorporating conductive filler particulates into composites with electrically insulating constituents (i.e. glass-fiber composites). Impregnating an electrically insulating matrix with a sufficient concentration of conductive micro/nano-particles, randomly oriented conductive particle networks can be formed [16]. These material systems, referred to as conductive polymer composites (CPCs), have since garnered interest in the SHM community as candidate material for strain and fatigue transducer development. CPC materials typically consist of various electrically insulating polymer(s) blends and conductive particles with sizes ranging from millimeters to nanometers. The benefits of such transducers include the simplicity of their design, ease of their manufacturing, and their atomic compatibility/similarity to that of structural composite designs, namely carbon-based FRPC.

Piezoresistivity has been demonstrated in a variety of CPCs with conductive constituents including metallic nanoparticles, chopped carbon fiber, carbon nanotubes, graphene, and carbon black (CB). The most commonly selected conductive filler material for piezoresistive CPC transducers are carbon-based. Nag-Chowdhury *et al.* demonstrated the viability of deploying a CPC transducer composed of epoxy and high-aspect ratio carbon nanotubes for SHM applications [17]. The results of this work highlight the potential for using transducers of this form to quantify fatigue life expectancy based on the drift of sensor resistance with an increasing number of load cycles. The prospect of deploying a network of CPC transducers with intent to monitor conductivity drift during service life presents a unique set of complex engineering

problems. Critical problems include the reproducibility of pristine transducer signatures, and the development of models used to correlate changes in transducer signature to changes in structural integrity, current factors of safety, and remaining service life.

1.4. Understanding the electromechanical characteristics of CPCs

Efficient and repeatable CPC sensor manufacturing methods are critical for large-scale deployment of CPC-based SHM systems in consumer industries. While various manufacturing methods have been reported in the literature, the results of studies of CPCs with similar constituent materials reveal significant variation in nominal electromechanical properties, as shown in Figure 1. To better understand, predict, and control CPC electromechanical properties, more precise manufacturing processes, process validation techniques, and predictive models are needed. In the following section the current state-of-the art in CPC manufacturing, electromechanical characterization, and predictive modeling is discussed.

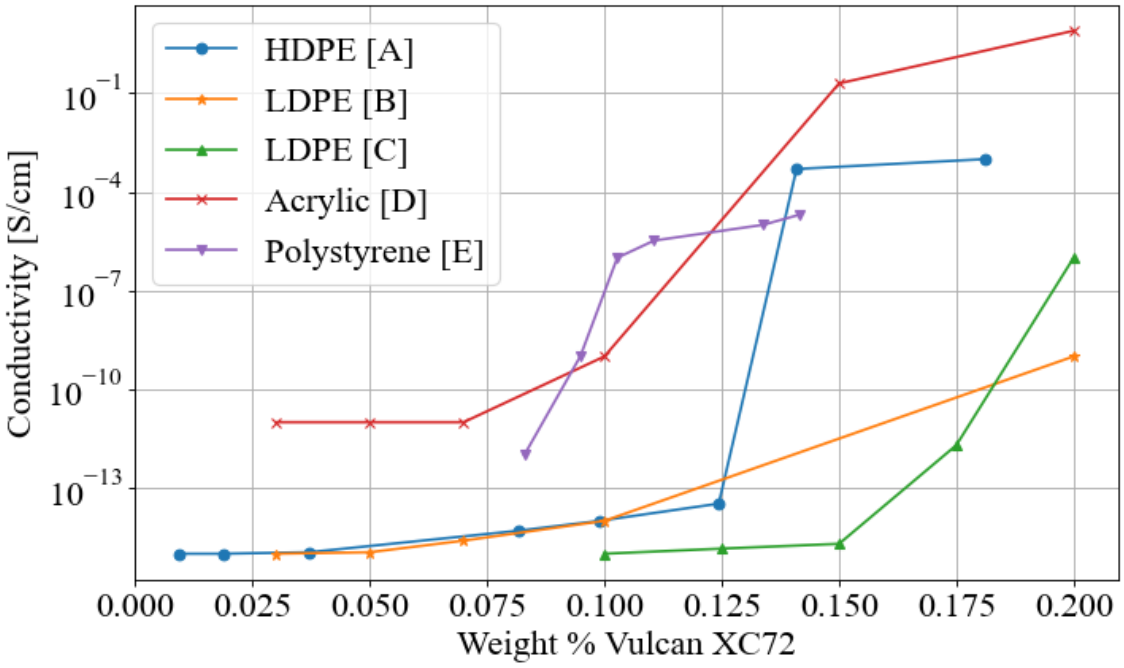

Figure 1 – Plot of the CB-based (Vulcan XC72, Cabot Co.) CPC conductivities with varying polymer matrices reported by various sources: (A) [18]; (B) [19]; (C) [20]; (D) [21]; (E) [22];

1.4.1. Experimental characterization of CB CPC samples

The popularity of CPC transducer research has resulted in a large body of experimental literature that continues to grow. Due to the overwhelming number of CPC constituent combinations and subsequent reports in the literature over the past few decades, it is unfeasible to review the entire landscape of experimental CPC transducer research in this dissertation. This section will focus on recent research regarding the development of CB CPC manufacturing and electromechanical characterization methods and those demonstrated with conductive fillers comparable to CB.

Numerous manufacturing methods for creating carbon-based CPC transducers have been demonstrated in the literature, including injection/compression molding [23–34], extrusion [35, 36], melt-spinning [37], 3D-printing and ink-jetting [34, 38–43], fumigation coating [44, 45], spray-layer-by-layer (sLBL) [17, 46], and hot pressing [32, 47–49] among others [50–52]. Each method has advantages and disadvantages, and often the viscosity of the pre-cured CPC mixtures limits the potential for using some methods. For example, CPC mixtures containing highly viscous polymers cannot be effectively thinned for sLBL deposition, but hot pressing is an easy solution for generating repeatable transducer geometries out of such constituents. For CPC mixtures with lower viscosities, or for those whose viscosity can be effectively thinned, sLBL is an attractive option due to its proven scalability and precision. Nag-Chowdhury *et al.* showed great manufacturing control over CPC transducer thickness (0.7 to 1.6 microns) could be achieved via their experimental sLBL deposition apparatus [17].

Establishing electrical contact to the conductive network within a CPC medium is another aspect of CPC research that presents a challenge. Many measurement systems for interrogating CPC conductivity have been demonstrated in the literature. Electrodes for interrogating the CPCs

resistive network are typically achieved through embedded conductors or external surface probing. For external surface probing, researchers have demonstrated measurement repeatability by deploying custom surface clamped electrodes [24, 27, 29, 50, 53], while others have deployed commercial volume resistivity test fixtures such as the Keithley 8009 [32, 34, 47]. Instead of deploying mechanically reinforced contacts, researchers have also demonstrated the effectiveness of applying conductive surface coatings, such as sputtered gold or conductive silver paste, to create electrical contacts [25, 28, 30, 31, 36, 40, 43, 48, 49]. To reduce electrical contact resistances on external surfaces of CPC transducers for either method, surface preparation such as sanding and polishing are typically deployed to expose outermost particulates of the subsurface conductive networks. Other researchers have utilized the inherent adhesive properties of the CPC constituents to adhere CPC films to metallic structures with exposed contacts [38, 41, 44, 45]. Alternatively, Nag-Chowdhury *et al.* demonstrated an embedded carbon fiber could be used to interrogate CPC conductivity and piezoresistivity [17]. This method is enticing due to the reinforcing nature of conductive carbon fibers and their widespread use in industrial structural designs.

Piezoresistivity of CPC materials have been realized by monitoring changes in CPC conductivity while subjected to strain deformation. CPC piezoresistive responses to both tensile and compressive strains have been reported in the literature. For low-aspect ratio particle based CPCs, compressive strains produce in an increase in measured conductivity while tensile strains produce the opposite effect. This phenomenon is a consequence of particle motion within the CPC inducing rearrangement of conductive pathways, thus varying measured conductivity [54]. For researchers interested in the development of CPC flexible strain gauges, reversibility or recovery of the pristine resistivity when unloaded is desired, but often not realized [43, 55–58].

For researchers interested in CPC SHM applications, understanding the underlying principles behind such irreversible conductivity change in fatigued CPC materials is a fundamental challenge on the cutting edge of the discipline.

1.4.2. Effects of dispersion on CPC conductivity

Conductive carbon nanoparticles, but more specifically CB nanoparticles, often become highly agglomerated during manufacture and packing due to the Van der Waals forces between them. Investigations of the effects of applying various dispersion methods on the mechanical and electrical properties of CB/polymer mixtures can be found as early as 1931 [59]. Boonstra and Medalia described the process of mixing as "intangible" and "of the most variable" in CB-rubber technology [60]. Research regarding the fundamental problem of CB-polymer dispersion persisted through the 20th century. For an in-depth review of the field during this time the reader is directed to the work of Huang [61].

Recently, researchers have shown that conductive network formation, often referred to as percolation, can be achieved at lower weight percentages of the conductive filler by thoroughly dispersing agglomerate structures, resulting in more random distributions of particles in the matrix [62–64]. Various dispersion techniques have been utilized for this purpose, including magnetic stir mixing, ultrasonic bath mixing, ultrasonic probe mixing, and calendaring via roll milling. The effectiveness of various preparation methods varies greatly by the nature of the constituents, namely the morphology of the conductive filler and the viscosity of the suspending polymer matrix. Less viscous polymers can be easily impregnated with a large variety of conductive fillers, of both high and low-aspect ratios, through ultrasonic-probe mixing and mechanical stirring. Highly viscous polymers, and mixtures that are highly viscous due to the concentration and morphology of the filler, require greater shear forces than some mixing

methods can provide. For high viscosity mixtures, calendaring via roll milling provides the most effective means of filler incorporation. Moriche *et al.* explored CPC dispersion using various combinations of ultrasonic probe mixing and calendaring and found evidence of the benefit of dispersion via calendaring [64].

Dispersion influence on the properties of nanocomposites is frequently noted in recent literature, especially in studies experimentally observing electromechanical behaviors of carbon-based nanocomposites [58, 65–72]. Some studies examine dispersion influence trends in experimental data by comparing measured properties of equivalently concentrated samples that differ in preparation [66, 70, 71]. Ji *et al.* defined a particle dispersion index for CB nanocomposites by curve fitting linear functions to normalized storage and loss moduli data [69]. Direct measurement and quantification of dispersion in nanocomposites has been an active area of research over the past few decades. Researchers have leveraged various technologies in the characterization of nanocomposite dispersion including small angle neutron/x-ray scattering [73], electron microscopy [65, 66, 73–84], atomic force microscopy [83, 85], and light microscopy [84, 86–89]. Microscopy images of nanocomposite samples are often used to quantify dispersion related statistics such as the area fraction of agglomerates in the image [89], the distribution of the areas of the agglomerates in the image [79, 80], estimations of average effective agglomerate diameter/shape (sphericity, convexity, etc) [73, 75, 78], and other dispersion related calculations [76, 86, 87]. Sample preparation methods are dependent on the interrogation tool deployed. For example, freeze-fracture and microtome sectioning is typically used to perform scanning or transmission electron microscopy on cured nanocomposite samples. Spin coating has also been demonstrated as a cost effective option for producing nanocomposite films with optical properties favorable for dispersion interrogation via light microscopy [74, 75, 81, 88, 90–94].

It has been proposed that computational methods might allow for more rapid investigation of the effects of dispersion on the electromechanical properties of various CB nanocomposite configurations at different length scales [95]. Feng *et al.* demonstrated the influence of dispersion on nanocomposite conductivity using the large-scale atomic/molecular massively parallel simulator developed by Sandia National Laboratories [96]. Akram *et al.* constructed COMSOL models of multilayer silicon dioxide nanocomposites from high-resolution electron microscopy images, and compared the multi-physics simulation predictions of electrical permittivity to measured permittivity of physical samples [97]. Coupette *et al.* developed a Monte Carlo simulation tool to generate fractal CB agglomerates in a representative volume element (RVE) and subsequently examine probabilistic network formation and percolation within [98]. Asylbekov *et al.* utilized discrete element and computational fluid dynamics methods to study the fracture and dispersion of fractal CB aggregates of varied fractal dimension and size subjected to shear stresses comparable to those created via a planetary mixer (3 to 40-kPa) [99]. The study concluded that with increasing shear stress, the diameter of gyration of the simulated aggregates converged to a value of 200-nm, no matter the initial size and fractal dimension defined at simulation start.

Furthering fundamental understanding of structure-property relationships of nanocomposites at length scales ranging from nano to macro will enable rapid improvement and deployment of nanocomposite sensor designs [100]. The efficiency of computational methods for testing a multitude of nanocomposite configurations and features at varying length scales is promising. Stochastic modeling methods provide a means to validate theoretical models with the precondition that the RVEs generated are of sufficient fidelity.

1.5. Predictive modeling of CPC electromechanical properties

Predicting the effective electromechanical properties of heterogeneous materials, such as CPCs, is critical for the rapid development and application of such materials [101]. While the problem of RVEs densely packed with spherical elements has been explored in great detail [101–104], problems involving less densely populated volumes have received less attention in the literature. Multiple semi-empirical and numerical methods have been proposed for predicting electrical characteristics of CB CPC sensors [105]. However, inconsistencies exist between such models examining CPCs of similar composition. More recent research has shown the potential of using stochastic methods to more accurately estimate CPC characteristics [96, 106–112]. The following sections will discuss advances in analytical models, followed by advances in stochastic modeling methods for explaining and predicting CPC electromechanical characteristics.

1.5.1. Analytical conductivity/piezoresistivity models

One of the most commonly deployed analytical models in the literature is the theory of percolation [113, 114]. This theory is described by the equation,

$$\sigma_c = \sigma_f\left(\psi_f - \psi_c\right)^t \qquad \text{Equation 1-1}$$

where ψ_f is the volume fraction of conductive filler, ψ_c is the percolation volume fraction of the composite, σ_f is the conductivity of the filler, and σ_c is the conductivity of the composite. The variable *t* in Equation 1-1 is the critical power law exponent and depends on the nature of the composite's final form. For 2D composites (such as surface coatings/films) a value of ~1.33 is typically used [115], while a value ~2.0 is typically used for 3D composites [116]. This formulation accurately describes the exponential increase of conductivity observed in CPC samples with minute differences in concentrations of conductive filler.

The conductive filler concentration about which small variations in filler content produce large variations in conductivity is referred to as the percolation threshold. A multitude of models have been developed to describe the conductivity of various CPCs created with conductive filler concentrations about the percolation threshold. Radzuan *et al*. have presented a thorough review of models for predicting conductivity of CPCs with respect to their concentration of conductive filler(s) [105]. Such models are typically adapted to empirical evidence by fitting combinations of model-specific parameters to experimental results.

Carmona *et al.* developed an analytical model based on theory of percolation to describe the piezoresistive behaviors of CB CPCs [117]. In that work, the piezoresistive behaviors of CPC under hydrostatic loading conditions were described as a change in volume concentration of the CPC due to the differences in the elastic properties of the filler and the matrix. Additionally, the sensitivity of the CPC to applied stress was shown to diverge as the filler concentration of the CPC approached the percolation threshold. To address the model's limitations in predicting the effects of various influencing factors (filler particle diameter, matrix compressive modulus, etc.) on piezoresistance quantitatively, and to explain the time dependence of CPC piezoresistance, Zhang *et al*. proposed an alternative analytical model [118]. The model proposed by Zhang *et al*. describes a CPC volume consisting of conductive spherical element chains suspended in an insulating matrix spanning parallel conductive electrodes. The resistance can then be approximated with,

$$R = \frac{(L-1)R_m + LR_c}{S} \approx \frac{L(R_m + R_c)}{S} \qquad \text{Equation 1-2}$$

where R is the resistance of the composite, R_m is the resistance between individual particle pairs, R_c is the resistance across the length of one particle, L is the number of particles forming one conductive chain, and S is the total number of conductive chains spanning the electrodes.

The quantum-mechanical theory of electron tunneling, which explains the flow of electrons between conductors separated by insulating barriers, is used to define the resistance between individual particle pairs. Simmons' analytical formulations propose that the tunneling current J between atomically similar conductors separated by an insulating barrier at low voltages can be written defined as,

$$J = \frac{3\sqrt{2m\varphi}}{2s}\left(\frac{e}{h}\right)^2 V\, exp\left(-\frac{4\pi s}{h}\sqrt{2m\varphi}\right) \qquad \text{Equation 1-3}$$

where h is Planck's constant, m and e are the electron mass and charge respectively, V is the applied voltage, s is the thickness of the insulating barrier, and φ is the height of potential barrier between the conductors. Assuming the effective area of conductance between the particles as a^2, the effective resistance between particle pairs can be defined as,

$$R_m = \frac{V}{a^2 J} = \frac{8\pi hs}{3a^2\gamma e^2}\exp(\gamma s) \qquad \text{Equation 1-4}$$

where

$$\gamma = \frac{4\pi}{h}\sqrt{2m\varphi} \qquad \text{Equation 1-5}$$

From this formulation, it is observed that the resistance between particle pairs diverges as the thickness of the insulating barrier separating them grows. The resistance across the length of an individual particle is considered negligible compared to the tunneling resistances assumed to be present in each particle chain, therefore $R_c \approx 0$. Substituting Equation 1-4 into Equation 1-2, the resistance of such CPCs can be calculated theoretically as,

$$R = \frac{L}{S}\left[\frac{8\pi hs}{3a^2\gamma e^2}\exp(\gamma s)\right] \qquad \text{Equation 1-6}$$

Adapting the model to describe CPC piezoresistive behavior, it is assumed that the separation between conductive particles changes from s_0 to s when strained. The relative resistance (R/R_0) can then be calculated as,

$$\frac{R}{R_0} = \frac{s}{s_0}\exp[-\gamma(s_0 - s)] \qquad \text{Equation 1-7}$$

where R_0 is the CPC's nominal resistance, and s_0 is the original assumed interparticle separation. Assuming that the change of interparticle separation along the conducting path is only due to matrix deformation, the separation s can be calculated as,

$$s = s_0(1 - \epsilon) \qquad \text{Equation 1-8}$$

where ϵ is the strain of the matrix. By assuming the spherical particles to be monodisperse and arranged in a cubic lattice, s_0 can be calculated as,

$$s_0 = D\left[\left(\frac{\pi}{6}\right)^{\frac{1}{3}}\theta^{-\frac{1}{3}} - 1\right] \qquad \text{Equation 1-9}$$

where D is the particle diameter, and θ is the filler volume fraction of the CPC. Substituting Equation 1-8 and Equation 1-7 into Equation 1-6, the relative change of resistance is defined as,

$$\frac{R}{R_0} = (1 - \epsilon)\exp\left\{-\gamma D\left[\left(\frac{\pi}{6}\right)^{\frac{1}{3}}\theta^{-\frac{1}{3}} - 1\right]\epsilon\right\} \qquad \text{Equation 1-10}$$

This formulation has been modified in the literature for special cases and other considerations such as the effects of creep, excitation voltage, and electrode contact resistance on CPC conductivity [63, 119–121]. Such cases and formulations are beyond the scope of the research presented in this dissertation.

1.5.2. Stochastic modeling methods

Good agreement between fitted analytical models and experimental data of CPC conductivity and piezoresistivity is common. It is far less common to find agreement between reported values of model parameters (i.e. percolation threshold, critical power law exponent, etc.) fitted for experimental datasets from CPCs of nearly identical composition. It is hypothesized that this is a consequence of the stochastic nature of CPC materials and the

influence of various factors that can be difficult to quantify including filler conductivity, the nature of the polymer-filler interactions, processing techniques, and so on.

Recent research has shown the potential of using stochastic methods in estimating CPC characteristics [96, 98, 106–112]. These methods utilize the capabilities of high-performance computing systems to create representative volume elements (RVEs) composed of conductive particles suspended in a polymer that is not discretely modeled. For this study, the authors decided to base the development of the model on previously reported 3-D RVE models [98, 106, 108, 109, 122]. Ma and Gao presented their model of CPCs with curved high-aspect ratio conductive fibers in 2008. In that research, the effect of fiber morphology (length, waviness, aspect ratio) on the percolation threshold was analyzed [122]. Later models developed by Bao *et al.* and Matos *et al.* focus exclusively on carbon nanotubes (CNT), a popular conductive high-aspect ratio nanoparticle [108, 109]. Those models were both constructed with periodic boundary control, which aims to reduce numerical error with respect to simulation size. Bao *et al.* reported numerical consistency of the conductivity for RVEs with a cubic length 1.1 times the length of the simulated CNT (5μm) while Matos *et al.* reported numerical consistency of the conductivity for RVEs with a cubic length 1.5 times the length of the simulated CNT (462 μm).

The effect of RVE size on conductivity variation is important to consider when addressing the demand for CPC films with thicknesses on the order of microns. To accurately determine the repeatability limitations for stochastic films of this nature, modeling schemes of the highest fidelity are desired. In the study conducted by Stepashkina e*t al.*, the modeling of a CB and polypropylene mixture was described as a "task of spheres" due to the sphericity of carbon black primary particles [106]. Compared to high aspect ratio inclusions, determining placements and interparticle relationships between spherical elements is less computationally

intensive. Thus, performing large-scale simulations becomes more feasible when considering a CB based CPC. For this reason, CB filler materials were selected as the primary focus of this research. The CB CPC stochastic model proposed in Chapter 2 is based on the works of Stepashkina *et al.* and an agglomeration algorithm implementation comparable to that proposed by Coupette *et al.* [98].

1.6. Objectives and outline of the dissertation

The primary objective of this dissertation is to present the research contributions made by the author in the areas of CPC mass-manufacturability, integrity monitoring viability, and dispersion influence on the electromechanical characteristics of CB CPC materials. In Chapter 2 a high-fidelity stochastic model, capable of accurately representing physical CB CPC specimens, is developed for furthering fundamental understanding of the electromechanical properties of such specimens and the change in such properties during service life. The effects of variations in sample preparation parameters are studied, and a method for quantifying dispersion characteristics of CPC mixtures is examined in Chapter 3. CB CPC RVE generation parameters are tuned using experimental sample dispersion statistics. The electromechanical properties of RVEs with varying dispersion characteristics are interrogated analytically and compared to physical specimens in Chapter 4. The implications of the research are summarized in Chapter 5, and final recommendations on future works and areas for consideration are offered in conclusion.

CHAPTER 2

STOCHASTIC MODELING OF CB-BASED CPCS

2.1. Introduction to stochastic modeling approach

The term "stochastic" is an adjective defined by the Oxford dictionary as – "having a random probability distribution or pattern that may be analyzed statistically but may not be predicted precisely" [123]. Stochastic modeling is a computational method used to study patterns arising from problems or systems that have many possible configurations, where such configurations are perceived as inherently random or chaotic. In the field of materials science, stochastic modeling methods have been used to study properties of randomly configured materials at scales ranging from atomistic to macroscopic. As it pertains to CPC research, stochastic modeling methods have been used to elucidate the electromechanical properties of nano-particle based CPCs through the stochastic generation of RVEs and the application of the quantum theory of tunneling, Kirchhoff's Laws, and Ohm's Law [96, 98, 106–112]. Typically, reported RVE electromechanical properties are then compared to experimental data, which are in turn used to tune the model parameters used in formulating the predicted RVE properties.

Two fundamental questions must be addressed when attempting to stochastically model properties of physical systems: (i) Are the formulations used to analyze the properties of the

stochastically generated systems correct/true? (ii) Are the stochastically generated systems sufficiently representative of the physical systems they are modeled after? In this Chapter, the development of a CB CPC stochastic modeling program is detailed. Critical assessment of the model regarding questions (i) and (ii) are presented, and the resulting evolution of the model's algorithms are discussed.

2.1.1. CB CPC stochastic modeling overview

The electromechanical properties of materials are often defined through the characterization of bulk experimental samples. Take for example the property of electrical conductivity ρ, which is defined as,

$$\rho = \frac{AR}{L} \qquad \text{Equation 2-1}$$

where A is the cross-sectional area of the sample perpendicular to the direction of the electric potential difference (V_{IN} to V_{OUT}), R is the measured electrical resistance of the sample, and L is the length of sample from the positive to negative electrodes, as illustrated in Figure 2A. For materials with highly ordered microstructure (i.e. metals), this model is accurate, repeatable, and therefore extremely useful for predicting the electrical resistance of metallic physical specimens at nearly all length scales.

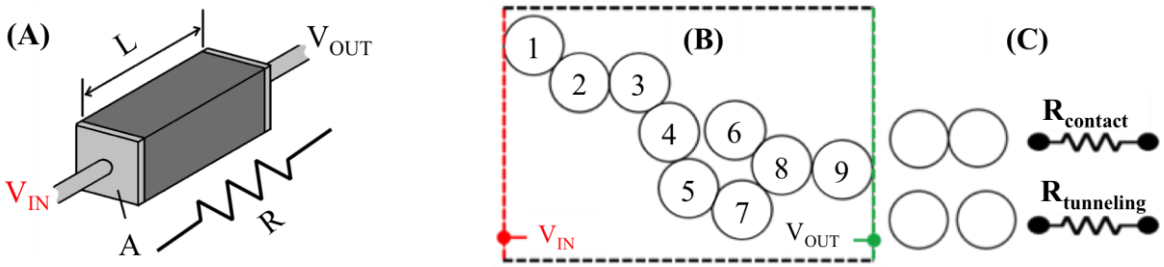

Figure 2 – (A) Illustration of the experimental characterization of a bulk material's electrical conductivity; (B) Example of conductive CB network in CPC; (C) Illustration of the two types of interparticle resistances considered during simulation – quantum tunneling and contact resistance

Most nano-particle CPC materials with nano-particle filler concentrations about the percolation threshold can be considered highly disordered. Figure 2B illustrates a very basic representation of the internal structure of a CB CPC material about which a potential difference is applied (current flowing from left-to-right). The numbered spheres represent CB primary particles randomly oriented within a polymer matrix forming a conductive network between two electrode faces. The conductivity of CB CPCs is dominated by the formation of the interparticle conductive networks illustrated in Figure 2B. CB networks formed within CPCs can be analytically represented as collections of random resistors networked between two electrodes. In the proposed modeling scheme, contact resistance between CB particles is considered constant, while tunneling resistances are calculated as a function of the dielectric properties of the suspending matrix and the distance of separation between the adjacent CB particles. The following formulation, derived by Simmons [124], is used to calculate the resistance between pairs of modeled CB particles conducting electricity via quantum tunneling,

$$R_{tunneling} = \frac{h^2 d}{A_t E^2 \sqrt{2m\lambda}} \exp\left(\frac{4\pi d}{h}\sqrt{2m\lambda}\right) \qquad \text{Equation 2-2}$$

where d is the distance between electrodes, h is Planck's constant, E is the quantum of electricity, A_t is the cross-sectional area of the tunnel between adjacent CB particles, m is the mass of an electron, and λ is the average barrier height of the epoxy [125]. Experimentally derived barrier height values for polymers reported by Xu and Sun [125, 126] and compiled by Soto [107] were used in this study.

The example illustrated in Figure 2B demonstrates the complex and stochastic nature of CPC materials and their electrical properties near the percolation threshold. Consider the 2D network in Figure 2B, and suppose any particle in the RVE were removed. The expected result would be a dramatic increase in the measured resistance of the system. Generally, the number of

potentially conductive pathways in a CB CPC is dependent on the size of the system and the concentration of CB in the system. Physical CB CPC sensors for SHM applications are typically constructed with dimensions on the micro to milli scale, often containing billions of CB primary particles, while the dimensions of the example illustrated in Figure 2B are on the nanoscale. At larger scales, the influence of removing one particle from a single conductive pathway is comparatively miniscule as other conductive pathways are likely present in the system. It is extremely unlikely that two equally concentrated CB CPC milli-scale systems will have the exact same net resistance and even more unlikely that their CB conductive pathway configurations will be identical. For this reason, it is easy to understand why stochastic modeling methods are a promising avenue for rapid characterization and prediction of CB CPC electromechanical properties.

The flow diagram in Figure 3 provides an overview of the algorithm used to generate predictions of the effective electrical conductivity of CB CPC materials via stochastic modeling. Since CB CPC electrical conductivity is stochastic, many RVEs must be generated to create a dataset that is statistically representative of the numerous possible physical configurations. The first iteration of the RVE generation and analysis program was written in Matlab®, and later rewritten in C++ for improved simulation efficiency. Once an RVE is generated and analyzed, the resulting conductivity is appended to a file that is then post-processed using Python. The Python program computes the running average of the reported conductivities to determine whether or not more RVEs are necessary to converge the average estimated conductivity. In the following sections the physical constraints, definition, and analysis of the CB CPC stochastic model are discussed in detail. The development of more advanced stochastic model algorithms are prefaced by preliminary results and discussion about ideas and goals for model improvement.

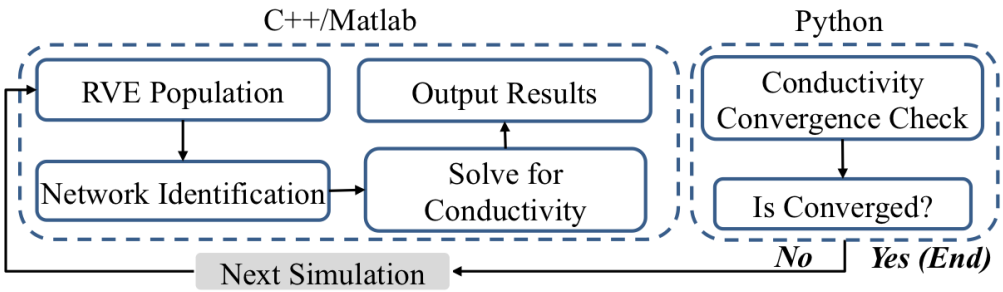

Figure 3 - High-level flowchart illustrating the execution of the proposed stochastic model

2.1.2. Physical constraints of the RVE and simulated CB

As illustrated in Figure 3, the stochastic modeling process begins with the generation of a RVE populated with spherical elements representing CB primary particles. The first step in generating the RVE lies in defining its desired physical characteristics. The program is coded to establish physical simulation parameters via a user defined input file. The input file contains the following user-defined variables: RVE length/width/height, the RVE discretization unit length, the weight fraction of CB in the RVE, the density of the CB, the distribution of the diameters of the CB primary particles, the maximum allowable CB penetration (illustrated in Figure 7A), the density of the polymer ρ_p, the polymer barrier height λ, and the maximum tunneling distance considered numerically relevant during simulation.

The Mersenne Twister random number algorithm is used to generate random coordinates for CB particles to be placed in the RVE [127]. In this study, the modeled CB particles are considered to have a soft outer shell that can be penetrated by adjacent particles to a certain degree as shown in Figure 7A. The maximum allowable magnitude of particle-particle penetration is defined as an integer value scaled by the RVE discretization unit length. This soft-shell technique is deployed to imitate the fusion of particles into colloidal structures, commonly observed in densely packed CB samples. CB particles placed in the RVE must follow two simple rules: (1) it cannot exist outside of the RVE boundary, and (2) it cannot cause particle-particle

penetration that exceeds the soft-shell boundary of any particle. To obey (2), it is imperative for the particle placement algorithm to verify that each newly placed particle does not over penetrate previously existing particles in the volume.

2.2. First iteration stochastic modeling program

The first iteration of the stochastic modeling program populated RVEs purely randomly. Random placement of all particles in the RVE is assumed to be representative of a perfect primary particle distribution; meaning particle placement probability is uniform throughout the RVE. This perfect distribution represents a scenario where agglomerates that occur in the RVE are not due to packaging methods or Van der Waals forces, but rather the complete randomness of an ideal mixture.

The first step in populating an RVE with CB particles is to generate a random coordinate set within the user-defined space. Early placement algorithms generated particle coordinates in a sequential or serial manner, which required the location of each newly generated particle to be compared to all previously existing particles in the volume. This comparison was used to ensure that newly generated particles would not interfere with existing particles. Due to this serial approach, and to the increased probability of interference as the RVE becomes populated, time spent by the placement algorithm increased exponentially with an increased number of particles placed. While Matlab® was useful for early algorithm development, its interpreted nature resulted in a memory-intensive code that required impractical simulation times. Rather than work to improve the efficiency of the interpreted code using just-in-time (JIT) compilation or other advanced methods, the authors decided to use a pre-compiled coding language. The first iteration of the code was rewritten in C++ while maintaining a majority of the original architecture. As expected, the resulting code was significantly more efficient.

In the particle placement algorithm, interparticle distance calculations must be performed to ensure proper placement. During this algorithm, it was found computationally efficient to store data regarding which particles are considered electrically contacting (hereafter referred to as neighboring). These neighboring relationships are stored in memory for determining the existence and resistance of the simulated conductive pathways. In addition to the interparticle relationships, newly placed particles are also checked for their relationship to the electrode planes (positive electrode at x = 0, ground electrode at x = RVE length). If a particle is found to be neighboring an electrode plane, that information is also stored as a Boolean for later algorithmic identification of conductive network formation.

2.2.1. Solving for conductivity

Once the desired number of particles has been placed in the volume, an algorithm is deployed to determine the existence of a conductive particle chain spanning the electrodes. If a particle has neighbors (or neighbors of neighbors of neighbors...) that span the length of the RVE contacting the opposing electrodes, the existence of a conductive pathway is realized. Neighboring particle resistances are then determined using the data stored during the placement algorithm. Once the interparticle resistive network has been defined, the nodal voltage of each CB particle in the current carrying network can be determined. To better explain the procedure used in solving the RVEs random resistor network, consider the 2-D case represented in Figure 2B. Kirchhoff's Current Law (KCL) states that the algebraic sum of currents flowing through all pathways in a network connected to a single node must equal zero [123]. Performing KCL at node 4, for example, gives the following relationship,

$$I_{4-3} + I_{4-5} + I_{4-6} = 0 \qquad \text{Equation 2-3}$$

where I is the current and the subscript (*4-n*) denotes the current flowing from node 4 to node n. Expanding the summation and applying Ohm's Law, the equation becomes,

$$\frac{V_4-V_3}{R_{4-3}}+\frac{V_4-V_5}{R_{4-5}}+\frac{V_4-V_6}{R_{4-6}}=0 \qquad \text{Equation 2-4}$$

where V_n is the voltage at node *n,* and $R_{4\text{-}n}$ is the resistance between nodes 4 and *n*. The same expansion can be performed at node 1 which is in contact with the positive RVE electrode. KCL at node 1 gives,

$$I_{1-pos}+I_{1-2}=0 \qquad \text{Equation 2-5}$$

where the subscript *pos* is used to denote contact with the positive electrode. Similar to Equation 2-4, Ohm's Law can be used to expand Equation 2-5, to yield,

$$\frac{V_1}{R_{1-pos}}+\frac{V_1-V_2}{R_{1-2}}=\frac{V_{IN}}{R_{1-pos}} \qquad \text{Equation 2-6}$$

where V_{IN} is the prescribed voltage of the positive electrode. Expanding the rest of the nodal summations in the same manner, a solvable linear system of equations can be formed for the entire RVE. This large system of equations can be represented in matrix notation as simply,

$$\bar{V}=\bar{I}\,\bar{\bar{R}} \quad or \quad \bar{\bar{G}}\,\bar{V}=\bar{I} \qquad \text{Equation 2-7}$$

where $\bar{V}$ is the voltage vector, $\bar{I}$ is the current vector, $\bar{\bar{R}}$ is a matrix of resistance values of the random resistor network, and $\bar{\bar{G}}$ is the conductivity matrix. The conductivity matrix and current vectors are sparse, so storing their respective values in C++ runtime vectors can be memory costly if all zero-values are retained. Therefore, sparse matrix templates are employed, and optimized LU decomposition is performed using the Eigen library to solve the system of equations in Equation 2-7for the unknown nodal voltages [128]. Once the nodal voltages have been determined, the resistance across the RVE can be found by calculating the algebraic sum of the currents entering the RVE and using KVL to give,

$$R_{RVE} = \frac{V_{IN}}{\Sigma I_{IN}} \quad \text{Equation 2-8}$$

where R_{RVE} is the effective resistance across the entire RVE, and I_{IN} are all currents traveling through nodes that are in contact with the positive electrode which has a prescribed voltage of V_{IN}.

2.2.2. Simulating strain

Since the foundation for calculating RVE resistance has been laid, an additional algorithm was constructed to explore the electromechanical effects of strain on the RVE. Once all particle coordinates have been defined, strain can be simulated on the RVE by applying directional scaling factors to the interparticle distance calculations. These scaling factors are dependent on the physical parameters of the simulation: namely the magnitude and direction of the strain and the Poisson's ratio of the suspending epoxy. Considering the vast majority of the RVE is composed of isotropic epoxy, the RVE is assumed to have isotropic characteristics. Uniaxial tension is simulated in the direction of net current flow through the RVE (x-direction). The RVE is subjected to simulated contraction in the y and z directions [129]. The general relationship between all principal strains can be expressed as,

$$\epsilon_y = \epsilon_z = -\nu\epsilon_x \quad \text{Equation 2-9}$$

where ε is the strain, ν is Poisson's ratio, and subscripts denote the principal direction associated with each strain. Various magnitudes of global uniaxial tensile strain are applied to the RVE. Local strain values are then calculated and are applied to the interparticle distance calculations. New interparticle relationships are defined, and a modified resistive network is formed where the resulting RVE resistance is calculated via the methods previously described.

2.3. First model results and discussion

Conductivities of stochastically generated RVEs were calculated, and during calculation nodal voltages of CB particles were determined. These nodal voltages were used to visualize the flow of electrons through the RVE by mapping the voltages in a scaled manner. An example of this nodal voltage distribution is shown in Figure 4 which was created using OVITO [130]. The non-current-carrying particles of the RVE have been omitted from these graphical representations for clarity. At a glance, one quickly notices that large clusters of particles are at similar values of electric potential. This potential clustering is caused by low-resistance contact between agglomerated particles separated by relatively high-resistance contact points between agglomerates in the percolated network. These combinations of contact and tunneling resistance along with agglomeration results in a low potential gradient within agglomerates and a high potential gradient between agglomerates.

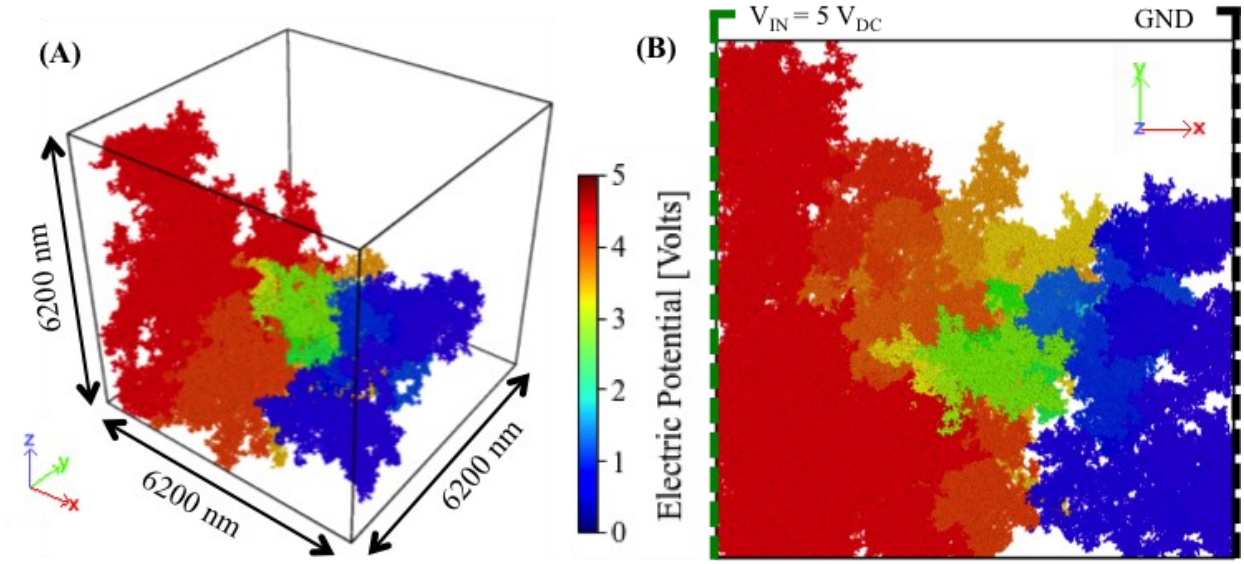

Figure 4 - (A) Orthographic view of a conductive network formed inside a cubic 6200 nm RVE. (B) 2D view of the RVE showing voltage distribution within the conductive network. The x- face (left edge) of the RVE has a direct-current voltage of 5 volts (5VDC) and the x+ face (right edge) is connected to ground (GND).

In testing the first iteration of the program, focus was placed on determining the RVE scale threshold at which simulated conductivity could be considered representative of bulk material characteristics. Multiple conductivity simulations at a specified RVE size were repeated, and only the results of such simulations where conductive networks existed were averaged. A moving average of the conductivity of the simulated dataset was monitored periodically to determine when sufficient convergence was achieved. The moving average was considered convergent once the range of the moving average for the last 100 simulations was less than or equal to 5% of the final average. Average conductivities were calculated for each set of RVE dimensions by monitoring the moving average as shown in Figure 5A. Once the average conductivity was considered convergent, its average was recorded along with the corresponding cubic RVE side length. After exploring conductivity convergence for a fixed RVE size, attention shifted toward determining the size of RVE required to achieve an average conductivity that is independent of RVE size. The simulation procedure was repeated while incrementally increasing RVE side length in order to investigate the relationship between converged average conductivity and RVE side length. Results of these conductivity simulations are plotted in Figure 5C. With all parameters held constant except for RVE size, average conductivity was found to decrease significantly while increasing RVE size. The converged conductivity data in Figure 5C is fitted with a curve of the form,

$$y = a + b(c^x) \qquad \text{Equation 2-10}$$

where a, b, and c are variables to be fitted to the data, and x is the cubic length of the RVE. This exponential function is in good agreement with the serial data, and displays a convergence trend to a constant value a for this specific set of model parameters. The length required to achieve convergence, x = 6200 nm, was determined when the fitted function was within 1% of the fitted

value for a. The average time cost of generating and analyzing a single RVE with a given cubic length is shown in Figure 5B. As expected, simulation times grew rapidly with an increase in RVE size. Earliest versions of the program developed in Matlab® were very inefficient, and the choice to redevelop the program in C++ was found to be well worthwhile. At the converged RVE size of 6200 nm, it was estimated that approximately 520,000 seconds (~6 days) would be required to perform a single RVE simulation using the serial model. Considering it may take several hundred of these simulations to calculate the converged average conductivity, using the serial model would not be practical. This realization influenced the decision to seek further improvements to computational efficiency via parallel and load-distributed computing concepts.

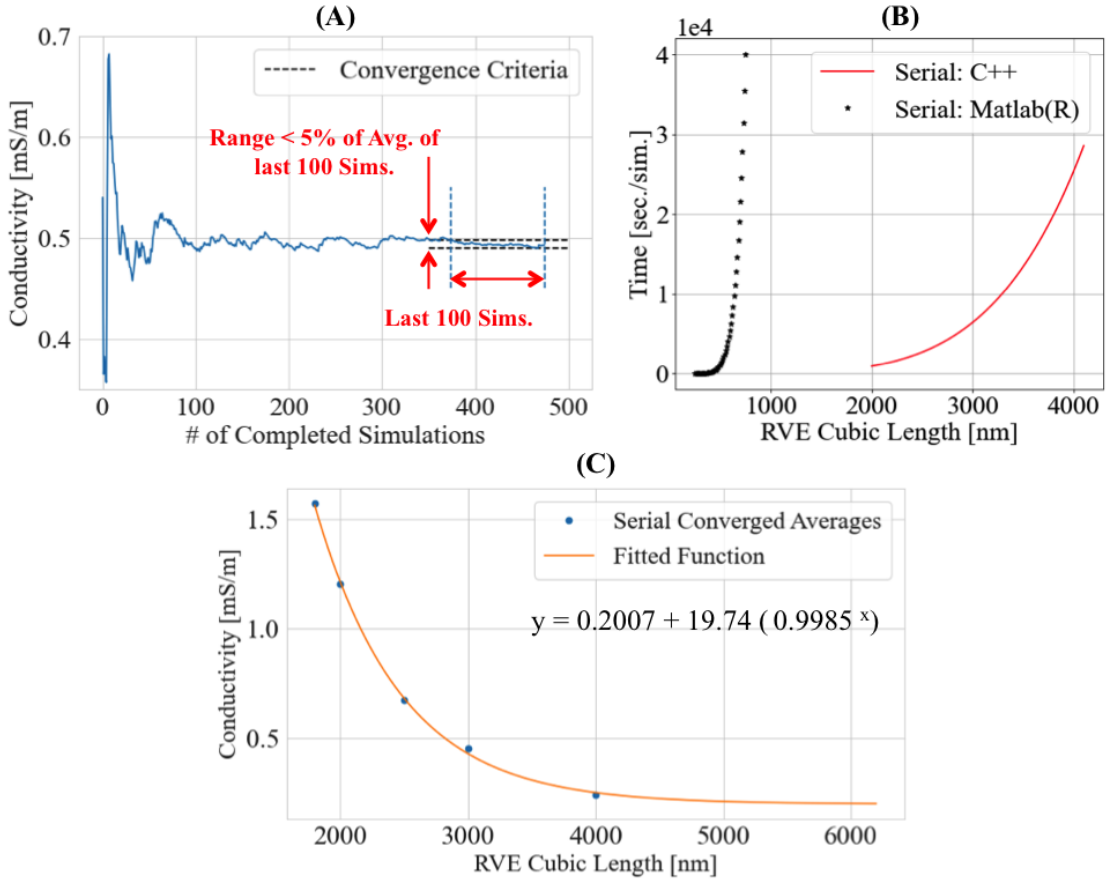

Figure 5 – (A) Plot showing convergence of moving average of simulated conductivity versus the number of completed simulations; (B) Plot comparing the time per simulation for increasing RVE cubic lengths for the first iteration of code executed in both Matlab ® and C++; (C) Plot showing convergence of simulated conductivity versus RVE cubic length from first iteration of the stochastic modeling program

2.4. Psuedo-parallel/load-distributed placement algorithm development

Originally, the model was designed with the intent to study nanoscale simulations, but the realization of simulation size dependence drove scalable model development. After realizing the need for a more efficient and scalable tool, model development focus shifted towards parallelized and load-distributed (LD) RVE generation algorithms. The first iteration of the LD model was designed to decompose the full RVE into smaller *cubic* sub-RVEs as shown in Figure 6A. Each sub-RVE would then be assigned to an individual computer process where it would be populated with particles using a serial algorithm. This model iteration suffered a few inherent deficiencies. First, the LD model allowed particles located on sub-RVE boundaries to penetrate other boundary particles beyond the soft-shell limit (Figure 7A), which is discussed in Section 2.1.2. As a result, additional algorithms were required to identify interfering particles from adjacent sub-RVEs. Such interferences decreased the fidelity of the simulated RVE and warranted further investigation on placement algorithm modifications.

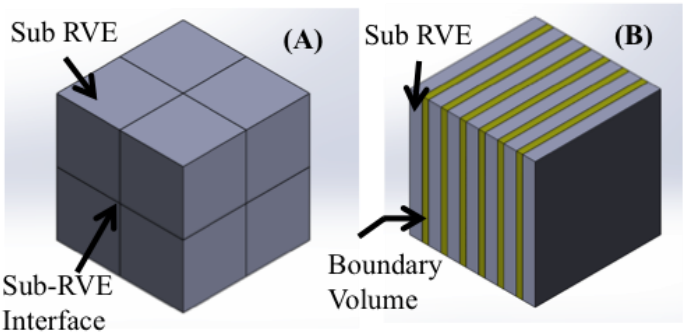

Figure 6 - (A) Load distributed method: RVE decomposition with no sub-RVE interface cross checking. (B) Pseudo-parallel method: RVE composed of sub-RVEs and boundary volumes

To combat the issue of interferences at the boundaries between sub-RVEs, the algorithm was modified to create boundary volumes (BV) as depicted in Figure 6B. These boundary volumes were created so that particles existing in one subdomain could not directly interact with

particles in another subdomain. This was achieved by defining the widths of the BVs so that particles placed on opposing interfaces could not interact electrically. Boundary volume width W is defined as the sum of the particle diameter a and the maximum allowable tunneling distance d_T. It is also assumed that each sub-RVE and BV contains the same weight percentage of particles as the greater RVE. This assumption allows the algorithm to manage particle placement for each set of sub-RVEs independently while ensuring that the resulting RVE will have the prescribed weight percentage. Dividing the RVE in this manner allows for parallel placement of the particles in each set of sub-RVEs; however, accounting for potentially interfering particles positioned near adjacent BVs remains a challenge. To overcome this challenge, the algorithm first places particles in BVs simultaneously. It is important to emphasize that adjacent sub-RVEs are currently empty. An object containing the identities and locations of these BV particles is stored for later use. After placing the particles in the BVs commensurate with their volumetric representation of the greater RVE, particles are then placed in the sub-RVEs. This final placement task *stitches* all sub-RVEs and BVs together to form a single RVE while efficiently accounting for cross-domain particle interactions.

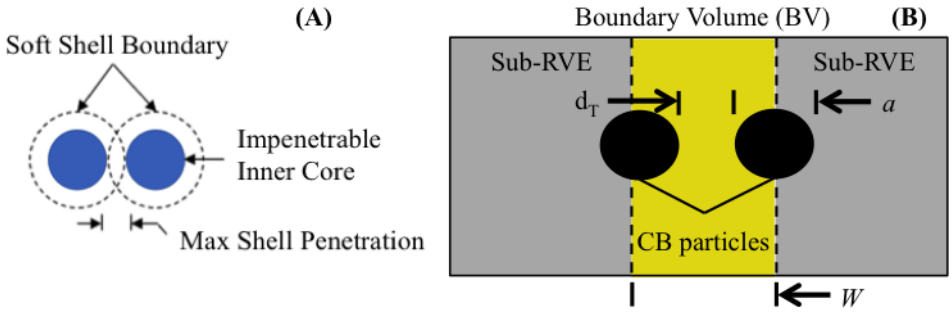

Figure 7 – (A) Representation of the model assumption that limited particle-particle penetration is allowed; (B) Boundary volume (center) separating two adjacent sub-RVEs. The width of the boundary volume is driven by the sizes of the particles being placed, as well as the maximum allowable tunneling distance defined by user input

The proposed interdigitated sub-RVE particle placement algorithm can easily be implemented and executed via parallel computing. The host process randomly selects a sub-RVE to place a new particle in and assigns the placement of that particle to a new process. The placement process uses the predefined boundaries of the sub-RVE object to generate a random set of coordinates. The newly generated particle is tested against other particles in that sub-RVE for interference checking. During these interference checks, neighboring particles are identified and stored. If the particle placement is found to be valid, the coordinates and neighbors of the particle are saved in a new particle object. If the particle placement is invalid, the particle is resubmitted to the host process for replacement.

2.5. Second iteration results and discussion

The same convergence procedures were followed for testing the second iteration of the placement algorithm. Conductivity convergence simulations were performed while varying RVE parallelization parameters to investigate the effect of parallelization on model fidelity. Ideally, the parallelization of the algorithm would have no effect on the fidelity or output of the model. As is evident in Figure 8A, it was found that the converged conductivities of RVEs with equal size, particle properties, and CB weight concentrations generated via the pseudo-parallel algorithm and the serial algorithms vary. These results show that increasing the degree of RVE parallelization, by increasing the number of sub-RVEs, resulted in an increase in the converged average conductivity. Two potential causes of this increased conductivity are: (1) The parallelization and subsequent re-initialization of the random number generators having coincident seeds, which has been explored by other authors [131, 132], and/or most likely (2) an increased probability density along the BV interfaces due to improper bounding of the sub-RVEs. The second cause will result in more particles being placed along interior BVs, thus

making planes of increased conductivity form along the length of the RVE. The following results show that while not ideal, the observed influence of parallelization is quantifiable and minimal even for highly parallelized simulations.

Computational efficiency of the pseudo-parallel model is shown in Figure 8D. Both the serial and pseudo-parallel simulations were performed on dedicated compute nodes, each with 24 cores (2x Intel Xeon E5-2680 v3) and 64 GB of RAM. The memory demand of the simulations was negligible (less than 1GB). To provide an accurate and fair efficiency comparison between the serial and pseudo-parallel algorithms, the number of cores used for a single simulation is multiplied by the total simulation time (seconds) resulting in units of core-seconds per simulation. The serial model – while not as efficient as the pseudo-parallel model – was considered to be the highest-fidelity model, which was used to produce baseline results for comparison. Because parallelization effects were quantifiable, a compromise between computational time and similarity to the baseline could be made. A parameter was defined to help quantify and compare how increasing amounts of parallelization influenced simulation accuracy and efficiency. The following formula was used to define the degree of parallelization D as:

$$D = \left(\frac{a}{L}\right) N_S \qquad \text{Equation 2-11}$$

where a is the particle diameter in nanometers, L is the side length of the cubic RVE in nanometers, and N_S is the number of sub-RVEs. The converged average conductivity determined at $D = 0.3$, for the case shown in Figure 8A, was found to provide reasonable agreement (within 8.2%) with the serial model's converged averages while also offering improved simulation efficiency. At $D = 0.39$, error was increased significantly to 33.3%. At $D = 0.24$, efficiency was significantly decreased, and accuracy only improved to within 7.2%, which is only marginally

more accurate than $D = 0.3$ with an error of 8.2%. Figure 8B shows the density plots of the reported conductivity values from the simulation results shown in Figure 8A. It is interesting to note the positive skew of the distributions seen in the density plot. This skewness is expected because unlike the probability of generating RVEs with conductive networks producing higher-than-average conductivities, the probability of generating a RVE in which a conductive pathway is realized that results in a lower-than-average conductivity is less likely, especially at weight concentrations about the percolation threshold. To reiterate, RVEs reporting zero conductivity values, in which conductive network formation is not realized, are not recorded for convergence purposes. Lastly, the conductivity (x-axis location) of the density plot peaks in Figure 8B for parallel cases D=0.3 and D=0.24 are within 1.2% of the serial peak location. This agreement indicates that the influence of parallelization is quantifiable and the RVEs produced by both the serial and parallel algorithms at perfect dispersion are statistically very similar. Figure 8C summarizes results of the RVE size convergence study, which shows good agreement between serial and pseudo-parallel models. The converged parallel simulation at 6200 nm shows good agreement with the serial data and the fitted curve.

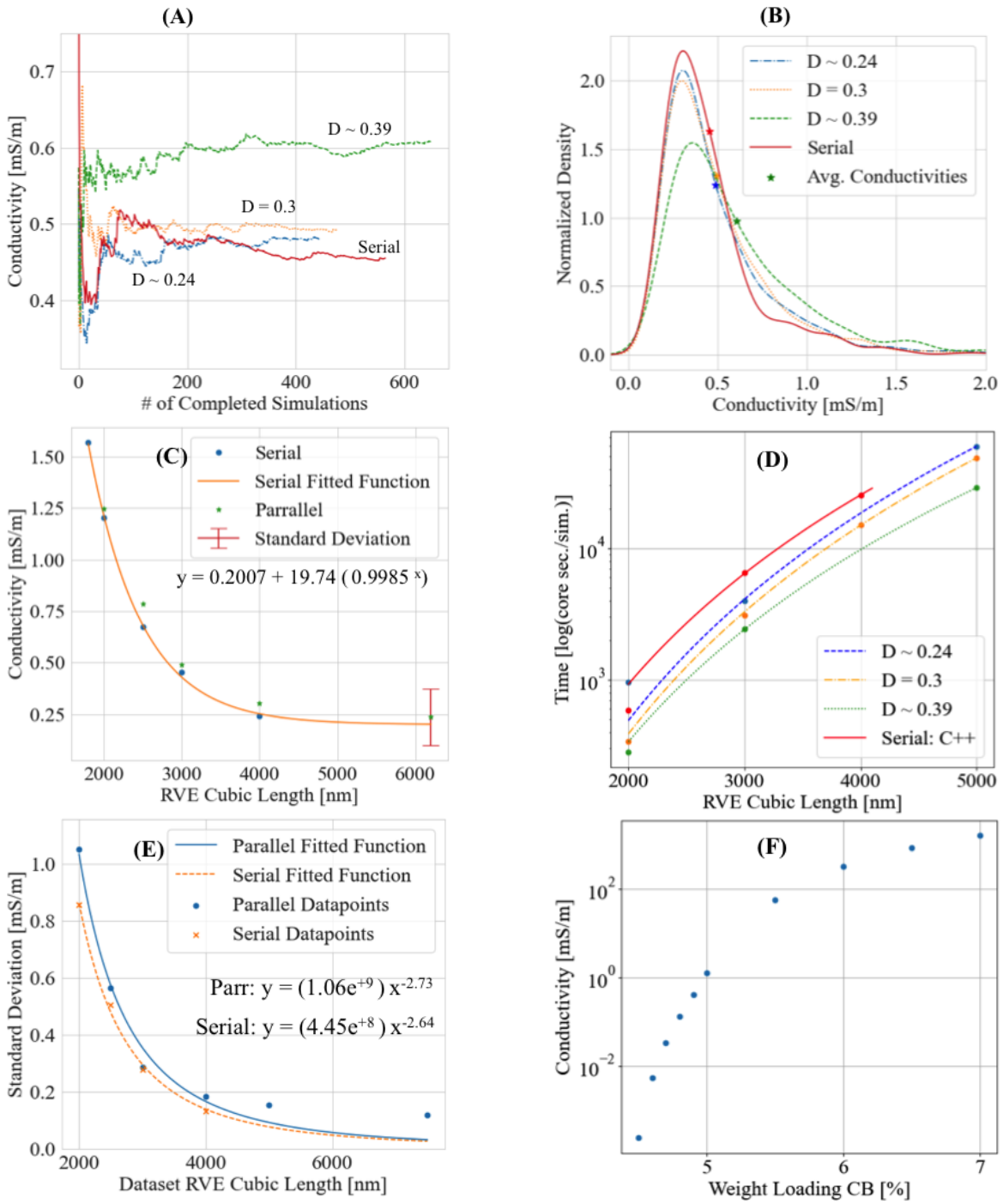

Figure 8 – (A) Moving average convergence of 3000 nm cubic length RVE with varying degrees of parallelization; (B) Density plots of converged average datasets with varying degrees of parallelization; (C) Plot showing convergence of simulated conductivity versus RVE cubic length for serial and pseudo-parallel iterations of the stochastic modeling program; (D) Simulation time vs. RVE cubic length and degree of parallelization; (E) Convergence of standard deviation with increasing RVE size for serial and pseudo-parallel models. Pseudo-parallel model simulated with constant degree of parallelization; (F) Weight loading (mass percentage of CB) vs. converged average conductivity for 5,000 nm cubic length RVEs ($D = 0.3$) considering perfect particle dispersion

Figure 8D shows the relationship between standard deviation, converged by the same aforementioned criteria, as a function of the cubic lengths of the simulated RVEs. Interestingly, the serial simulated conductivity convergence trend more closely follows the fitted power function with increasing RVE size, while the pseudo-parallel data appears to be positively offset. The trends observed in Figure 8E, along with the trends in observed in Figure 8C, confirm that conductivity becomes independent of RVE size beyond 6200 nm. Therefore, the variables representing the electrical characteristics of the matrix and filler materials solely determine the conductivity of such samples. The existence of such convergence defines limitations of repeatability in theoretically perfectly dispersed CB CPC sensor designs on a micro-scale without nanoscale control over the filler material orientation. This repeatability threshold is crucial for the overarching goals of SHM sensor design and implementation.

After determining the influence of RVE size on conductivity, the effect of weight loading percentage could be investigated. Simulation results shown in Figure 8F were generated with an RVE size of 5000 nm considering perfect dispersion of particles in the simulated volumes. The model predicts a percolation threshold between 4.5 and 5.5 percent by weight carbon black for such perfectly dispersed samples, evident from the logarithmic increase in conductivity about that weight loading range.

2.6. Particle agglomeration algorithms

The process of generating spherical elements in a bounded RVE at first seems a remedial task. The complexity of such a task is realized upon comparing and controlling the fidelity of the simulated volumes to physical specimens observed in experiment. In Chapter 3, the fidelity of the final stochastic modeling scheme proposed in this Chapter is investigated experimentally. The chronological order of model development and experimental dispersion realizations are not

consistent with the order in which they are presented in this dissertation. For the sake of continuity, early experimental results from Chapter 3 are shown in Figure 9 to motivate the proceeding sections of this Chapter. Figure 9A is a microscopy image of one of the earliest experimental samples manufactured for model fidelity investigation. The image shows how CB particles (black) tend to agglomerate when mixed with epoxy. This image was post-processed using ImageJ (Figure 9B and D) for comparison to stochastically generated CB CPC RVEs rendered using Ovito [130]. One such rendered RVE, shown in Figure 9C, shows that RVEs generated with perfect dispersion are more comparable to TV static than to similarly concentrated physical CB CPC specimens of comparable dimensions.

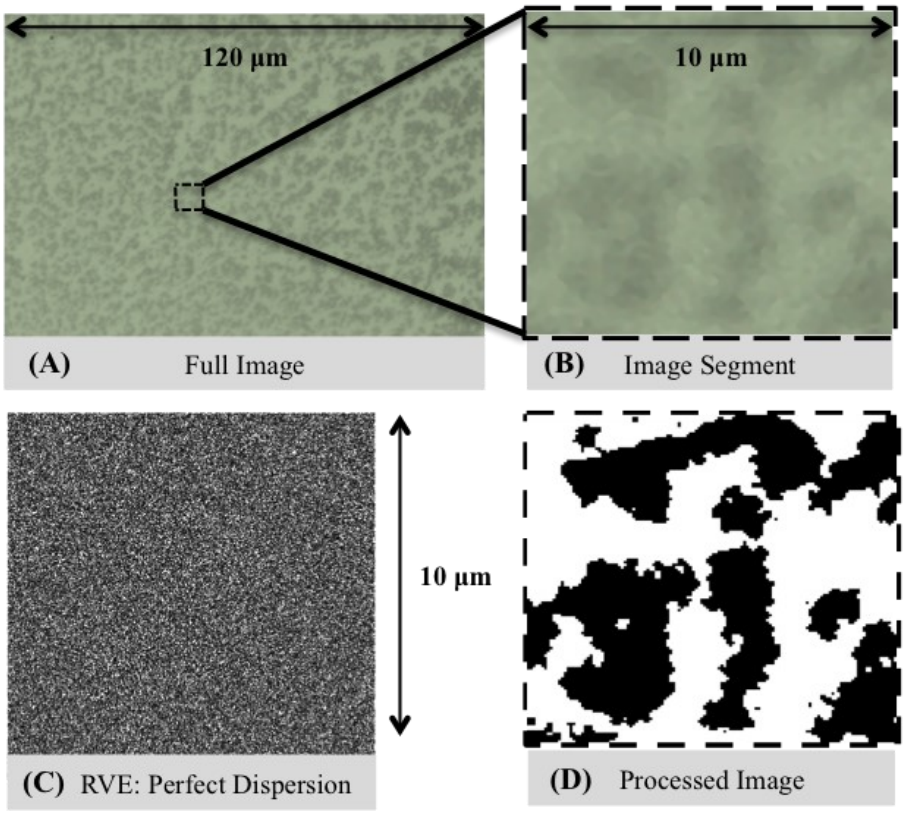

Figure 9 - (A) Microscopy image (Leica VZ700 C) of CPC film; (B) Cropped segment of microscopy image; (C) Stochastically modeled cross-sections of perfect dispersion quality; (D) Post-processing of segment using Image J [133];

From these early investigations, it was obvious that the development of an agglomeration inducing RVE placement algorithm was necessary. CB is often described as colloidal or aggregated, and the shape and size of such CB structures is generally non-uniform. As discussed in Chapter 1, it has been shown that the characteristics of CB CPC are largely dependent on the processes deployed in their manufacture and incorporation into such mixtures. To study such dependence stochastically, comparable CB CPC structures must be generated for simulation. Various agglomeration-inducing algorithms were developed to meet this need, and the results of those developments are discussed in subsequent sections.

2.6.1. Dispersion quality factor method

The first method for influencing agglomeration during the particle placement algorithm was the dispersion quality (DQ) factor method. The DQ method was deployed in the serial iteration the stochastic modeling program. The *DQ* factor is a user-defined unitless floating-point value between 0 and 1 used to influence agglomeration during the placement of particles in the RVE (1 causes perfect dispersion and 0 causes total agglomeration). During the placement of a new particle at a random location in the RVE, the potential indices of neighboring particles are stored for future use by the program. If a newly placed particle has been found to create no interferences, the DQ factor method is then applied. The DQ factor is used to determine placement validity when a particle is placed in the RVE but it is not contacting a user designated number of previously existing particles, *X*. In such an instance, a random number is generated between 0 and 1 and is compared to *DQ*. If the randomly generated floating-point value is greater than *DQ,* the particle placement is invalid and the process is forced to replace the particle.

The DQ factor method proved to be computationally intensive and inefficient. To induce any agglomeration comparable to that observed in Figure 9, the DQ factor had to be set to very

low values (DQ < 0.001). Setting the DQ to such low values resulted in a greatly increased chance of a particle needing to be replaced multiple times, especially at the early stages of the placement procedure when the RVE was relatively empty. Such replacements dramatically affected simulation times, which were increased by multiple orders of magnitude compared to purely random placements. To address this inefficiency, the DQ factor method was modified to create a more efficient procedure: the random seed placement method.

2.6.2. Random seed placement method

The random seed placement procedure is illustrated by the flow chart in Figure 10. The random seed placement method is initiated by the distribution of *seed* particles in the RVE randomly while upholding interparticle interference requirements. Once seed particles have been placed at random, agglomerates are formed through the placement of the remaining particles in the RVE while maintaining a condition of forced agglomeration. Forced agglomeration is achieved by setting the *DQ* variable equal to zero and *X* equal to one. This variable assignment requires a new particle to be in contact with at least one previously placed particle in the RVE for the particle's placement to be considered valid. This method was applied to both serial and parallel iterations of the program with very few code modifications, and was found to be much more computationally effective than the DQ method alone. During forced agglomeration placement, new particle random coordinate generation is still conducted and particle replacement is often necessary, but random seeds in the volume at forced agglomeration placement start greatly improve early placement efficiency. Adjusting the number of seed particles (N_{seed}) in the RVE provides a means of modifying both dispersion and the average agglomerate size in the RVE, thus giving users the ability to create artificially agglomerated CB CPC models.

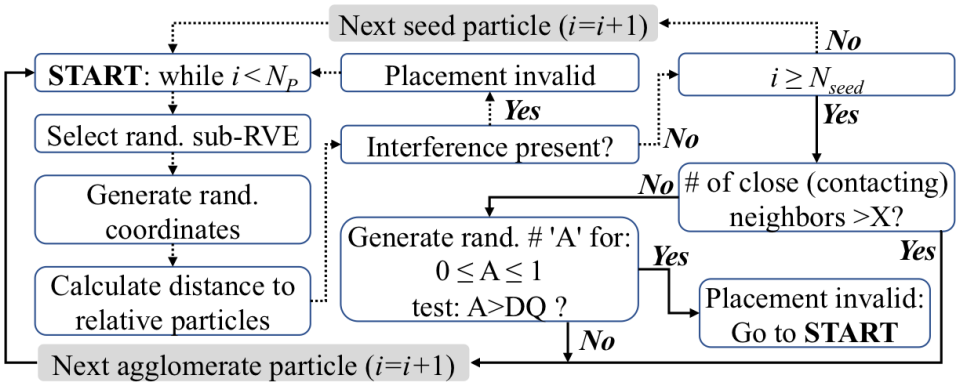

Figure 10 - Flowchart detailing the particle placement procedure followed for both seeding (dotted lines) and agglomeration (solid lines) phases of RVE population

Figure 11B and C shows cross-sections of simulated RVEs generated via the random seed method with various dispersion parameters. Each RVE is populated with a CB weight percentage and dimension comparable to the experimental sample shown in Figure 9A. The random seed method proved effective for efficiently controlling agglomeration characteristics of particles placed in the RVE as demonstrated in Figure 11. The agglomerate structures in Figure 11C are comparable in size to those observed in the post-processed microscopy image segment in Figure 11A. As evidenced in Figure 11, multiple simulation factors can affect the degree of agglomeration realized in particle placements, namely the degree of parallelization, the thickness of the cross-section, and the percentage of random seeds in the volume. While the simulated agglomerate structures in Figure 11 are not an exact match to the microscopy images, they demonstrate that the proposed agglomeration algorithm is capable of tailoring RVE agglomeration characteristics from perfectly-dispersed to highly-agglomerated with quantifiable stochastic simulation parameters.

From Figure 11B and C it was noted that the parallelization of the RVE resulted in the generation of volumes with unrealistic features. Looking closely at the simulated images,

straight-line regions devoid of particles are identified at the locations of the BVs. The realization of such voids influenced further development of the stochastic modeling scheme.

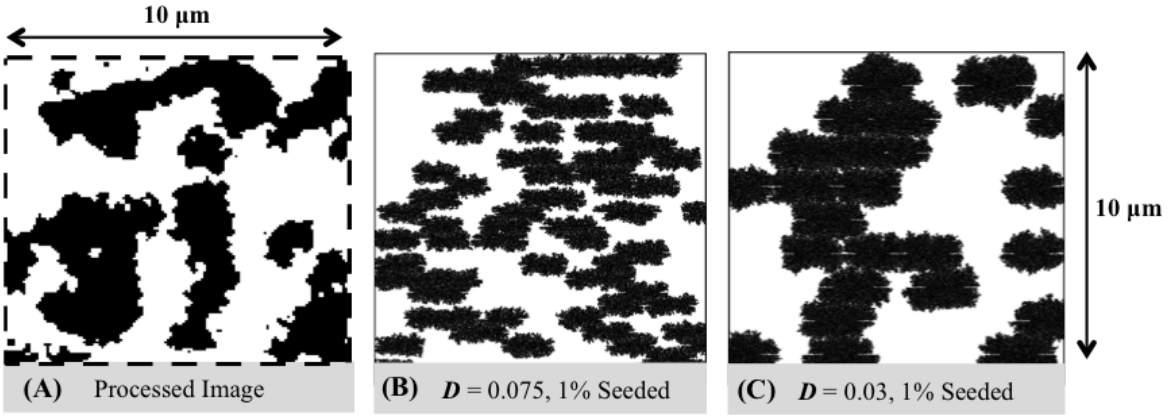

Figure 11 – (A) Cropped segment of microscopy image from Figure 9A; (B) Parallel simulation ($\boldsymbol{D}$ = 0.075) with 1% of particles as random seeds; (C) Parallel simulation ($\boldsymbol{D}$ = 0.03) with 1% of particles as random seeds

2.7. Stochastic model architecture improvement

The stochastic modeling architecture developed up to this point is dependent on the generation of random coordinates for particles to be placed in the RVE. This results in the placing and replacing of particles to force neighboring relationships, causing a dramatic increase in simulation times. Upon parallelization of the volume for improving these simulation times, it was realized that parallelization produced unrealistic features that influenced the reported electromechanical properties of the studied mixtures. This result is highly undesirable, and prompted investigation into improving the efficiency and fidelity of the stochastic modeling architecture for generating agglomerated CB CPC RVEs.

In the random seed placement method, only a small fraction of the total possible placement locations are considered valid, as a particle must be placed in a neighboring relationship with other particles. Rather than randomly selecting the next particle location from a list of valid locations, the current architecture requires a random location to be selected from a

list of both valid and invalid locations after which time-consuming calculations must be performed. The hypothetical notion of collecting valid placement locations in a list was enticing, and prompted a major overhaul of the stochastic modeling architecture.

2.7.1. Index-mapping scheme

A rapid, scalable, and memory-intensive particle placement algorithm was developed to replace the previously detailed stochastic modeling placement algorithm. For this algorithm, an index-mapping scheme was developed. Consider the cubic RVE illustrated in Figure 12B. Each discrete location in the RVE is assigned a unique numbered index. Bit-fields are then created to store binary information about each index including the invalidity of placing a particle at that index (visually represented by red indices in Figure 12A), the existence of a particle centered at that index, and whether or not a particle placed at that index would be in close proximity to preexisting particles in the RVE (visually represented by green indices in Figure 12A). A variable length array containing indices of valid and neighboring placement locations is constantly updated once particles are added to the RVE, accomplished by a simple relative index mapping scheme. This method allows for rapid identification of valid, invalid, and agglomerate producing placement locations without recalculating interparticle distances every time a new particle is placed.

The increase in RVE population speed was quickly realized. The first index-mapping scheme was capable of placing particles at a rate of 1200 particles per second. The model iteration detailed in Section 2.2 placed particles at a rate of approximately 100 particles/second when DQ = 1, and for DQ < 1 the rate of particle placement was less than 50 particles/second. While the improvement in placement speed was realized, the fidelity of the model was still found to be lacking. Figure 12C shows an example RVE populated with the new index-mapping

architecture using the same random seed placement method. The RVE was generated with comparable parameters to the image and renderings shown in Figure 11A-C. The sphericity of the agglomerations was found to be a consistent feature of the index-mapped random seed placement method. The final proposed iteration of the stochastic modeling program was motivated by discoveries from recent literature on the simulation of fractal CB aggregate structures.

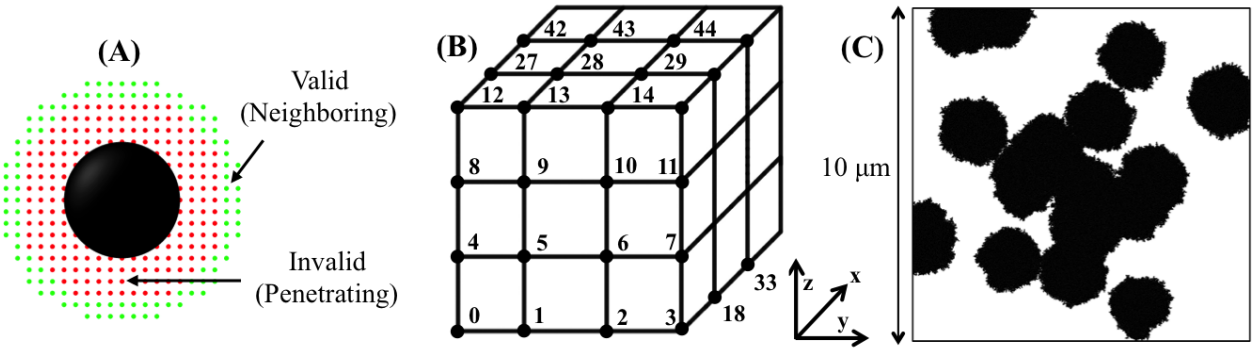

Figure 12 – (A) Simulated primary particle with mapped valid (green) and invalid (red) placement indices, and (B) Illustrated RVE index mapping scheme; (C) Example RVE populated with the seed placement algorithm and the newly implemented index-mapping scheme.

2.7.2. Fractal aggregate placement algorithm

The fractal nature of CB aggregates is well documented, and a comprehensive literature review of this topic is presented by Donnet *et al.* [134]. In keeping with that work, the term aggregate will be used to refer to a collection of CB spherical primary particles, as shown in Figure 13A and B. The term agglomerate will be used to refer to collections of aggregates that appear to be contacting. Research on computational modeling of fractal aggregates is vast, and a comprehensive review of the field is offered by Meakin [135].

In the final iteration of the stochastic modeling program, a fractal aggregate generation tool, FracVal [136], was used to generate 10,000+ aggregates of monodisperse spherical particles whose coordinates were stored for placement in the proposed program. Example aggregates

generated via the FracVal software are shown in Figure 13A and B. The number of primary particles per aggregate, particle radius, fractal dimension, and pre-factor parameters used to generate the aggregate coordinate files used in the final proposed model were 100, 15-nm, 2.7, and 0.7 respectively. These values fall within ranges reported in recent literature, and were held constant for purposes of exploring other pertinent simulation parameters [98].

As noted by Coupette *et al.*, it is difficult to distinguish agglomerates from aggregates in bulk materials experimentally [98]. Van der Waals attraction between aggregates result in weakly linked agglomerates, varying in apparent size and shape. The agglomeration of the generated aggregates is controlled via additional simulation parameters in the proposed stochastic modeling program. These additional simulation parameters are the number of aggregates to be placed at random, the number of aggregates to be placed via forced agglomeration, and the number of individual particles to be placed via forced agglomeration. After these user defined simulation parameters have been input, each coordinate file from the bank of FracVal aggregates is loaded into memory. Each particle in the FracVal aggregate file is assigned a relative index for rapid integration into the global coordinate/indexing system of the RVE. The placement algorithm begins by randomly placing a user-defined number of seed aggregates in the RVE. Once the seed aggregates have been placed, a percentage of the remaining particles are placed as FracVal aggregates using a forced agglomeration sub-routine. In this sub-routine, a random index in the volume is selected followed by the selection of a random aggregate from the collection of FracVal aggregates. The relative aggregate indices are transformed according to the selected random index, and a loop is used to determine if (1) all of the placement indices of the new aggregate are valid, and (2) if any of the particles have been placed in close proximity to particles of previously placed aggregates. If both (1) and (2) are true

the placement is considered valid, the bit-fields are updated, and the next aggregate is placed. Following the placement of the aggregates in forced agglomeration, individual particles are placed in the RVE under forced agglomeration until the desired CB concentration is met. These individual particles constitute the fill percentage variable *f*, which is defined as,

$$f = \left(1 - \frac{N*100\left[\frac{particles}{aggregate}\right]}{T-S*100\left[\frac{particles}{aggregate}\right]}\right) * 100\% \qquad \text{Equation 2-12}$$

where *T* is the total number of particles in the RVE, *S* is the total number of seed aggregates, and *N* is the total number of aggregates placed via forced agglomeration. After all particles have been placed, the coordinates of each particle are saved for post-processing.

Figure 13C shows an example RVE generated using the fractal aggregate placement algorithm. Comparing this RVE with the experimental image in Figure 11A and outputs of previous iterations (Figure 11B and C, Figure 12C), it is clear that the fractal aggregate placement algorithm is a vast improvement in terms of model fidelity. The structure of the agglomerates more closely mimicked the samples observed in preliminary experimentation, and thus the model was deemed capable of representing realistic CB CPC configurations.

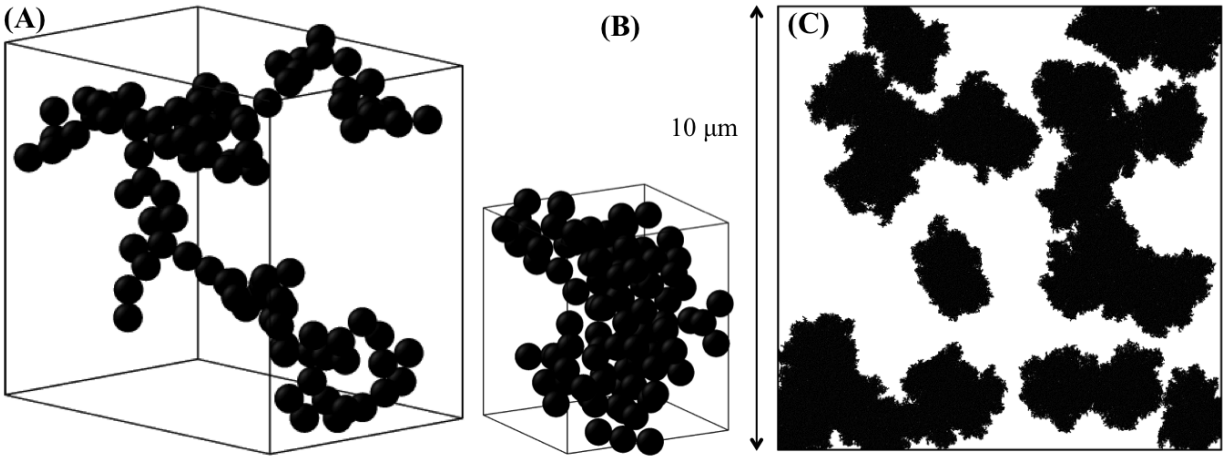

Figure 13 – Example FracVal aggregates consisting of 100 particles with radii of 15-nm, pre-factor = 0.7 and: (A) fractal dimension = 2.1; (B) fractal dimension = 2.7; (C) Rendering of example RVE generated with fractal aggregate placement algorithm. RVE dimensions and CB concentration comparable to images and renderings of Figure 11A-C and Figure 12C.

2.8. Chapter summary

This Chapter presented the development of a stochastic modeling program for purposes of studying and predicting the electromechanical properties of CB CPC materials. Multiple programming languages were deployed including Matlab ®, Python, and object-oriented C++. Physical constraints and assumptions applied in the numerical modeling of spherical CB elements are discussed, and fundamental questions of model accuracy and fidelity are presented.

Early iterations of the stochastic modeling program (subsequently termed the serial model), developed in Matlab ® and later C++, were designed to utilize a single computing process for the generation of purely random RVEs and the analysis of random resistor networks contained within. Assessment of the numerical convergence of the serial model was achieved by generating hundreds of stochastic RVEs and examining the moving average of the reported conductivities, excluding any instances where no network existed in a simulated RVE.

Conductivity moving average convergence for a single set of simulation parameters (RVE cubic length, weight fraction CB, etc.), determined by a standardized convergence criteria, was found to require more than 500 conductive RVEs. After such realization, a single simulation parameter (RVE cubic length) was increased and the same conductivity convergence procedure was performed. This process was repeated with increasingly larger RVEs, revealing a dependence of converged average conductivity on the overall size of the simulated RVEs. An exponential function was found to be in good agreement with the converged average conductivity vs. RVE cubic length trend, with negligible RVE cubic length influence on conductivity for perfectly dispersed RVEs with cubic lengths greater than 6200-nm.

The serial model program runtimes at such RVEs scales were impractical. RVE generation via the serial random placement algorithm was found to be the most computationally

expensive subroutine of the program. Load distributed and pseudo-parallelized particle placement algorithms were developed as a consequence. A successful pseudo-parallelization scheme consisting of interdigitated sub-RVEs and BVs was detailed. Investigation on the effect of parallelization on converged average conductivity found slight variation between serial and pseudo-parallel models. Comparison of the distribution of reported conductivities from serial and pseudo-parallel models revealed a positive skew in the pseudo-parallel data, while the mode of the distributions were found to be in good agreement. Improvements in computational efficiency were realized, and pseudo-parallel model predictions were in agreement with the exponential convergence prediction from the serial data.

Early experimental model fidelity validation efforts revealed drastic differences between simulated RVEs and comparable physical CPC specimens. Agglomeration features realized in experimental samples, discussed in Chapter 3, prompted further model particle placement algorithm development. Multiple agglomeration inducing schemes were tested and found to produce RVEs containing more realistic agglomeration features through random coordinate generation and forced agglomeration placement rejections/replacements. Such particle replacements drastically decreased simulation efficiency, and prompted further model evolution.

An overhaul of the placement algorithm, using an index-mapping scheme, dramatically improved simulation efficiency. Placement of single spherical particles via random seeding and forced agglomeration was found to produce agglomerates with tailorable size and distribution. Renderings of such RVEs revealed agglomerates with consistently spherical geometries. Coincident with this realization, literature regarding the fractal nature of CB aggregates and spherical element aggregate modeling schemes was discovered.

The model was further developed to generate RVEs containing fractal aggregate structures. Monodisperse, spherical element-based, fractal aggregate coordinate files were generated using FracVal, an open-source program discovered in the literature. The stochastic modeling program accesses the aggregate coordinate files and subsequently generates RVEs with varying dispersion characteristics. User-defined variables pertaining to aggregate placement randomization and agglomeration are introduced for tailoring RVE dispersion. The renderings of the resulting index-mapped RVEs exhibited the most realistic agglomeration features modeled yet, all while vastly improving particle placement algorithm efficiency.

CHAPTER 3

VALIDATION OF STOCHASTIC PLACEMENT ALGORITHM FIDELITY

3.1. Physical CPC specimen investigation

In Chapter 2, the development and improvement of the stochastic model placement algorithm was discussed in detail. The realization of necessary improvements via early experimental methods was briefly mentioned for contextual purposes. In this Chapter, the experimental methods used to characterize the dispersion of CB in CPC specimens are discussed in detail.

The simulated RVEs were modeled after a physical CPC specimen composed of commercial-grade constituents. CB can be purchased in many different forms. The CB used in this study, VULCAN XCMAX22, was donated by CABOT Corporation. This particular variety of CB is classified as traditional furnace black, and is packaged in powder like form as shown in Figure 14B. The properties of the suspending matrix in the simulated RVEs were modeled after EZ-Lam® 60-Minute Epoxy, a two-part epoxy system with a working time of 60-minutes and a cure time of 24 hours at room temperature. This particular phenolic resin system was selected for simplicity and ease of preparation.

3.1.1. Mixture preparation methodology

The manufacturer defines the viscosity of the workable mixture at 700 CPS. Although the manufacturer offers no individual assessments of each constituent's viscosity, the resin in this system was found to be noticeably more viscous than the hardener. Viscosity plays an important role in the dispersion of CB in a suspending matrix. Incorporation of CB filler into polymer matrices that are more viscous (e.g. rubber) require high-shear mixing methods such as calendaring or mechanized stirring, while CB can be incorporated into less viscous polymer matrices with fluid stirring mechanisms such as ultrasonic baths or probes. In initial investigations, less viscous CPC mixtures were desired due to the mixing utility available, an ultrasonic homogenization probe (Boshi Electronic Instrumentation).

The manufacturer prescribed ratio of resin to hardener by weight is 100:44. In an attempt to keep the resin and hardener separated during ultrasonic homogenization, the CB was first incorporated solely into the resin. Even though the resin was more viscous, the resin/CB mixture was significantly less viscous than a similarly loaded hardener/CB mixture. However, the resin/CB mixtures were found difficult to process via ultrasonic homogenization at CB weight concentrations greater than 1%. For such samples, a calendaring process, via a 3-roll mill (Torrey Hills Technologies), was deployed to improve initial incorporation of CB into the resin.

3.1.2. Constituent material characterization

The resin of the epoxy system is very transparent, and the hardener has a yellowish hue. Initial investigations of cured specimen showed that the mixture tends to lighten as it cures, which is favorable for through thickness imaging. Characterization efforts were then focused on validating the manufacturer specifications of the CB variety used in the study. Resin was first loaded with CB at a weight fraction of 1%. The resin/CB mixture was agitated via ultrasonic

homogenization, hardener was then added, and the final mixture was hand stirred. The final mixture was poured into a Kapton tape slot mold and cured for 24 hours. The sample was sent to the KSU Microscopy Facility for inspection via transmission electron microscopy (TEM). The sample was suspended in imaging resin and sliced with a microtome to obtain cross-sectional samples approximately 90 nanometers thick. The cross-section samples were absorbed onto 200 mesh copper grids and imaged at 100kV on a CM-100 TEM. The TEM image (Figure 14A) shows the natural tendency of the CB particles to exist in aggregate and agglomerate form. Measurements performed by the TEM are in agreement with the manufacturer's description of the average particle diameter, which is approximately 30 nanometers in magnitude.

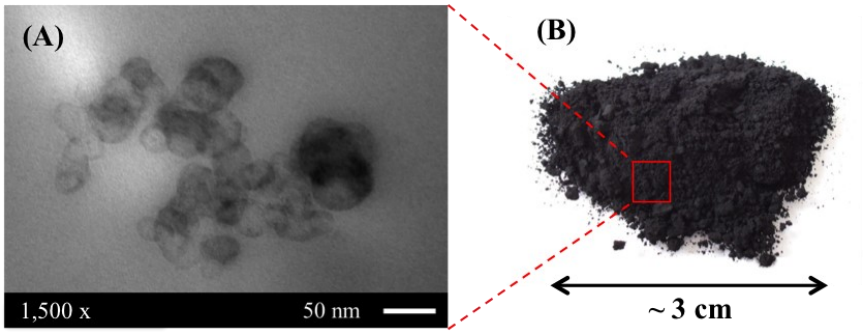

Figure 14 – (A) TEM image of VULCAN© XCMAX22 embedded in imaging resin; (B) CB sample in bulk packaged powder form

3.1.3. Investigation of CPC dispersion via optical microscopy

While validating the average CB primary particle diameter, the colloidal structure of CB was realized prompting further investigation of CB structures in cured CPC. Of the dispersion characterization methods discussed in Chapter 1, optical microscopy was selected due to its availability and simplicity. Various CPC mixtures were prepared with weight loadings of CB ranging from 0.1% to 5%. At lower weight loadings (< 1% by weight CB), the cured CPCs were noticeably more translucent as expected. However, low weight loading samples with thicknesses

on the order of millimeters were still relatively opaque. Imaging such samples via optical microscopy yielded very little useful information.

3.1.3.1. CPC thin-film manufacturing and characterization methods

Sandwiching mixtures between glass microscopy slides (AmScope), the first optically translucent CPC film samples were generated. These films were significantly more transparent than any previously cast samples. By depositing a droplet of CPC mixture onto a slide, and pressing the mixture into a transparent film, individual CB agglomerates in the mixture became distinguishable as shown in Figure 15A. This sandwiching method did have a few drawbacks. First, the process of pressing microscopy slides together frequently resulted in CB structures in the cured CPC films that appeared to be smeared as shown in Figure 15B. This phenomenon was seemingly unavoidable. Secondly, assessment of film thickness for direct comparison to stochastic simulation was not easy. To estimate film thicknesses, sandwiched microscopy slide samples were freeze-fractured by submerging the sample in liquid nitrogen for 60s before fracturing the sample over a table's edge. Fractured cross-sections were then observed via optical microscopy to determine film thicknesses. This method ultimately proved ineffective, and other film manufacture and measurement systems were pursued as a consequence.

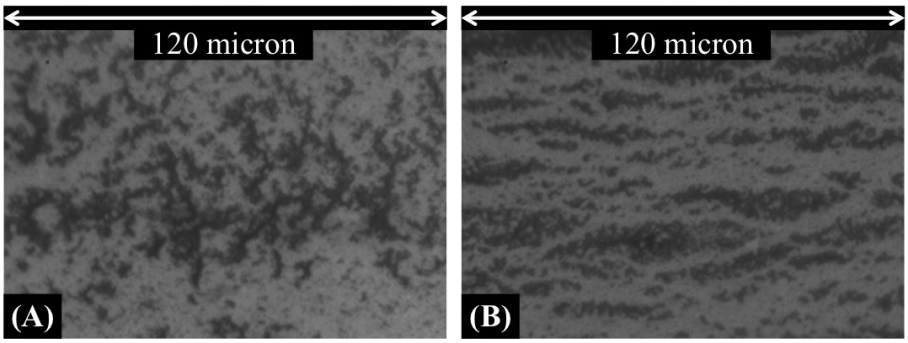

Figure 15 – Cured CPC films of 3.5% by weight CB sandwiched between glass microscopy slides imaged at 100x magnification. (A) CPC film exhibiting more random dispersion of CB agglomerates; (B) CPC film with CB agglomerates that appear to be smeared in one direction

After conducting research on profilometry measurement systems in the marketplace, an optical profilometer manufacturer, Filmetrics, was discovered. Filmetrics graciously agreed to test the efficacy of their measurement systems for our research. Film coated microscopy slides to be sent to Filmetrics were prepared using a hybrid form of the aforementioned sandwiching method. First a droplet of CPC mixture with a weight concentration of 3.5% CB was deposited on a microscopy slide. A quick release film was then placed between the first and second slides to allow removal of the top slide and release film after curing. The resulting CPC coated microscopy slides were then sent to Filmetrics to be profiled. Image and statistical analysis of the Filmetrics experiments are shown in Figure 16 below. Figure 16A shows a top-view image of the sample, Figure 16B shows a 2-D stitched surface plot, and Figure 16C shows a single profile quantifying the thickness of the film along line x-x'. These results showed the large variations in thickness produced by the sandwich method. Additionally, direct measurement of film thickness via optical methods was complicated by the absorptivity of the CB in the films. For this reason, a step height measurement method was used. The step height measurement requires an assumption that the neat surface of the microscopy slide is flat and smooth relative to the deposited CPC film. Later in this Chapter, that assumption was found to be inappropriate. Still, the profilometry measurement system was still considered a more consistent approach than previous attempts.

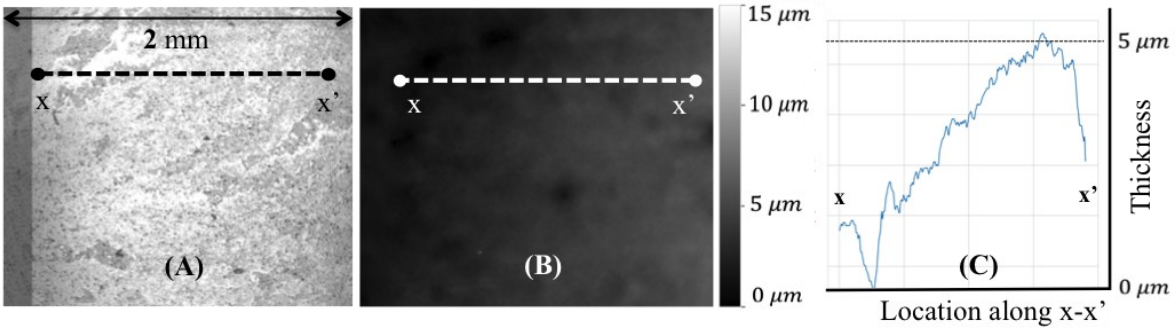

Figure 16 – (A) Image of CPC film on microscopy slide; (B) Filmetrics optical profilometry of CPC film; (C) Height distribution along the line spanning from x to x'

A stylus profilometer (Dektak 150), discovered inoperable in a collaborator's lab, was repaired and utilized for characterizing film thickness. The stylus profilometer is equipped with a motorized XY-stage, along with a sub-micron precision scan-direction motor, which translates the stage to perform a single scan. The operating principle of stylus profilometers is illustrated in Figure 17. The sample to be profiled is first loaded onto a motorized translational stage. The stylus is lowered until it is contacting the surface of the sample, and the stage/sample is slowly displaced. While the stage is translating, the dragging stylus is displaced by the variation in sample height, which is quantified using a mirrored laser and spatially sensitive photodetector. The resulting measurements are output as a CSV file to be post-processed. Slope bias, resulting from the slope of the translational stage, is inherent in the output of the system, and is illustrated by the plot in Figure 17. This slope can change dramatically by picking up the sample from the stage and replacing it at a different stage location.

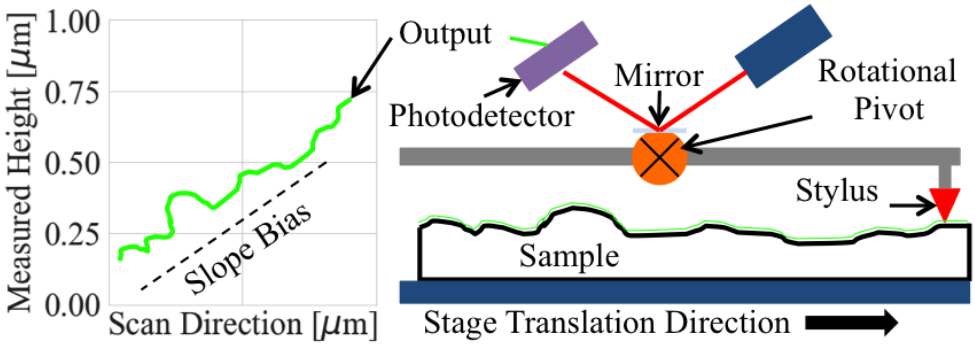

Figure 17 – Illustration of the operating principle of a stylus profilometer measurement system demonstrated with an arbitrary sample.

With the profilometer revived, various substrates were profiled to test their viability for film thickness characterization. First, precision silicon wafers were profiled and the resulting datasets revealed extremely low surface roughness and flatness statistics consistent with manufacturer specifications. Silicon wafers were fairly costly, and a means of reusability had not

yet been identified. For these reasons, alternatives were investigated. Laboratory grade microscopy slides, used in previous sandwich experiments, were then profiled. While the microscopy slides were assumed relatively uniform, smooth, and feature free, profilometry scan data revealed surface features with heights on the order of 1 to 2 microns. Such surface features were considered unfavorable due to previous estimates of manufactured film thicknesses (1 to 5 micron). Profilometry scans of laboratory grade (No. #1.5H) precision microscopy cover slips were found to have significantly improved surface quality, exhibiting very few surface features with heights greater than 0.1 micron. Cover slips were identified as the most precise and reasonably cost-effective substrate for the CPC film characterization study.

3.1.3.2. Spin-coated CPC films

While the modified sandwich method was moderately successful, greater control of film thickness and consistency was desired. Of the various methods of film generation observed in the literature, spin coating was identified as a method that could be replicated with cost-effective components from the lab. The first spin coater was constructed from an old hard disc drive (HDD). The HDD was disassembled and stripped of all its components except for the press-fit brushless DC motor. An electronic speed controller (ESC), powered via a digital power supply, was used to vary the speed of the motor in a controlled manner. A 3D-printed splashguard was installed using existing fixture mounts on the HDD frame, and a 3D-printed cover slip mount (Figure 18A) was press-fit to the rotor.

The highly concentrated CPC mixtures prepared in previous studies were very viscous, and images from early CPC films were densely populated. As shown in Figure 15, distinguishing single agglomerates from these images is difficult. It was hypothesized that by reducing the concentration of CB in the mixture, individual agglomerate and aggregate features could be more

easily identified and thus quantified. Additionally, reducing CB concentration lowered the viscosity of the mixture, which was preferred for spin coating. A new master batch of CB and resin was made by first measuring quantities using an analytical balance then combining constituents by hand stirring before shear mixing via a 3-roll mill. The content of CB in the master batch was controlled to produce cured CPC films containing approximately 0.25% CB by weight. Quantities of the master batch were isolated in a beaker and a thinning agent (200-proof ethanol) was added at a ratio of 0.5 parts thinner to 1 part resin. The sample was further agitated in a precise, varied, and quantifiable manner via the ultrasonic homogenization probe prior to the addition of the hardening agent. The hardening agent was then added to the mixture, and the mixture was hand-stirred prior to being deposited on the spinning cover slip by a plastic laboratory dropper.

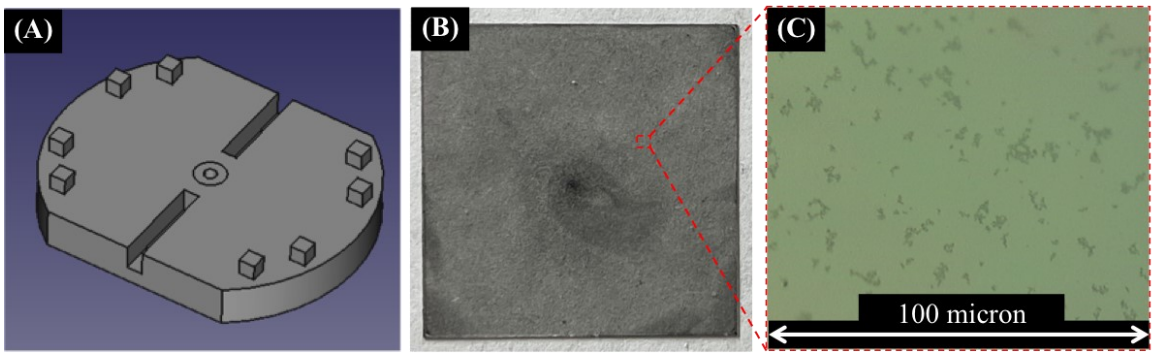

Figure 18 – (A) Cover-slip spin coating motor mount; (B) CPC film-coated high-precision cover slip; (C) Microscopy image of CPC thin film imaged at 100x magnification

Multiple spin coating deposition methods were tested including static mixture deposition, low-speed deposition, and high-speed deposition. A strobe tachometer was used to estimate the rotational velocity, α, of the sample. Depositing the mixture at static and low speeds, the CPC mixture tended to streak off of the spinning cover slip. High-speed deposition ($\alpha > 2000$-rpm) was found to produce consistent and repeatable film coverage, such as the CPC coated cover slip

shown in Figure 18B. Microscopy investigation of the resulting films (Figure 18C) revealed unique CB structures that were clearly defined.

The initial imaging results were promising. Film thickness quantification was attempted using the step-height profilometry method. Lengthwise sections of the CPC film were abrasively removed from the coated cover slips to create flat references. Step measurements proved to be difficult as the cover slips tended to be easily displaced on the profilometer stage while the stylus was being dragged across their surface. In addition, the waviness and thickness variation of the cover slips limited the extrapolation of the scored reference plane. To visualize this, examine the neat profiles shown in Figure 20A. The thickness of the cover slip is shown to vary significantly from one end to the other. As a result, the further from the location of the scored reference plane, the more uncertain the film thickness estimation becomes.

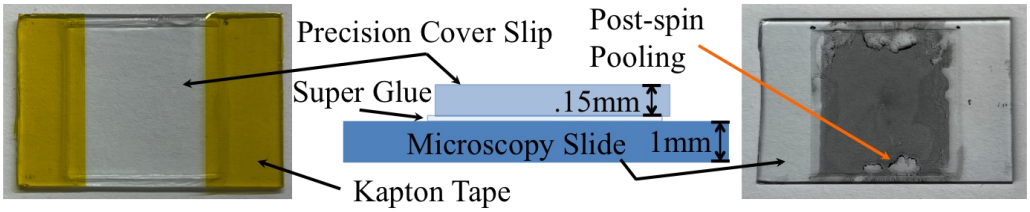

Figure 19 - (Left) Clean sample prepared for spin coating; (Center) Cross-sectional view of sample layered configuration; (Right) Sample post deposition of nanocomposite mixture exhibiting undesirable pooling.

To reduce uncertainty and improve the consistency of the film thickness measurement process, a more robust substrate, illustrated in Figure 19, was developed. The improved substrate consists of a precision quartz cover slip, pre-cleaned with 98% isopropyl alcohol, mounted on a laboratory grade microscope slide using transparent super glue (Loctite). Kapton tape covers regions of the glass slide and cover slip substrate maintained for removal of slope bias from the resulting film thickness measurements. Pristine-mounted samples are first topographically mapped using the profilometer. The pristine samples are then plasma cleaned (Harrick Plasma)

to improve the wettability of the substrate. As shown in Figure 19, initial spin-coating attempts with the aforementioned composite constituents produced non-uniform films susceptible to droplet formation and edge pooling. To combat this phenomenon, a 3D printing grade photopolymer resin (Anycubic) was incorporated into the mixture by hand stirring at a ratio of 1 part phenolic resin to 1 part photopolymer coincident with the addition of the hardening agent just before the deposition of the films. Immediately following deposition, the samples are exposed to high-intensity UV light (λ = 405nm, 40W) in order to reduce the mobility of the film during curing. After the films are cured for 24 hours, the samples are topographically mapped again. Comparing before and after topographies, the thickness of the cured film is defined.

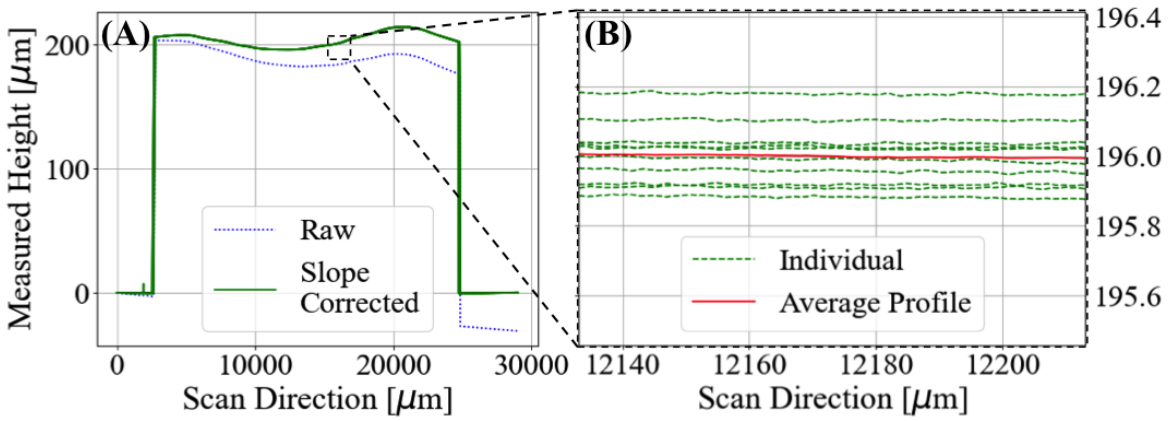

Figure 20 – (A) Plot of multiple scans of the same sample performed after removing and replacing the sample on the profilometer stage and (B) enlarged plot section showing the average profile (solid) generated from the individual scans (dashed)

The average inherent measurement error was estimated by profiling a neat sample substrate multiple times, and calculating the variance between the reported datasets. The profilometry data used in this estimation is enlarged in the plot of Figure 20B. To find the average measurement error, 10 profilometry scans were performed on a single sample at the same location. Figure 20A shows a plot of the resulting datasets before (denoted as “Raw”, dotted line) and after slope bias removal. In the plot of Figure 20A, the waviness of the adhered

cover slip (the "step" portion of the curves) is also observed. Data from the cover slip region of the curve were combined to create an average profile, displayed as the solid red line in Figure 20B. Each individual profile was then compared to the average profile, and the absolute differences were averaged to a value of approximately 125-nm, with a standard deviation of 60-nm. Considering the average thicknesses of the films in the dispersion characterization study ranged from 1.5 to 1.8-μm, the average measurement error was estimated between 8% and 10%. This error was deemed acceptable considering the uncertainty of available alternative measurement methods.

CPC mixtures of 0.25% by weight CB were spin-coated using the HDD spin coater and characterized using this method. Initial estimates of the resulting average thickness of the films were greater than anticipated ($t_{avg} \cong 5\text{-}\mu\text{m}$). Considering the goal of comparing simulated RVEs directly to physical CPC film samples, reducing the thickness of the imaged films was desired to reduce overall simulation times. The resulting thickness of spin-coated polymer solutions is typically affected by the rotational speed of the sample, physical properties of the constituents in the solution, and ambient conditions among other factors [137]. The concentrations of CB, resin, hardener, and ethanol were maintained constant in all experimental samples to focus the study on the effects of variations in the preparation of the spun mixtures. The HDD spin coater was incapable of achieving rotational velocity greater than 3000-rpm, so a larger DC brushless motor was purchased. The new motor could easily achieve speeds greater than 15000-rpm, but for safety reasons the maximum rotational velocity tested was 12000-rpm. CPC mixtures at 0.25% by weight CB, with thinner concentration comparable to previous attempts, were spin coated while varying spin coater rotational velocity from 3000 to 12000-rpm. The samples were allowed to cure for 24 hours before they were characterized via profilometry. Figure 21A shows the

before and after profiles along the same trajectory across the sample. Once again, the importance of slope bias removal is noted. The surface plot in Figure 21B is constructed by stitching together the film thickness data derived from the set of 14 before/after profiles. The plot shown in Figure 21C shows the relationship between the spin coater rotational velocities versus the resulting average thickness of the CPC films produced. As expected, the greater the velocity during deposition and spinout, the thinner the resulting CPC film.

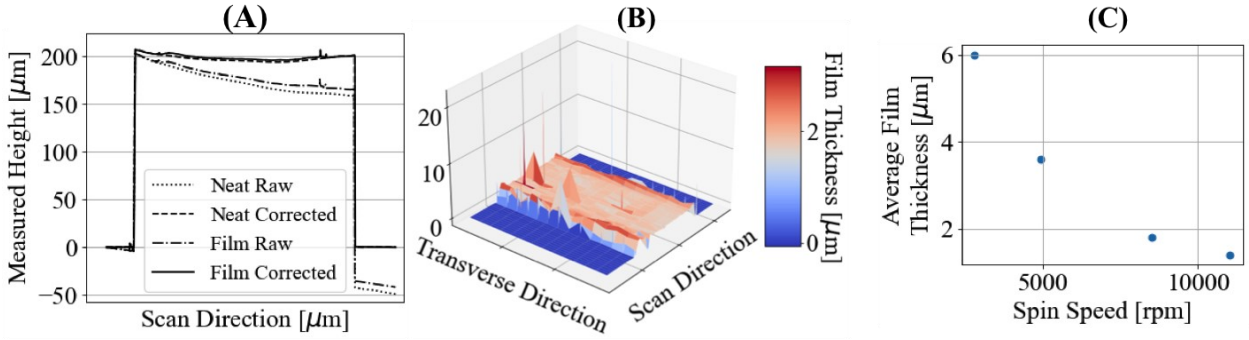

Figure 21 – (A) Plot showing neat/post-spun profiles and the significance of slope bias removal; (B) Surface plot of cured CPC film constructed from 14 scans; (C) Average film thickness versus rotational velocity of sample during spin coating deposition and spinout

Observing surface plots similar to that shown in Figure 21B, it was found that the thickness of the deposited films varies significantly. This thickness variation is most notable at peaks and valleys of convex and concave regions of the substrates. In an attempt to quantify the variation in film thicknesses caused by substrate waviness, 10 samples were spin-coated at constant speed of 10,000-rpm. The mixture deposited was once again considered very well mixed. Of the 10 samples spun, the average standard deviation of the thickness was approximately 350-nm. Thickness measurements within 3-mm of the cover slip edges were omitted from this variance estimation as edge buildup can be observed in the plot of Figure 21A. These edge regions were also excluded during microscopy imaging.

3.2. Profilometer measurement and image location correlation

The variation in film thickness about the sample was significant enough that recording a single thickness value for all microscopy images seemed insufficient. To provide each image with more accurate and localized film thickness information, a coordinate system correlation was developed to transfer profilometer data to a custom motorized microscopy stage built specifically for this purpose. The motorized microscopy stage was designed with a step resolution of 0.05-mm. Figure 22A is a screenshot from the profilometer software showing an image from the system's live feed camera, equipped for sample alignment purposes. In that image, the corner of a CPC film sample substrate can be seen. Figure 22B illustrates the problem of aligning the coordinate systems of both the profilometer and the motorized stage. To simplify the problem, the profilometer stage X and Y-axes are assumed to be perfectly perpendicular, the scan direction axis is assumed to be parallel to the profilometer stage Y-axis, and the machined edge of the microscopy slide is assumed to be perfectly straight. Before each profilometry scan is initiated, a marked edge of the sample is aligned with the profilometer Y-axis, and the stage is navigated so that the optical datum of the sample (Figure 22A) is in the center of the live feed image (alignment cross-hairs of software not shown). This alignment process ensures each profilometry scan begins at the same location with the sample in the same orientation.

Once a sample has been characterized via profilometry, preferable target-imaging locations are identified programmatically, avoiding regions with greatly varying thicknesses. The coordinates and thickness statistics of each identified target location (relative to the optical datum) are stored in a file that is accessed by a Python script for controlling the motorized microscopy stage. The sample is mounted to the motorized microscopy stage using double-sided tape. The optical datum of the sample is centered under the objective of the microscope

(AmScope ME520T) equipped with an autofocus camera (Imaging Source - DFK MKU130-10x22). By assuming that the machined edge of the sample is perfectly straight, a coordinate transformation can be performed to generate spatial coordinates from the profilometer data for commanding the motorized microscopy stage. Using a gridded microscopy slide, the navigation error of the motorized microscopy stage was found to be approximately $\pm$ 0.1mm. This was deemed acceptable considering the incremental distance separating the profilometry scans was 1-mm.

The total area captured via microscopy at each magnification was calculated using a calibration slide. This capture area was used to determine how many images could be acquired from each sample without overlapping images. Magnifications of 10x, 40x, and 100x were found to capture circular images of approximately 4-mm, 1-mm, and 0.5mm in diameter respectively. Square images are then cropped from the center of those circular images (i.e. 10x cropped to 2.5-mm side length) via a Python script. The resulting images are post-processed using the ImageJ particle analysis algorithm [133].

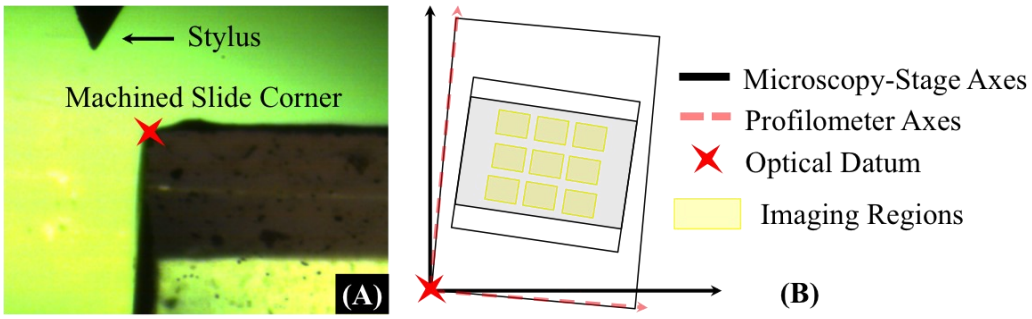

Figure 22 – (A) Screenshot from profilometer GUI showing sample positioning camera used to navigate profilometer stage to starting position at the optical datum; (B) Illustration of the coordinate systems for correlating profilometry measurements to spatial locations for imaging by aligning sample via microscopy slide machined corner (optical datum)

3.3. Statistical comparison of simulated images to optical micrographs

First, the effect of rotational velocity and CPC film thickness on the optical characteristics of the nanocomposite films was investigated. Figure 23 shows microscopy images of spin-coated nanocomposite samples dynamically deposited at varying rotational speeds and spun for 60 seconds at constant speed after deposition. CB-resin from the master batch (detailed in Section 3.1.3.2) was diluted with ethanol and the mixture was homogenized via an ultrasonic probe for 12 minutes with an estimated applied energy of 17-kJ From the microscopy images in Figure 23A-C, there are clear differences in the apparent size and distribution of CB agglomerates between films of varying thickness. As film thickness increases, the agglomerates in the images appear to grow larger. Matching stochastic film RVEs were generated for comparison (Figure 23D-F), and the trend was replicated. The 6-μm thick stochastic film RVE (Figure 23D) contained approximately 9 million CB particles, consumed 115-GB of memory, and took just less than 3 hours to complete. For comparison, the 2-μm thick stochastic film RVE (Figure 23F) contained 3 million CB particles, consumed 35-GB of memory, and took just less than 1 hour to complete. While the influence of thickness on the optical characterization of dispersion in bulk nanocomposites was realized, computational demand and time limitations were influential in the decision to limit the scope of the research presented in this dissertation to nanocomposite films less than 2-μm in thickness.

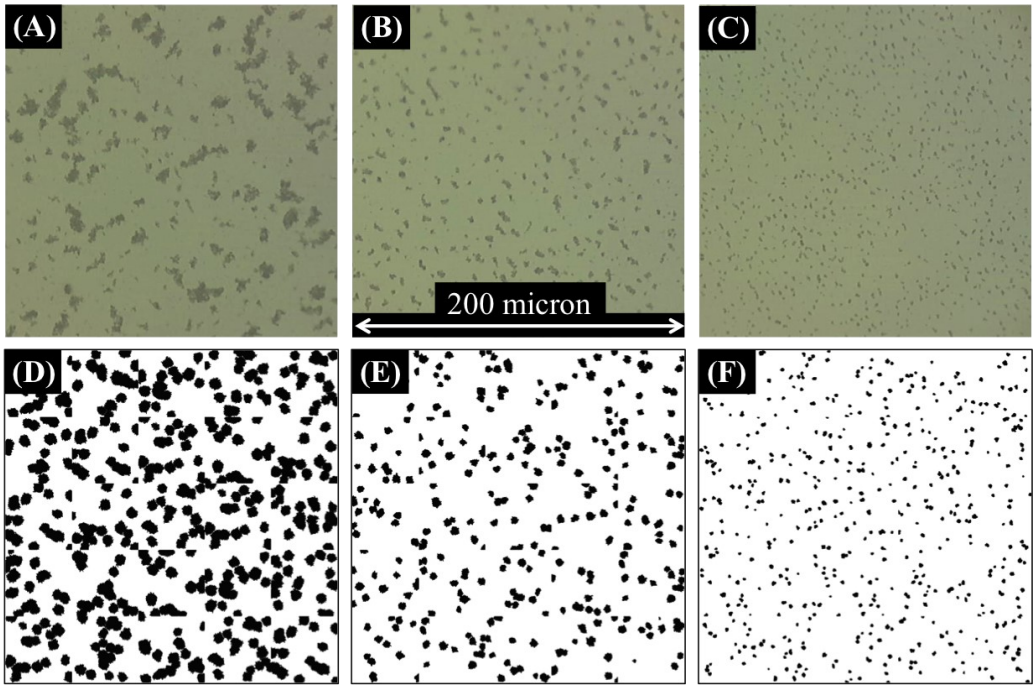

Figure 23 - Microscopy images at 100x magnification of spin-coated films with average thicknesses of (A) 6-μm, (B) 4-μm, and (C) 2-μm; (D-F) Simulated film RVEs of matching thickness and cross-sectional area to their experimental counterparts above

Dispersion energy applied via ultrasonic homogenization was varied between 0-kJ and 25-kJ. Five CPC film samples were generated at each dispersion increment while maintaining mixture constituent concentrations. Figure 24 shows microscopy images from two separately prepared mixtures with applied dispersion energies of (Figure 24ACD) 2-kJ and (Figure 24BEF) 17-kJ, acquired at two magnifications. Comparing Figure 24A and Figure 24B, one can confidently make a qualitative characterization of the differing dispersion states - Figure 24A is poorly dispersed, and Figure 24B is very well dispersed. Closer inspection of the same samples at greater magnification (i.e. Figure 24C and E) reveal dispersion states that are more difficult to tell apart.

A moderately large agglomerate feature in Figure 24A is magnified in Figure 24D. Numerical determination of the exact boundaries of such agglomerates captured at 100x

magnification proved difficult. Contrasting algorithms were deployed to improve the particle analysis macro's ability to capture all visible agglomerates. The success of those algorithms was determined by manual comparison of visible agglomerates counted in grayscale microscopy images (Figure 24E) to their binary transformations (Figure 24F). Often, those same contrasting algorithms were unsuccessful when deployed on images of less-dispersed regions (Figure 24D). In such cases, visible agglomerates were omitted and/or boundary noise was generated due to inconsistent edge contrasting, a product of imperfectly leveled samples and shadowing/blurring during imaging. For this reason, agglomerates found to be contacting image boundaries were excluded from statistical analysis.

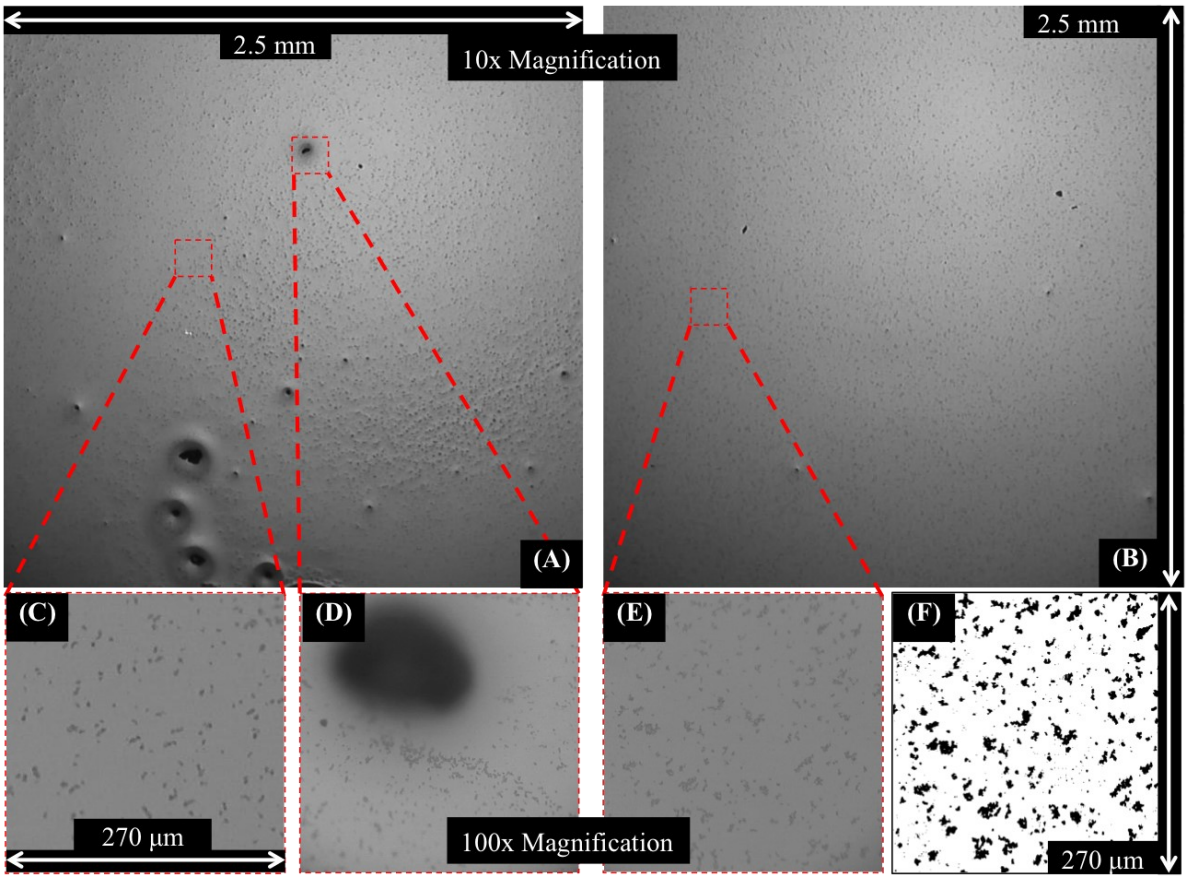

Figure 24 - Microscopy of two separately prepared nanocomposite film samples at varying magnifications. (ACD) Sample probed with 2-kJ of energy, imaged at (A) 10x magnification and (CD) 100x magnification. (BEF) Sample probed with 17-kJ of energy, imaged at (B) 10x magnification and (E) 100x magnification (F) post-processed using ImageJ

Statistics from images acquired at 100x magnification revealed similar particle area and perimeter distributions for samples across the entire range of dispersion energies. The vast majority of recorded agglomerate areas from those images ranged from 1 to 50-μm^2. At 10x magnification, agglomerates of a similar order of magnitude in area were difficult to distinguish from background noise as shown in Figure 25B - a close-up image of a well-defined agglomerate from Figure 25A. Surrounding this agglomerate, one can identify collections of slightly darkened pixels, ranging from areas of 1 to 4-$pixels^2$, or 13.5 to 216-μm^2 considering the scale of the image. With knowledge of the range of agglomerate areas defined at higher magnification, one could reasonably assume that these dark collections of pixels are in fact CB agglomerates. Programmatic boundary definition for agglomerates of such size introduces a greater probability of noise (due to image digitization); therefore agglomerates with areas under a minimum area threshold were filtered from the datasets. Statistical analysis was performed while varying the applied minimum area threshold to observe the effects of such data filtering, and those results are shown in Figure 25C-D. Approximately 250 images were acquired from each sample at 100x magnification, which amounts to a cumulative imaged area of approximately 20-μm^2 per sample. At 10x magnification, 40 images were acquired from each sample, a cumulative imaged area of approximately 250-μm^2 per sample. By imaging a larger area at a lower magnification, the largest agglomerates on each sample are typically captured, thus greatly influencing the averages reported in Figure 25C. Consider an image of a poorly mixed sample (Figure 24A) containing large agglomerates. When focusing in on larger agglomerates at 100x, often such agglomerates are so large that the entire image is black. Such images, which would drastically skew the averages of datasets they are included in, are typically thrown out through the exclusion of edge agglomerates. The average agglomerate areas from images acquired at 10x and 100x, with

various area threshold filters applied, are plotted in Figure 25C and Figure 25D respectively. From Figure 25D, no consistent trend between the average agglomerate area and sample probe dispersion energy is observed. Images at 10x magnification revealed drastic differences in dispersion between samples prepared with varied mixing energies applied via the ultrasonic probe. In Figure 25C, the data suggests that the average agglomerate area tends to decrease with increased mixture dispersion energy. Samples prepared with 5-kJ or greater dispersion energy showed consistent average agglomerate areas when applying a constant minimum area threshold. Average agglomerate areas of the datasets filtered with the smallest minimum area threshold, 4-pixels^2 or 55-μm^2, were found to be consistent across all samples. As the minimum area threshold was increased, average agglomerate area of samples prepared with 5-kJ or greater dispersion energy tended to scale similarly, while average areas of less dispersed samples tended to increase much more rapidly. This trend is attributed to the fact that the majority of CB agglomerates have apparent areas that cannot be discerned from background noise at 10x magnification. It is concluded that data from microscopy images acquired at 10x magnification more precisely define the positive tail end of the agglomerate area distribution curve at the macro scale. This tail end of the distribution is where differences in dispersion characteristics are apparent to the naked eye and easily quantified.

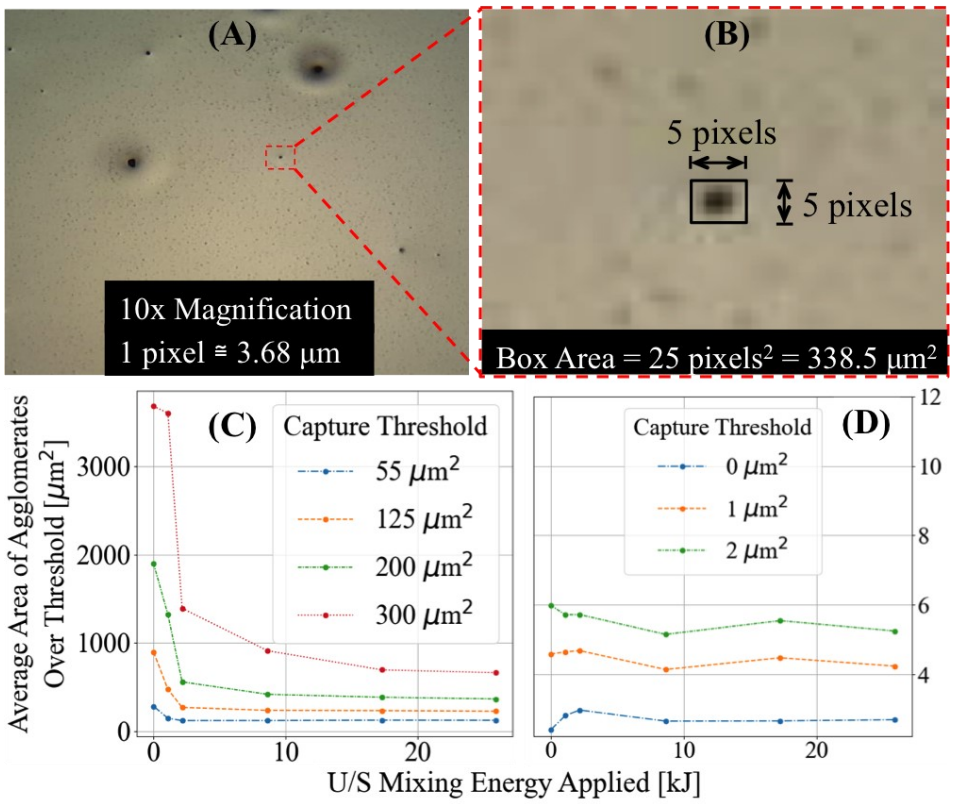

Figure 25 - (A) Moderately mixed (2.16-kJ) nanocomposite film sample imaged at 10x magnification and (B) enlarged to show pixilation of agglomerate features and their approximate dimensions. Plots of average agglomerate areas of samples with varied dispersion energy at (C) 10x and (D) 100x magnification with varying area threshold filters applied

Simulating RVEs with dispersion characteristics comparable to those seen in Figure 24A presents a unique challenge that the current stochastic simulation tool is not suited to efficiently address. In such poorly dispersed samples, the concentration of CB in large agglomerates greatly skews the relative densities and weight fractions of CB at various locations about the film. Such large agglomerates cannot be replicated using the current simulation configuration, however the current simulation configuration can be used to accurately represent well-dispersed CB nanocomposite films such as the example shown in Figure 24B. Thousands of RVEs, of comparable thicknesses to experimental film samples, were generated while varying simulation placement algorithm parameters. Statistical analysis was performed on the resulting RVE film

images and compared to statistics from experimental images of samples prepared with ultrasonic dispersion energies greater than 15-kJ imaged at 100x magnification. Distribution plots of agglomerate area, perimeter, circularity, roundness, solidity, and aspect ratio (AR) for experimental film samples imaged at 100x magnification (solid lines) and comparable simulated film RVEs (dashed/dotted lines) are shown in Figure 26. These image statistics are directly reported from the ImageJ particle analysis macro, and technical formulations can be located via official online ImageJ documentation [133]. Figure 26 demonstrates the capability of the model to generate a large range of agglomerated fractal aggregate structures. Variations in the geometries of such agglomerates can be quantified using commonly deployed image analysis methods, and user defined model parameters can be tuned to replicate geometries and shape descriptor statistics observed in experimental samples. The number of possible placement parameter and FracVal aggregate generation parameter combinations is vast, and precise tuning of these simulation variables is beyond the scope of this dissertation.

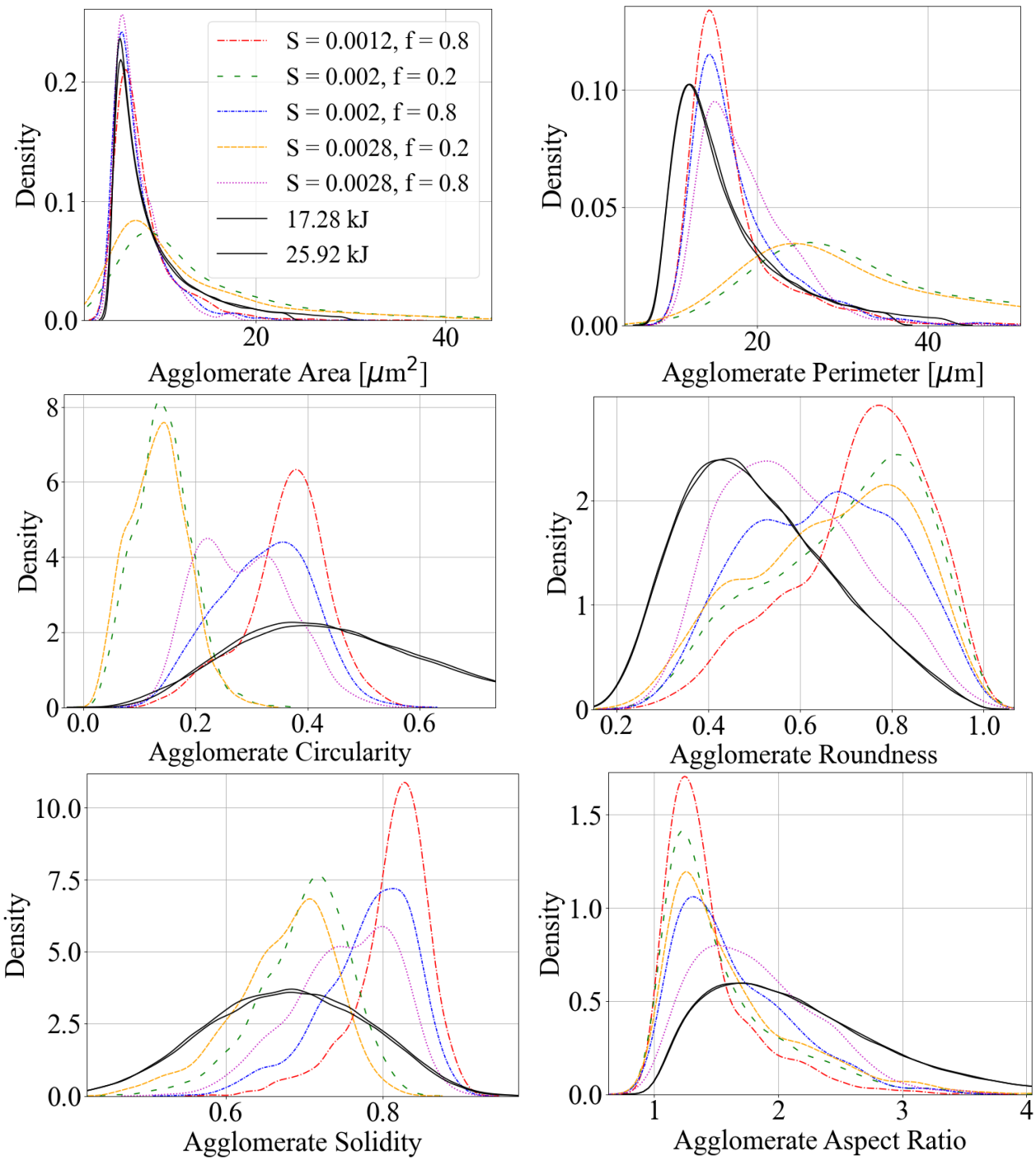

Figure 26 – Kernel density estimate plots of various shape descriptor statistics from ImageJ particle analysis of collections of microscopy images (solid lines) of well dispersed samples imaged at 100x magnification and collections of simulated film RVEs (dashed/dotted lines) with varying stochastic model agglomerate placement parameters.

3.4. Chapter summary

In this Chapter, the experimental methods for validating the fidelity of the final iteration of the stochastic modeling program were presented. CPC samples consisting of a two-part epoxy system and specialty conductive CB, prepared via ultrasonic homogenization and calendaring using a 3-roll mill, were investigated for determining the influence of preparation parameters on resulting dispersion characteristics of cured samples.

The CB variety (Vulcan © XC Max 22) used in this study was characterized via TEM to validate the manufacturer's specifications of average particle diameter (approximately 30-nm), and the resulting measured diameters were found in agreement. Dispersion characteristics of cured CPC mixtures sandwiched between glass microscopy slides were investigated via optical microscopy. Initial investigation of sandwiched mixtures revealed CB smearing and agglomerations that were vastly different than simulated volumes.

Comparing simulated volumes to experimental samples requires knowledge of the experimental sample dimensions for defining comparable simulation parameters. Estimation of the thicknesses of the sandwiched films was attempted unsuccessfully by freeze-fracturing samples and observing fractured cross-sections via optical microscopy. Surface profilometry was pursued as an alternative thickness measurement system. A quick release film was inserted into the microscopy slide sandwich samples to facilitate the removal and exposure of the cured CPC films. Cured samples were sent to Filmetrics for examination via optical profilometry. Resulting film measurements concluded that the thickness of the films produced via the sandwich method varied from 0.1 to 5 micron. Profilometry was identified as a preferred measurement approach, and coincidentally a stylus profilometer in a collaborator's lab was discovered and repaired.

To produce CPC films with more consistent topographies, a spin coater was created using a spare HDD and 3D printed parts. Initial microscopy images of spin coated samples revealed clearly defined agglomerates of sizes that were replicable via preliminary simulation attempts. CPC film sample substrates were adapted to improve the repeatability and accuracy of film thickness measurement using the stylus profilometer. The inherent error of the new measurement system was quantified as less than 10%. Pooling of the CPC mixture on the substrates was realized in the first spin coating attempts. To combat this phenomenon, plasma cleaning was performed on the substrates and a photopolymer resin was incorporated into the spun mixtures to reduce film mobility during curing using high intensity UV-light.

The relationship between film thickness and optical dispersion characteristics were qualitatively assessed. Trends in agglomerate growth, realized in increasingly thicker experimental samples, was replicated using the final iteration of the stochastic modeling program. The effects of varied mixture homogenization energies on the dispersion characteristics of resulting CPC films were investigated. Microscopy images of poorly dispersed and very well dispersed samples, taken at high magnifications (100x), revealed exceedingly similar agglomerate distributions, while microscopy imaging at lower magnifications (10x) revealed drastic differences in agglomeration. Filtering data to remove noise, differences in average agglomerate area between samples of varied mixture energies were quantified.

For increasingly mixed samples, the average agglomerate area reported from image analysis data appeared to converge. These observations support the theoretical and numerical predictions of aggregate dispersion limits reported by Asylbekov *et al* [99]. Simulated RVEs with comparable dimension and constituent concentrations were generated for comparison to imaged films. Statistical analysis of simulated images was performed via the ImageJ Particle

Analysis algorithm, recording shape descriptor statistics and agglomerate area distributions. Preliminary investigation of model tuning was conducted by comparing image statistics, calculated using ImageJ, of experimental samples image statistics of rendered RVEs while varying simulation parameters. The evidence of the ability of the final iteration of the stochastic modeling program to encompass a wide range of possible agglomeration characteristics was presented. Future works regarding model parameter tuning should focus on the application of multivariate nonlinear regression methods, such as those commonly deployed in the machine learning discipline.

CHAPTER 4

EXPERIMENTAL CHARACTERIZATION OF ELECTROMECHANICAL PROPERTIES OF BULK CPCS

4.1. Development of sample manufacturing/characterization methods

The efficacy of deploying a CPC transducer network for SHM applications has been frequently discussed in the literature, as detailed in Chapter 1. Two major research pathways associated with the development of such systems are focused on (i) the mass manufacturability, reproducibility, incorporation, and maintenance of such systems in structural designs and (ii) the development of models to understand the variation in CPC transducer electromechanical properties during service life - relating transducer output to quantifiable degradation of structural integrity. Both research pathways are highly interdependent. Pursuing research focused on addressing the first pathway (i) is greatly enticing with a wealth of intellectual property rights and commercialization opportunities looming. The second pathway (ii), while equally critical for the advancement of such technologies, has received less attention in the literature.

In Chapter 2, a stochastic modeling program was developed for purposes of studying the electromechanical properties of CB-based CPC materials. Experimental results in Chapter 3

garnered confidence in the ability of the model to accurately represent physical CPC specimens through optical microscopy based model parameter tuning methods. In this Chapter, the stochastic model program predictions of CPC electromechanical properties are compared directly to the physical CPC specimens of whom they are modeled. The development of a highly repeatable experimental bulk property characterization method is introduced. Additional model parameter tuning necessities are studied through the investigation of the piezoresistive response of the experimental CPC samples.

4.1.1. Injection molding

The CPC mixtures for the bulk electromechanical characterization experiments were prepared using the same methods detailed in Section 3.1. Early experimental efforts were focused on creating a simple proof-of-concept method for realizing conductive samples with resistances measurable via a hand-held digital multi-meter (DMM) with a maximum resistance measuring capability of 40 MΩ. A CPC mixture consisting of 5% by weight CB was poured into layered Kapton tape slot molds of various lengths, widths, and heights. After pouring the CPC, a razor blade was used to scrape off excess material from the slot mold. To facilitate the removal of the samples post-curing, a layer of quick release film was taped to the block. After the sample had cured, conductive silver epoxy (MG Chemicals) was applied to the ends of the transducer to attach braided copper wire lead-outs for electrical interrogation. The inconsistency in transducer geometry produced via this method was undesirable, and alternative means of transducer fabrication were pursued.

An injection molding process was developed to replace the Kapton tape slot molds. Laser cutting nylon sheet materials of varying thickness, transducer slots sheets were created. Additional nylon spacer sheets were laser cut to create injection ports for the mold, shown in

Figure 27. CPC mixtures of varying weight percentage CB were pulled into large syringes and injected into the clamped injection mold. The samples were cured for 24 hours, carefully removed from the mold, and trimmed to precise dimensions that are measured with a digital caliper and recorded for reference during data manipulation. The surface of the sensor was abrasively removed to expose embedded carbon black particles beneath the outermost layer of epoxy insuring an electrical contact was created. Highly conductive silver paste epoxy was applied to abrasively exposed surfaces of the transducer, and 26 AWG wire was adhered to the exposed surfaces. The paste was cured at room temperature before further manipulation and experimentation. The resulting transducers (shown in Figure 27C) were interrogated electrically using a DMM.

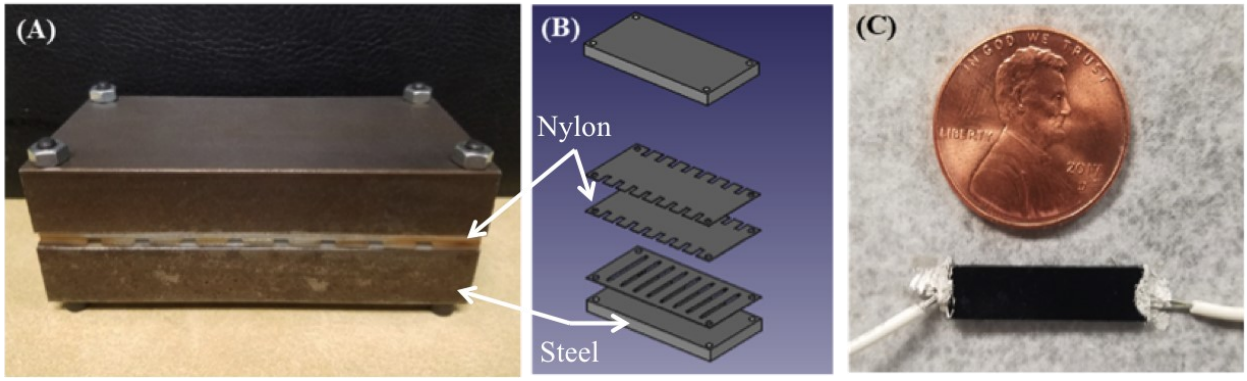

Figure 27 - (A) Image of the fabricated injection mold in its assembled form; (B) Exploded view of the mold assembly; and (C) Sensor sample created via injection molding including electrodes adhered to end faces of cut sample with conductive silver paste.

The measured resistance of the samples varied greatly while agitating the silver pasted electrodes during handling. Inconsistency in the contact resistance of the measurement proved to be insurmountable. As an alternative, copper solder wicking was tested as an embedded electrode. Strips of copper wicking material were taped in parallel inside the injection mold stack between the slot mold sheets and the spacer sheets. The injection mold stack was then carefully

tightened to ensure the wicking materials stayed in place, and the mixture was injected into the mold. The wicking material has a mesh structure that is easily penetrated by the CPC mixture, and was successfully embedded in cured CPC samples. The wicking material provided a much more consistent and repeatable means of interrogating internal conductive networks within the CPC. However, introducing the copper wicking material into the injection mold stack created problems during the injection process. The injected mixtures tended to flow over the copper wicking between the individual slots, creating transducers with less consistent geometries.

The injection molding method produced conductive CPC sensors, measured via DMM, at a weight fraction of approximately 3.25% by weight carbon black. However, the variation in the geometries of the sensors and the variable gauge lengths between copper electrodes produced large measurement errors. Ultimately, the injection molding method was abandoned in pursuit of a more consistent manufacturing method following a technique demonstrated in the literature – spray layer-by-layer (SLBL) manufacturing.

4.1.2. Spray layer-by-layer

A SLBL apparatus was constructed for this study with aims of improving reproducibility and consistency of the CPC samples. The airbrush used in this study (Paasche H-Series) was a single action airbrush that externally mixes forced air with reservoir-drawn mixtures. The movement of the airbrush over the sample substrates was motorized and the control of airbrush actuation mechanisms was assigned to a microcontroller (Arduino). Figure 28 is a schematic of the forced air deposition apparatus. The airbrush was contained in an airtight enclosure that was negatively pressurized via a fan and filtration exhaust system. The airbrush was mounted to a linear actuator, controlled via a microcontroller that commands the airbrush to traverse across

multiple sets of samples at once. An air control manifold, informed by reed switches placed along the linear actuator, was used to initiate airflow through the airbrush.

The linear actuator transverse velocity was characterized to ensure consistent airbrush movement during spray application. The linear actuator operates on either high or low speed settings, with variable speed control via user input from 0V to 5V. The actuator was found to operate smoothly at voltages between 0.5V to 2.5V. For greater layer thickness control, a constant velocity at the high-speed setting was chosen: 2 inches per second at 0.75V.

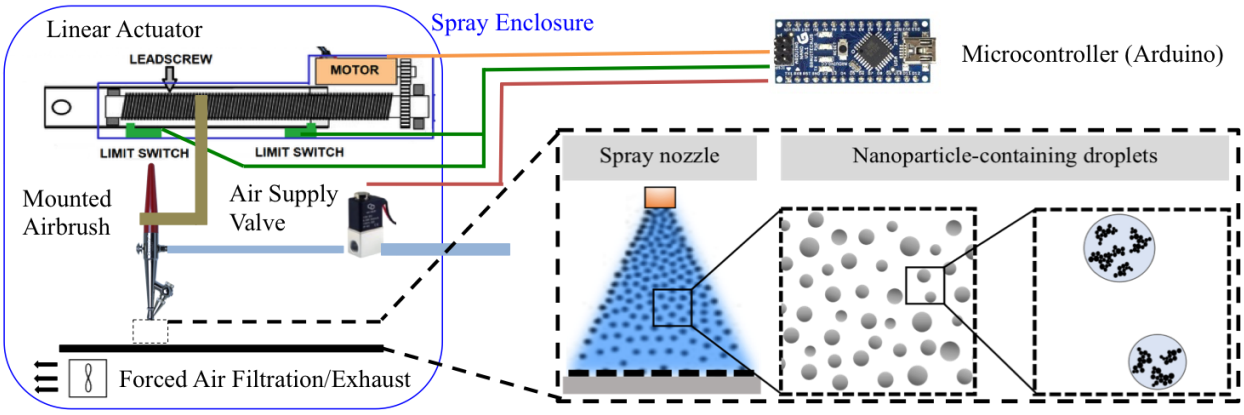

Figure 28 – Schematic of the sLBL apparatus consisting of a lead-screw linear actuator mounted on a forced-air filtered spray enclosure, a hobbyist airbrush controlled by an electric air supply valve, and an Arduino nano commanding the system.

Once the actuator and airbrush transverse velocity control was understood, the airbrush spray control parameters were systematically investigated. Control mechanisms of the airbrush that influence droplet deposition characteristics include the viscosity of the liquid to be sprayed, the input air pressure, and the needle/nozzle depth ratio. For this study, the needle/nozzle depth ratio was held constant at the factory configuration. In addition to actuation and airbrush control parameters, variation in the preparation of the mixture greatly influenced the resulting films. CPC mixtures with 3.15% CB by weight were prepared for this study by following the same batch mixture preparation methods outlined in Section 3.1. Quantities of the master batch were

diluted with acetone in various amounts to reduce the viscosity of the mixtures. Various thinned mixture concentrations were then qualitatively compared to commercial airbrush paints. It was found that by adding approximately 30% by weight acetone to the mixture, a viscosity and consistency similar to that of commercial paints could be achieved. To study the effect of airbrush input pressure variation on the resulting droplet patterns, CPC mixtures were deposited on laboratory grade microscopy slides and cover slips. A single spray pass was performed on a batch of 5 samples for each airbrush input pressure tested. The samples were then left to cure undisturbed in the spray enclosure. After curing for 24 hours, the droplet patterns of each sample were imaged via optical microscopy.

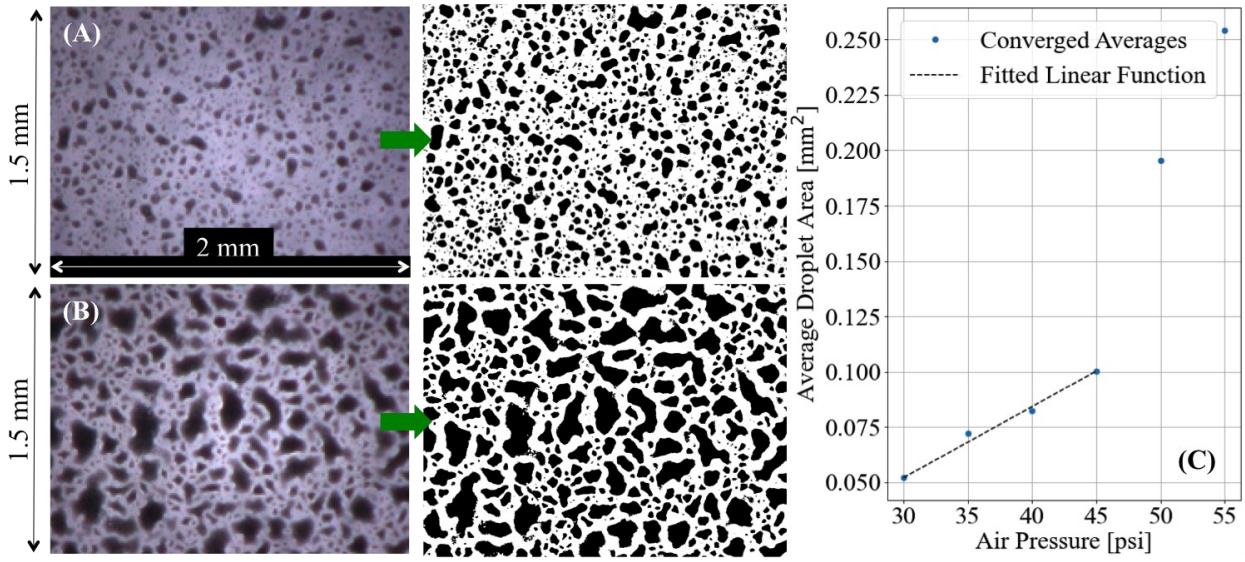

Figure 29 - Microscopy images of single spray pass deposition of CPC droplets on cover slips with Image J post-processing droplet analysis of (A) 25-psi and (B) 50-psi air pressures; (C) Average droplet area as a function of airbrush input air pressure.

Evident in the microscopy images Figure 29A and B, there is a general trend of increasing average droplet size with respect to an increase in airbrush input air pressure. To gain a more comprehensive understanding of this relationship, multiple samples were deposited while varying airbrush input pressures. Microscopy images from each sample were acquired at 10x

magnification, and the average droplet areas of the images were calculated using ImageJ [133] and are plotted in Figure 29C. At lower input air pressures (30 psi to 45 psi) the relationship between pressure and average droplet size appears to be linear. However, pressures above 45 psi produced erratic results. For this reason, the PCB sensors were manufactured with an input air pressure of 35 psi.

As previously mentioned, the issues of measurement error inherent in the injection mold method proved troublesome for determining accurate conductivity estimates for the resulting CPC samples. For this reason, a PCB substrate was identified as a candidate substrate upon which CPC could be deposited via SLBL manufacturing. The PCB samples, shown in Figure 30F and G, were manufactured (PCBway.com) for the purpose of creating easily interrogated transducers with precise geometries and electrode spacing/conditions. The methodology for creating the finished sensor substrates shown in Figure 30G is represented in Figure 30A-E. Kapton tape is adhered to the surface of the PCBs to serve as a masking layer. Rectangular slots are cut out of the Katpon tape layer with a C02 laser. The SLBL CPC mixture deposition method, described in the following section, is then used to create a piezoresistive film atop the opposing copper pads. Copper traces connect these electrode pads to through-hole vias to provide easy-to-access solder and probe locations used for resistance measurements.

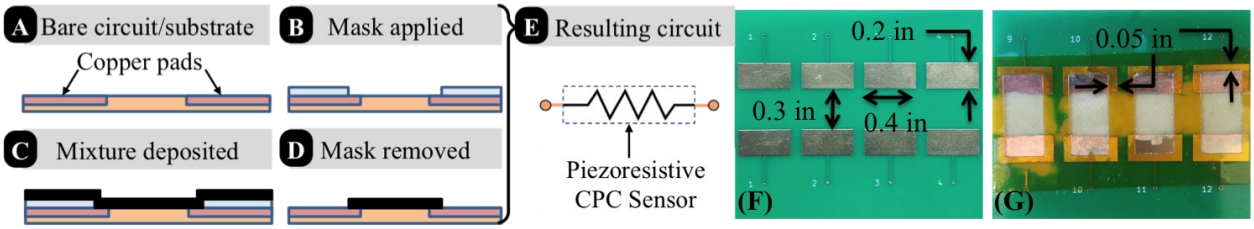

Figure 30 – (A-E) Schematic representation of the creation of PCB sample substrates; (F) PCB without solder mask and (G) after abrasive preparation with Kapton solder mask applied

As evident in Figure 29A and B, the CPC mixtures had a tendency to form droplets on the glass substrates. The wettability of the PCB solder mask layer proved similar to that of the glass microscopy slides, and thus additional sample surface preparation was required. Surface preparation was accomplished using various sanding and buffing compounds applied via various mechanical methods including a drill equipped with a buffing wheel, a rotary tool sander, and a hand-sanding block. CPC films were deposited on PCB samples whose surfaces were abrasively prepared by various methods. CPC mixtures at 30% by weight acetone thinner were sprayed at an air pressure of 30 psi for 10 passes over the PCBs with an actuator speed of 2 inches/second. The results of those films are shown in Figure 31. The untreated sample in Figure 31A clearly shows the pooling of the mixture along the edges where Kapton tape was adhered. Figure 31B-F shows the resulting surface coverage of the films with varying methods of surface preparation. In general, it was found that the removal of the solder mask layer lead to improved film coverage. This is believed to be a result of the hydrophobicity of the solder mask compared to the PCB fiberglass substrate layer. As a result of this finding, the current method of preparation of the PCB substrates equates to the removal of the solder mask layer via abrasive means. The most efficient means of removing the solder mask layer was found to utilize a rotary hand-tool (Dremel) equipped with 220-grit sandpaper.

The resulting film of Figure 31F is ideal due to the fact that the film covers the entire slotted region of the substrate. This coverage was found to be qualitatively smooth, and initial observations via stylus profilometry show the ability to produce films with thicknesses on the order of microns. Furthermore, initial investigations of increased thinner content samples showed an even greater potential to produce sub-micron film depositions. While the PCB deposited film of Figure 31F is smooth and visibly consistent, the film conductivity was difficult to assess. This

is largely due to the lack of adhesion between the CPC film and copper electrodes. As opposed to the woven copper wick, the PCB copper electrodes offer little to no voids for surface penetration by the mixture. As a result, the films were easily peeled from the PCB surfaces, and recorded conductivity measurements were greatly influenced by lightly handling the samples. In addition to this complication, the necessary abrasive removal of the solder mask layer increased the error in measuring the geometry of the deposited films. These realizations raised concerns about the potential for using traditional PCBs for such characterization methods.

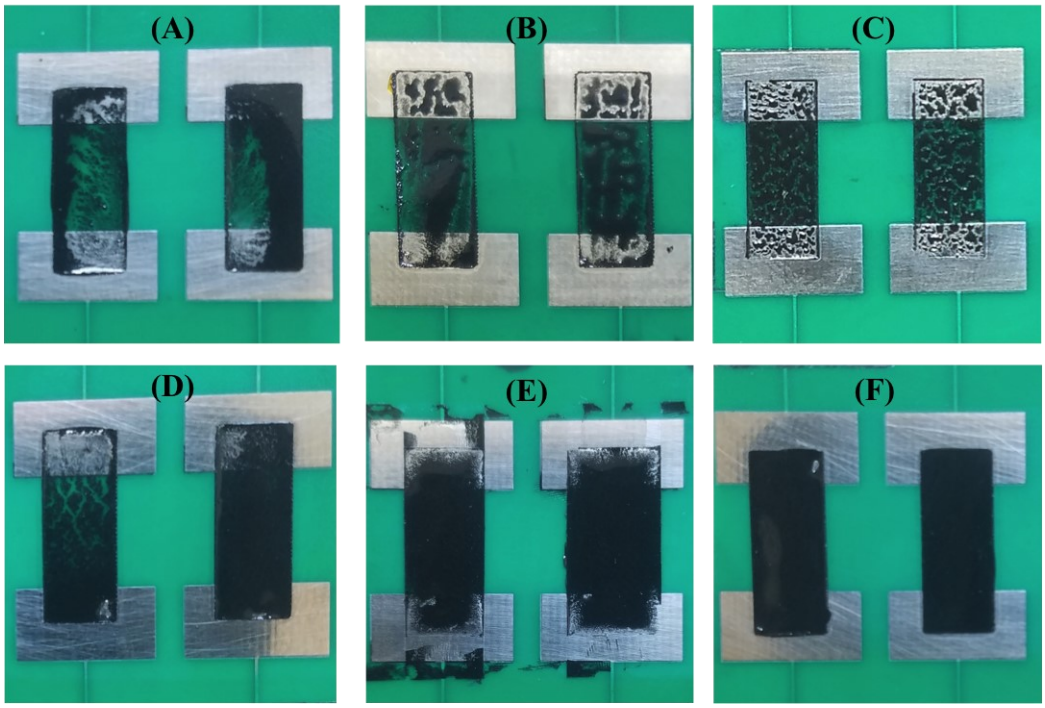

Figure 31 - CPC films deposited on PCBs with various surface preparations: (A) Untreated, (B) Light sisal wheel buffing, (C) Sisal wheel buffing (light), (D) Denim wheel buffing (light), (E) Denim wheel buffing (heavy), (F) 220 grit sandpaper.

A simple and cost effective alternative was pursued to replace the PCB substrates. Depositing CPC via SLBL on standard printer paper, no droplet formation or pooling was observed. To create rectangular film geometries, rectangular slots were cut out of thicker construction paper sheets that were used as a spray stencil. Taping carbon fiber (CF) tows (3k,

ACP Composites) in parallel on the printer paper substrate to be coated/embedded via SLBL, the electrical properties of the CPC films could easily and consistently be interrogated. An image of a resulting paper substrate CPC transducer is shown in Figure 32B. Spraying additional layers the thickness of the deposited CPC film can be increased. The relationship between the total passes of the airbrush and the resulting sensor thicknesses are shown in Figure 32A. Measurements acquired via digital micrometer (Mituyo) are reduced by the average thickness of standard printer paper (~ 0.1-mm) to determine the thickness of the CPC film alone. While it is assumed that the CPC is partially absorbed by the paper fibers, this measurement allows for a simplified approximation of CPC electromechanical properties.

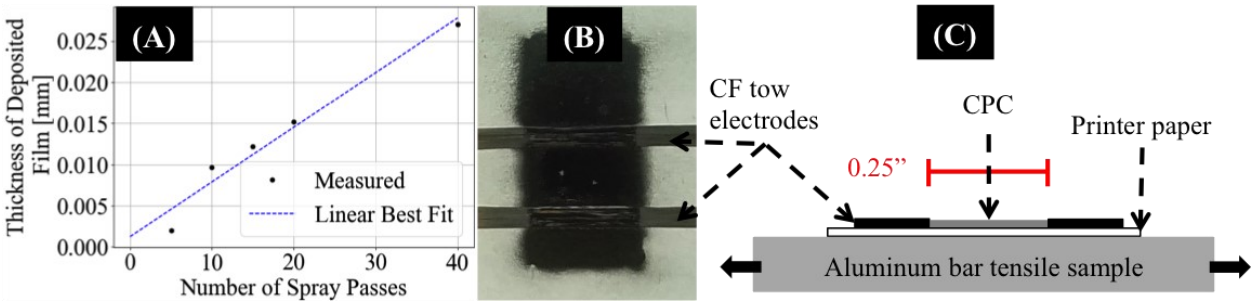

Figure 32 – (A) Relationship between paper substrate CPC transducer thickness and the number of layers applied via additional spray passes; (B) An image of a paper substrate CPC transducer after curing; (C) Illustration of the adhesion of a finished paper substrate CPC transducer to an aluminum tensile sample for piezoresistivity characterization

The piezoresistive characteristics of the paper substrate CPC transducers were characterized by adhering the transducers to aluminum bars for uniaxial tensile strain application via a hydraulic load frame (MTS). Figure 32C illustrates that the sample is oriented such that the strain field is parallel with the direction of the voltage differential applied across the CF tow electrodes. To measure the change in sample resistance during strain deformation, the CF electrodes were mechanically connected to lead-wires using metallic alligator clips. A CompactDAQ (cDAQ), paired with LabView (National Instruments), was used to record

measurements of sample resistance during testing. The cDAQ was equipped with a strain/bridge input module (NI-9237) and a RJ-50 to screw-terminal connector (NI 9949) to streamline the data acquisition process. Connecting the transducer in a quarter-bridge configuration required a precision resistor to be supplied to match the nominal resistance of the transducer. The paper substrate CPC transducer nominal resistances ranged from 1-MΩ to 8 MΩ. To cover this range of resistances, multiple high-resistance potentiometers were soldered together in series on a prototype breadboard, and were subsequently connected to the bridge module. By connecting potentiometers to the bridge, the bridge could be balanced without the need for programmatic compensation. Once the bridge was balanced successfully, the piezoresistivity of the sample could be examined.

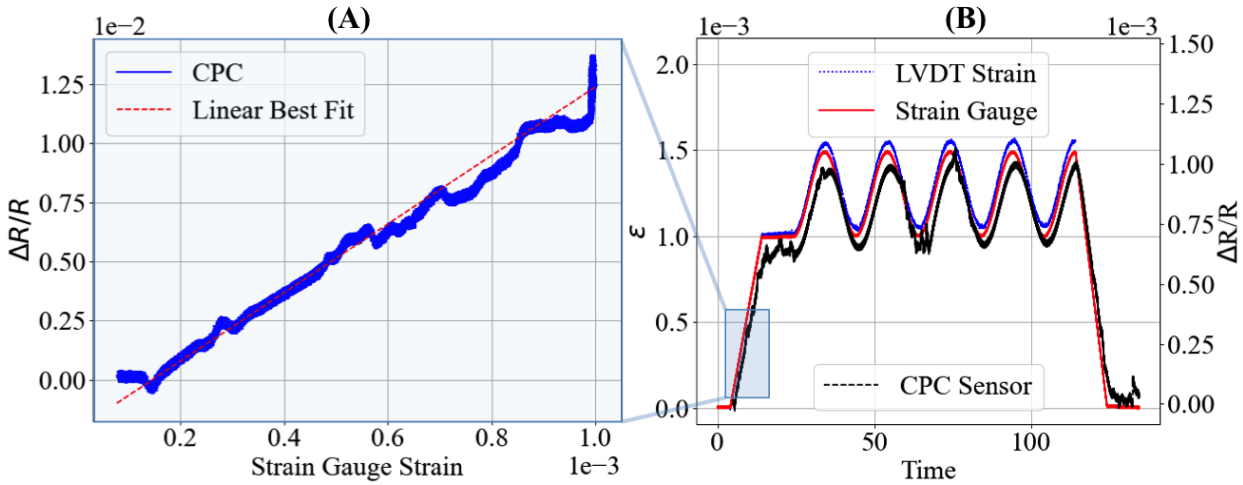

Figure 33 – (A) Characterization of the relationship between applied strain, measured by a traditional strain gauge, and the relative change in resistance of the CPC transducer during a linear strain increase during uniaxial testing; (B) Time-series data of strain calculated via the load frame's linear variable displacement transducer (LVDT) output, strain as measured by a foil strain gauge adhered to the beam, and un-scaled strain measured by the CPC transducer during a uniaxial cyclic tensile test

Figure 33 shows plots of data acquired from multiple measurement sources during a single uniaxial tensile test of an aluminum beam equipped with a CPC transducer similar to the schematic shown in Figure 32C. The aluminum beam (1" wide, 0.125" thick, 8" long) was also

equipped with a traditional foil strain gauge (Omega) for comparison and validation of the strain calculated using the linear variable displacement transducer (LVDT) data output by the load frame controller. The data from the load frame (force and displacement) was also collected by the cDAQ to maintain a coincident time-series between the LVDT, strain gauge, and CPC data. This time-series data is plotted in Figure 33B. The load frame was commanded by a force-controlled feedback loop, informed by a load cell, using a proprietary software suite (MTS TestSuite). The test begins with a ramped increase in applied strain, followed by a cyclic variation in strain, finishing with a ramped relaxation to the zero load state.

The CPC transducer signature shown in Figure 33B is a measure of relative resistance change. For common foil strain gauges, the following formulation is used to calculate strain

$$\epsilon * K = \frac{\Delta R}{R} \qquad \text{Equation 4-1}$$

where ϵ is the strain in the direction defined by the sensor's orientation, K is the gauge factor, and $\Delta R/R$ is the relative change of resistance of the strain gauge. Typically, the gauge factor is a unit-less constant provided by the manufacturer. For this reason, the gauge factor of the sensor is requested in the LabView subroutine for the strain/bridge module to scale the output of the balanced bridge to a strain value.

Having no knowledge of the effective gauge factor of the CPC transducers, an arbitrary gage factor of 1.0 was defined in the LabView subroutine. The measurements recorded from the bridge are therefore a direct observation of the relative change of resistance of the CPC at various levels of strain. Observing the plot of Figure 33A, it is shown that a linear function can be defined in agreement with the plotted data of relative change of resistance of the CPC at various applied strains. This proportional relationship is consistent with the definition for gauge

factor in Equation 4-1. Thus the slope of the fitted line is assumed to be equal to the gauge factor, which was estimated at 14.5.

The results of experiments with paper substrate CPC transducers successfully demonstrated the piezoresistivity of CPC samples containing 3.15% by weight CB. However, the absorption of the CPC mixtures by the paper substrate introduced additional uncertainties. These uncertainties include the influence of the paper fibers on the formation of conductive networks and the effective geometry of the CPC transducer. Once again, an alternative approach was investigated to reduce uncertainty in the comparison of stochastic and experimental results.

4.1.3. Casting

Casting was identified as a cost effective, simple, and repeatable manufacturing method for molding room-temperature curable CPC transducers. To create flexible casting molds, a room-temperature cure two-part silicone epoxy was poured into 3D printed molds. An image of the 3D printed inverse dogbone-shaped mold is shown in Figure 34A. This 3D printed structure is used to create the silicone dogbone-shaped molds shown in Figure 34B and C, which are then used to cast dogbone-shaped CPC samples such as the sample shown in Figure 34D. The shape of the sample was designed in accordance with the ASTM D638-14 standard [138]. Slots were created in the silicon mold to allow the placement of CF tows in precise locations about the sample gauge length. 3k CF tows were placed in the slots prior to the deposition of the CPC to limit the flow of the CPC into the ends/tabs of the mold. The sample tabs were poured with neat resin to eliminate the influence of conductive pathway formation via the metallic grips of the hydraulic load frame.

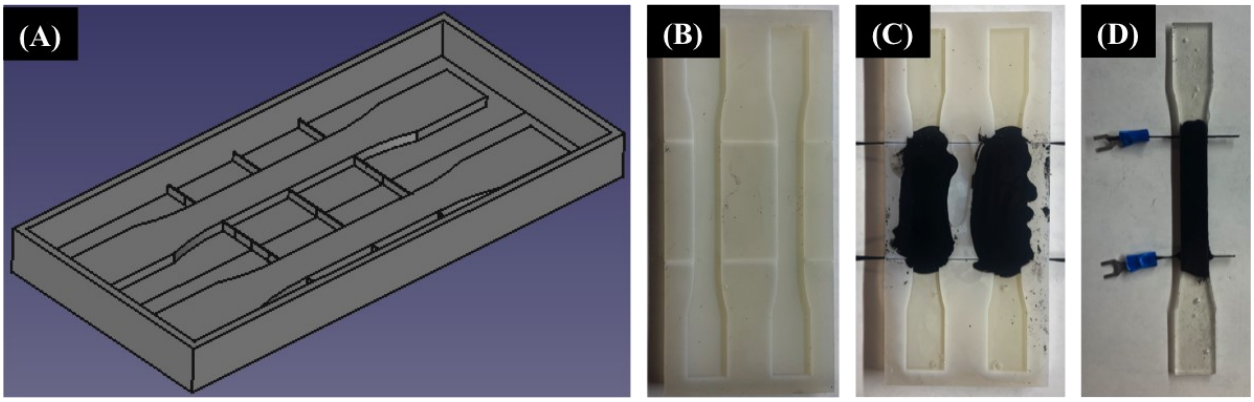

Figure 34 – (A) Rendering of 3D printed dogbone mold maker; (B) Cured silicon epoxy dogbone mold; (C) Dogbone mold with CPC transducer curing; (D) CPC dogbone sample with easy-access clamped electrical leads ready to be tested

Quantities of the master batch detailed in Section 4.1.2 were diluted with ethanol at a concentration of 1 part ethanol to 1 part resin. The thinned mixture was then agitated via ultrasonic probe homogenization at 65% of maximum power at a duty cycle of 40%. After homogenization, the mixture was baked in a conventional oven at 180 degrees Fahrenheit for 72 hours with occasional stirring to evaporate the vast majority of the ethanol. After evaporating the solvent and allowing the mixture to cool to room temperature the hardening agent was incorporated into the final mixture via hand stirring. Finally, the mixture was poured into the casting mold, and excess resin was scraped from the mold using a straight edge tool. The samples were allowed to cure for 24 hours at room temperature. After removal of the samples from the cast, the edges of the sample were trimmed using a razor blade.

4.2. Characterization of cast CPC samples

Measurements of pristine sample geometry and resistance were acquired prior to uniaxial tensile testing. The average length, width, and thickness of the gauge length region of the CPC samples were 56-mm, 13-mm, and 3-mm respectively. Mixtures were produced with ultrasonic homogenization energies 50-kJ, and 100-kJ. These mixtures were spin coated and imaged via

light microscopy to investigate dispersion characteristics. Images from the spin-coated films are shown in Figure 35A and B. The mixture prepared with 100-kJ of homogenization energy was considered to be of the greatest possible dispersion using the probe method. Measurements from cast CPC samples prepared with the 100-kJ mixture were to be compared directly to stochastic model predictions. The average and standard deviation of ten, 100-kJ mixture energy, CPC samples' resistivity at a pristine state was 0.261 Ω-m and 0.085 Ω-m respectively. The average and standard deviation of six, 50-kJ mixture energy, samples' resistivity at a pristine state was 1.940 Ω-m and 0.249 Ω-m respectively.

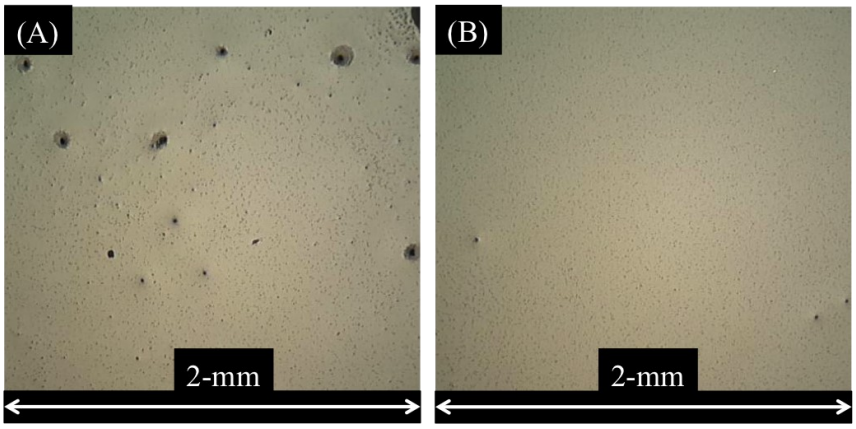

Figure 35 - Images of spin coated CPC film samples with homogenization energies of (A) 50-kJ and (B) 100-kJ

Individual samples were carefully secured in the load frame grips under a no-load condition, and uniaxial strain tests were performed while monitoring the change in sample resistance using the aforementioned quarter-bridge data acquisition setup. In addition to monitoring the CPC electrical properties, the elongation of the sample is measured about the gauge length using an extensometer (Epsilon). Figure 36A shows extensometer and CPC resistance change data for a sample being strained at a constant rate of 0.2-mm per minute. Since the time-series data from the extensometer and CPC sample are coincident, the relative resistance

change can be plotted in relation to the local strain measurement, shown in Figure 36B. At low strains ($\epsilon < 0.004$) the relationship between measured strain and relative change in sample resistance appears to be linear. The relationship between measured stress and strain, and stress and relative resistance change, also appeared to be correlated linearly. The same uniaxial tensile test was performed on each sample, and the results of those tests are tabulated in Appendix A. The slope of the best-fit line relating relative resistance change to strain is equivalent to a sample's gauge factor (GF). The average GF, and standard deviation of the measured GFs, of the 100-kJ samples was slightly less than that of the 50-kJ samples. The most significant difference between the sample mixtures was their average resistivity: 0.26 for 100-kJ, and 1.94 for 50-kJ.

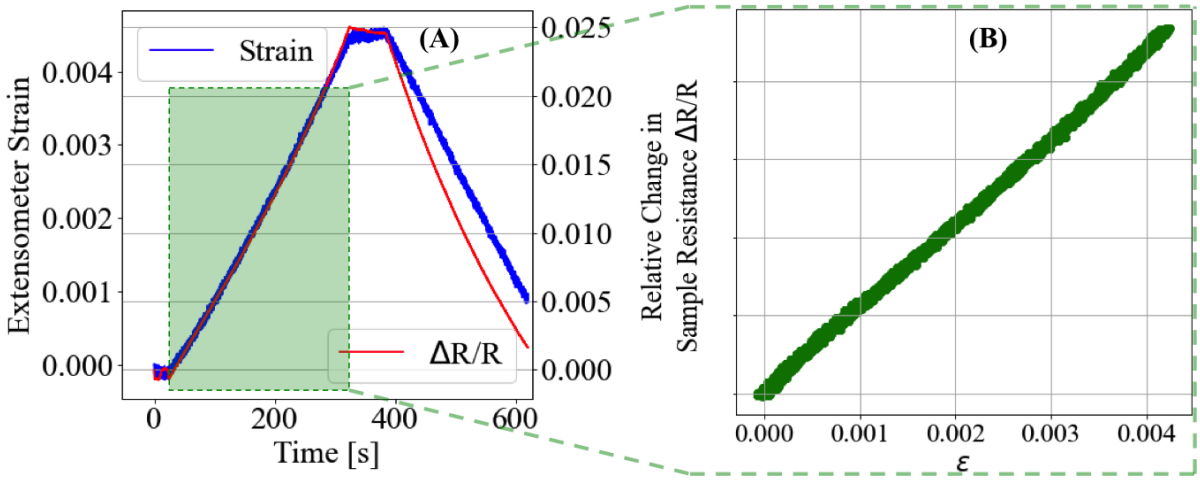

Figure 36 – (A) Plot of extensometer and CPC sample resistance measurements obtained undergoing a uniaxial tensile event with incremental displacement control rate of 0.1-mm per minute; (B) Plot of relative CPC sample resistance change with respect to measured local strain

4.2.1. Comparison of predictive models

Hundreds of stochastic RVEs were generated with the final iteration of the stochastic modeling program detailed in Chapter 2. Simulation parameters for the generation of the RVEs were defined in accordance with the results of the model fidelity validation and tuning research detailed in Chapter 3. RVEs cubic lengths of 12000-nm were subjected to incremental uniaxial strain, and the relative change in RVE resistance at each increment of strain was calculated

following the method discussed in Section 2.2.2. The polymer barrier height simulation parameter (λ) was varied to study the influence of the parameter on the predicted resistance change of the simulated RVEs. Each RVE relative resistance change is calculated for varying values of λ, and the individual data points and averages are plotted in Figure 37A. Evident in Figure 37A, varying the assumed value of λ influences the rate of relative resistance change with respect to strain. In other words, the assumed value for λ directly influences the GF predictions of the stochastic model.

The simulation parameter defining the resistance between particle pairs in direct contact (R_c) was also varied to study its influence on the predictions of conductivity for RVEs at zero strain. After searching the literature and finding no experimentally derived values, an arbitrary value for R_c (1000 Ω) was used in initial simulations. The same RVEs used to generate the data in Figure 37A were used to generate predictions of unstrained resistivity while varying R_c. The results are shown in Figure 37B. As the value of R_c is increased, the average resistivity of the RVEs is increased. The standard deviation of the average resistivity was also found to increase. The average measured resistivity of the experimental samples is plotted in Figure 37B for reference. These results show that by varying λ and R_c within physically feasible bounds the predictions of the electromechanical properties of the modeled CPCs can be tuned to more closely resemble characteristics of physical CPC systems.

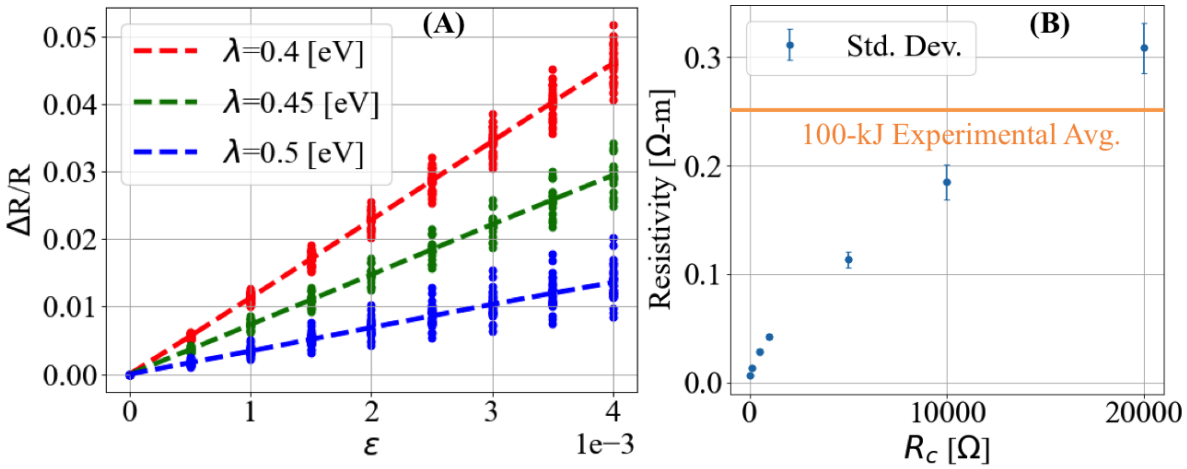

Figure 37 – (A) Plot of average relative resistance change of RVEs subjected to uniaxial strain while varying values of polymer barrier height, a parameter used in calculating tunneling resistance between simulated particle pairs; (B) Plot of nominal resistivity predictions for simulated RVEs considering varying values of contact resistance between particle pairs in direct contact.

Piezoresistivity predictions for the cast CPC samples were computed using the analytical model developed by Zhang *et al.* [118], detailed in Section 1.5.1. The parameters in the analytical model were defined according to the specifications of the cast CPC experimental samples. The analytically predicted response of the CPC is compared to experimental results from a single CPC specimen in Figure 38. As evident from this plot, major disagreement exists between the experimental results and the original model predictions. As discussed in Section 1.5.1, the original derivation of the model assumes the spherical conductive filler in the CPC is arranged in a cubic lattice to simplify the mathematical calculation of the average interparticle tunneling distance (s_0) [118]. The research presented in Chapter 3 proves that this assumption is not appropriate for real mixtures due to their stochastic particle dispersions. Instead, the cubic lattice assumption serves as a theoretical upper bound for such CPC systems with maximally ordered particle distributions of isotropic interparticle spacing s_0. Straying away from the cubic lattice assumption proposed in the original model derivation, predictions of piezoresistivity were generated considering a range of values for the variable s_0. The polymer barrier height variable

for the analytical model was set at 0.5-eV, consistent with ranges reported in the literature for similar polymers. Good agreement between experimental and analytical predictions occurred when s_0 was set to a value between 0.5 and 1.0-nm, as shown in Figure 38. For comparison, the idealized cubic lattice assumption resulted in a value of $s_0 \approx$ 15-nm.

Figure 38 plots the predictions of the stochastic and analytical models alongside the experimental data from low-strain portions of a uniaxial tensile test of a cast CPC sample with electromechanical properties near the average of the sample set. From this plot, it is evident that the stochastic model results exhibit gauge factors comparable to the physical CPC specimens at low strains. These results are derived from the application of widely accepted physics-based models to stochastically generated RVE systems with agglomeration features optically comparable to those observed in experiment. The physical model parameters λ and R_c are varied within physically feasible and published ranges defined in the literature, and agreement is found between both predictions of nominal conductivity and gauge factor. Additionally, the deviation of pristine resistivity and gauge factor observed in experimental samples are comparable to the deviations of the same predicted properties obtained via the stochastic model, graphically illustrated in Figure 37A and B. Such deviations in nominal properties are indicative of the stochasticity of the physical specimens. The stochastic nature of the physical specimens is captured via the stochastic modeling algorithm, and agreement between the model's property predictions and experimental results can be tuned by varying simulation parameters representing physical phenomena that are difficult to measure directly (λ and R_c) but remain within physically feasible limits.

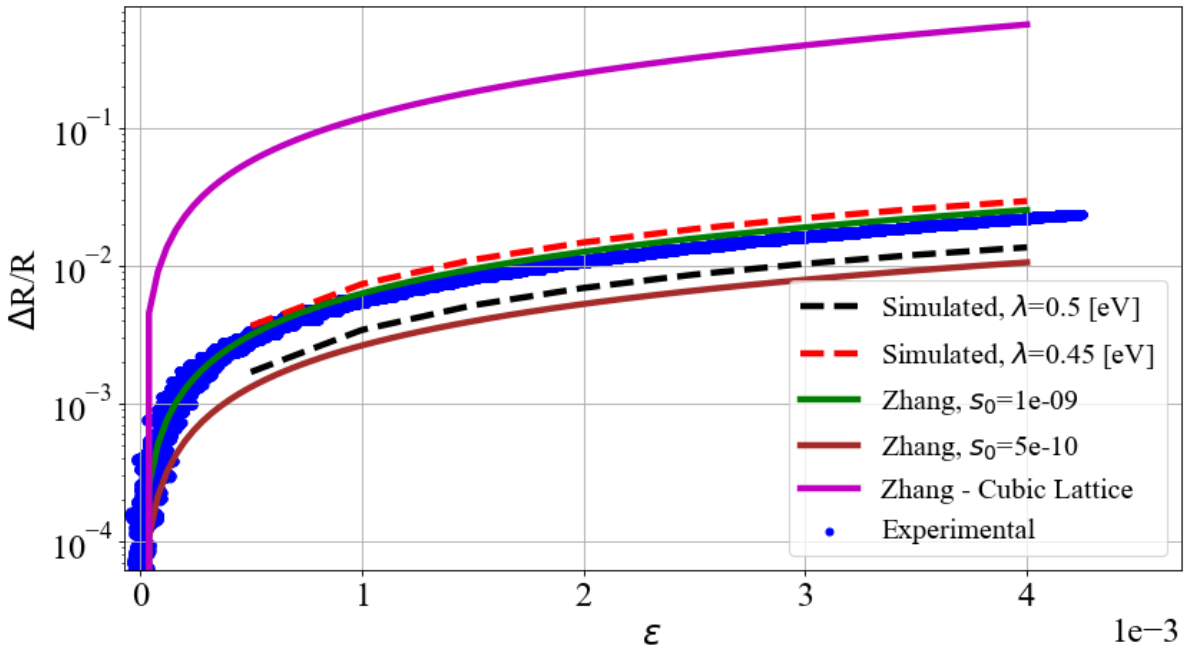

Figure 38 – Plot of relative change of resistance with respect to strain for experimental CPC samples undergoing uniaxial tensile strain events of varying displacement rates, simulated RVEs with varying assumed polymer barrier heights (λ), and analytical predictions from Zhang's piezoresistivity model with varying assumed pristine state average tunneling distances (s_0)

4.3. Chapter Summary

In this Chapter, the development of experimental methods for characterizing the electromechanical properties of CB and phenolic resin CPC materials are presented. The purpose of the development of such methods is to support efforts to improve current models for bettering understanding of the underlying physics behind the experimentally observed behaviors of these materials.

Injection molding was examined as a simple method for manufacturing CPC samples of consistent geometry. CPC mixture consisting of weight concentrations of CB ranging from 0.1% to 5% were mixed via an ultrasonic probe homogenizer before being injected into a custom injection mold composed of steel blocks and nylon sheet slot cavities. After curing, the samples were removed from the mold, and electrodes were created by adhering copper wire to the sample with conductive silver epoxy. The resulting transducers were found to be conductive at CB

weight loadings of approximately 3.5%. The contact resistances of pasted electrodes were sensitive to handling. Embedding copper wicking into the samples during curing was found to create more consistent electrical contacts. However, the incorporation of the copper wicking in the injection mold stack negatively affected the consistency of the sample geometries produced.

PCBs were explored as candidate substrates upon which CPC mixtures could be deposited for creation of CPC transducers. PCB substrates were selected in hopes of improving the consistency of the electrode conditions and creating transducers with precise geometries. SLBL was selected as a method for depositing CPC mixtures onto the substrates. An automated SLBL apparatus was developed for this purpose. Parameters for SLBL apparatus deposition, including airbrush input air pressure, translational speed, and number of passes, were systematically investigated. The solder masks of the PCBs were found to be highly hydrophobic, resulting in pooling of the mixture during curing. By removing the surface solder mask layer, more consistent CPC films were created. The contact resistances between the CPC mixtures and the copper pads upon which the CPCs were deposited were found to be much greater than those estimated from samples with embedded copper wicking electrodes. Additionally, the peel strength of the CPC/pad interface was found to be weak, and sample resistances were found to vary significantly after handling the substrate.

The complications presented by the PCB substrates influenced exploration of alternative substrates upon which CPC transducers could be deposited. Standard printer paper was found to exhibit little to no pooling during SLBL deposition. A linear relationship between the number of spray passes and the resulting thickness of the CPC films deposited on paper substrates was observed. CF tows were taped to paper substrates in parallel to serve as electrodes for CPC electromechanical interrogation. Similar to the copper wicking electrodes, the CF tows were

found to create very consistent electrodes. To create CPC transducers of consistent geometries, rectangular slots were cut out of construction paper to serve as stencils. The resulting transducers were adhered to aluminum tensile specimens and were subjected to uniaxial tensile strain via a hydraulic load frame while monitoring changes in sample resistances. The paper substrate transducers were found to exhibit piezoresistive behaviors for sensors composed of 3.25% by weight CB.

Still, the geometries of transducers were not nearly as precise as desired. To improve CPC transducer geometry, a room-temperature casting method was developed. 3D printed structures were used to create flexible molds out of silicon epoxy. The resulting molds were used to create dogbone-shaped specimens consistent with the specifications of ASTM D638-14. The molds were designed with slots for CF tows to be embedded in parallel about the gauge length of the dogbone-shaped specimens. CPC samples composed of 3.15% by weight CB were cast using the flexible molds, and subjected to uniaxial strain tests. The average relative change of sample resistance with respect to strain for all samples was calculated and compared to predictions of the stochastic model and a popular analytical model from the literature. Modifications to the analytical model are presented, and discussion is offered regarding the motivation to continue development of stochastic models for understanding CPC electromechanical behaviors.

CHAPTER 5

CONCLUDING STATEMENTS

5.1. Master summary

This dissertation discusses numerical, experimental, and analytical aspects of the electromechanical characteristics of composite materials composed of spherical conductive nanoparticles contained within an electrically insulating matrix. The following is a summary of Chapters 2 through 4 that highlights the primary discoveries, successes, and contributions of each Chapter.

5.1.1. Chapter 2

A stochastic modeling program was developed for purposes of studying and predicting the electromechanical properties of CB CPC materials. Multiple programming languages were deployed including Matlab ®, Python, and object-oriented C++. Physical constraints and assumptions applied in the numerical modeling of spherical CB elements are discussed, and fundamental questions of model accuracy and fidelity are presented. Early iterations of the stochastic modeling program (subsequently termed the serial model), developed in Matlab ® and later C++, were designed to utilize a single computing process for the generation of purely

random RVEs and the analysis of random resistor networks contained within. Assessment of the numerical convergence of the serial model was achieved by generating hundreds of stochastic RVEs and examining the moving average of the reported conductivities, excluding any instances where no network existed in a simulated RVE.

Conductivity moving average convergence for a single set of simulation parameters (RVE cubic length, weight fraction CB, etc.), determined by a standardized convergence criteria, was found to require more than 500 conductive RVEs. After such realization, a single simulation parameter (RVE cubic length) was increased and the same conductivity convergence procedure was performed. This process was repeated with increasingly larger RVEs, revealing a dependence of converged average conductivity on the overall size of the simulated RVEs. An exponential function was found to be in good agreement with the converged average conductivity vs. RVE cubic length trend, with negligible RVE cubic length influence on conductivity for RVE cubic lengths greater than 6200-nm.

The serial model program runtimes at such RVEs scales were impractical. RVE generation via the serial random placement algorithm was found to be the most computationally expensive subroutine of the program. Load distributed and pseudo-parallelized particle placement algorithms were developed as a consequence. A successful pseudo-parallelization scheme consisting of interdigitated sub-RVEs and BVs was detailed. Investigation on the effect of parallelization on converged average conductivity found slight variation between serial and pseudo-parallel models. Comparison of the distribution of reported conductivities from serial and pseudo-parallel models revealed a positive skew in the pseudo-parallel data, while the mode of the distributions were found to be in good agreement. Improvements in computational efficiency

were realized, and pseudo-parallel model predictions were in agreement with the exponential convergence prediction from the serial data.

Early experimental model fidelity validation efforts revealed drastic differences between simulated RVEs and comparable physical CPC specimens. Agglomeration features realized in experimental samples, discussed in Chapter 3, prompted further model particle placement algorithm development. Multiple agglomeration inducing schemes were tested and found to produce RVEs containing more realistic agglomeration features through random coordinate generation and forced agglomeration placement rejections/replacements. Such particle replacements drastically decreased simulation efficiency, and prompted further model evolution.

An overhaul of the placement algorithm, using an index-mapping scheme, dramatically improved simulation efficiency. Placement of single spherical particles via random seeding and forced agglomeration was found to produce agglomerates with tailorable size and distribution. Renderings of such RVEs revealed agglomerates with consistently spherical geometries. Coincident with this realization, literature regarding the fractal nature of CB aggregates and spherical element aggregate modeling schemes was discovered.

The model was further developed to generate RVEs containing fractal aggregate structures. Monodisperse, spherical element-based, fractal aggregate coordinate files were generated using FracVal, an open-source program discovered in the literature. The stochastic modeling program accesses the aggregate coordinate files and subsequently generates RVEs with varying dispersion characteristics. User-defined variables pertaining to aggregate placement randomization and agglomeration are introduced for tailoring RVE dispersion. The renderings of the resulting index-mapped RVEs exhibited the most realistic agglomeration features modeled yet, all while vastly improving particle placement algorithm efficiency.

5.1.2. Chapter 3

Experimental methods for validating the fidelity of the final iteration of the stochastic modeling program were presented. CPC samples consisting of a two-part epoxy system and specialty conductive CB, prepared via ultrasonic homogenization and calendaring using a 3-roll mill, were investigated for determining the influence of preparation parameters on resulting dispersion characteristics of cured samples.

The CB variety (Vulcan © XC Max 22) used in this study was characterized via TEM to validate the manufacturer's specifications of average particle diameter (approximately 30-nm), and the resulting measured diameters were found in agreement. Dispersion characteristics of cured CPC mixtures sandwiched between glass microscopy slides were investigated via optical microscopy. Initial investigation of sandwiched mixtures revealed CB smearing and agglomerations that were vastly different than simulated volumes.

Estimation of the thicknesses of the sandwiched films was attempted unsuccessfully by freeze-fracturing samples and observing fractured cross-sections via optical microscopy. Surface profilometry was pursued as an alternative thickness measurement system. Cured samples were sent to Filmetrics for examination via optical profilometry. Resulting film measurements concluded that the thickness of the films produced via the sandwich method varied from 0.1 to 5 micron. Profilometry was identified as a preferred measurement approach.

To produce CPC films with more consistent topographies, a spin coater was created using a spare HDD and 3D printed parts. Initial microscopy images of spin coated samples revealed clearly defined agglomerates of sizes that were replicable via preliminary simulation attempts. CPC film sample substrates were adapted to improve the repeatability and accuracy of film thickness measurement using the stylus profilometer. The inherent error of the new measurement

system was quantified as less than 10%. Pooling of the CPC mixture on the substrates was realized in the first spin coating attempts. To combat this phenomenon, plasma cleaning was performed on the substrates and a photopolymer resin was incorporated into the spun mixtures to reduce film mobility during curing using high intensity UV-light.

The relationship between film thickness and optical dispersion characteristics were qualitatively assessed. Trends in agglomerate growth, realized in increasingly thicker experimental samples, was replicated using the final iteration of the stochastic modeling program. The effects of varied mixture homogenization energies on the dispersion characteristics of resulting CPC films were investigated. Microscopy images of poorly dispersed and very well dispersed samples, taken at high magnifications (100x), revealed exceedingly similar agglomerate distributions, while microscopy imaging at lower magnifications (10x) revealed drastic differences in agglomeration. Filtering data to remove noise, differences in average agglomerate area between samples of varied mixture energies were quantified.

For increasingly mixed samples, the average agglomerate area reported from image analysis data appeared to converge. These observations support the theoretical and numerical predictions of aggregate dispersion limits reported by Asylbekov *et al* [99]. Simulated RVEs with comparable dimension and constituent concentrations were generated for comparison to imaged films. Statistical analysis of simulated images was performed via the ImageJ Particle Analysis algorithm, recording shape descriptor statistics and agglomerate area distributions. Initial model parameter tuning was performed. Simulation parameters were varied to show the ability of the stochastic modeling program to generate RVEs spanning a wide range of agglomerate statistics.

5.1.3. Chapter 4

The development of experimental methods for characterizing the electromechanical properties of CB and phenolic resin CPC materials were presented. The purpose of the development of such methods is to support efforts to improve current models for bettering understanding of the underlying physics behind the experimentally observed behaviors of these materials.

Injection molding was examined as a simple method for manufacturing CPC samples of consistent geometry containing weight concentrations of CB ranging from 0.1% to 5%. Electrodes were created by adhering copper wire to injection-molded samples with conductive silver epoxy. The resulting transducers were found to be conductive at CB weight loadings of approximately 3.5%. The contact resistances of pasted electrodes were found to be sensitive to handling. Embedding copper wicking into the samples during curing was found to create more consistent electrical contacts. However, the incorporation of the copper wicking in the injection mold stack negatively affected the consistency of the sample geometries produced.

PCBs were explored as candidate substrates upon which CPC mixtures could be deposited for creation of CPC transducers. An automated SLBL apparatus was developed deposition of CPC mixtures. Parameters for SLBL apparatus deposition, including airbrush input air pressure, translational speed, and number of passes, were systematically investigated. The solder masks of the PCBs were found to be highly hydrophobic, resulting in pooling of the mixture during curing. By removing the surface solder mask layer, more consistent CPC films were created. The contact resistances between the CPC mixtures and the copper pads upon which the CPCs were deposited were found to be much greater than those estimated from samples with embedded copper wicking electrodes. Additionally, the peel strength of the CPC/pad interface

was found to be weak, and sample resistances were found to vary significantly after handling the substrate.

Standard printer paper was found to exhibit little to no pooling during SLBL deposition. A linear relationship between the total number of spray passes and the resulting thickness of the CPC films deposited on paper substrates was observed. CF tows were taped to paper substrates in parallel to serve as electrodes for CPC electromechanical interrogation. The resulting transducers were adhered to aluminum tensile specimens and were subjected to uniaxial tensile strain via a hydraulic load frame while monitoring changes in sample resistances. The paper substrate transducers were found to exhibit piezoresistive behaviors for sensors composed of 3.25% by weight CB.

To improve CPC transducer geometry, a room-temperature casting method was developed. 3D printed structures were used to create flexible molds out of silicon epoxy. The resulting molds were used to create dogbone-shaped specimens consistent with the specifications of ASTM D638-14. The molds were designed with slots for CF tows to be embedded in parallel about the gauge length of the dogbone-shaped specimens. CPC samples composed of 3.15% by weight CB were cast using the flexible molds, and subjected to uniaxial strain tests. The average relative change of sample resistance with respect to strain for all samples was calculated and compared to predictions of the stochastic model and a popular analytical model from the literature.

5.2. Key contributions of the dissertation

The following bulleted list summarizes the primary contributions that the research presented in this dissertation provides for the structural health monitoring and materials science engineering disciplines regarding carbon-based nanocomposite technologies and applications.

- Chapter 1 provides an extensive literature review of the state-of-the-art in structural health monitoring transducer development and practical considerations for deployment in composite structural designs. Recent research in the development of nanoparticle-based composite transducers is introduced. The need for advanced predictive tools and characterization methods are highlighted, and recent efforts reported in the literature to address such needs are presented.
- Chapter 2 presents a stochastic modeling program for the prediction of the electromechanical properties of spherical element-based CPC materials. The development of the model is discussed in great detail, from the earliest iterations of the program to its final form. The relationship between the cubic length of the RVE and the predicted electromechanical properties, for simulations of constant physical composition, was discovered in early stages of model development, which motivated the development of more efficient computational algorithms. Methods of simulation parallelization are presented, and the effects of parallelization on model fidelity are quantified. The predictions for CPC electrical conductivity were found to converge at a RVE cubic length of approximately 6200-nm, considering perfect dispersion. The fidelity of the perfect dispersion RVEs was determined unsatisfactory. The final iteration of the stochastic modeling program, developed on the idea of forced agglomeration, was found to be vastly more efficient than parallelization schemes and allowed for RVEs of high fidelity to be generated.
- Chapter 3 presents the development of a precise and repeatable method for characterizing dispersion in CPC mixtures for the tuning and improvement of stochastic model fidelity. The characteristics of the conductive CB modeled in Chapter 2 are examined via TEM to

validate the manufacturer's specifications. Spin coating was found to be a precise and repeatable means of preparing CPC films with optical characteristics favorable for dispersion characterization via optical microscopy. CPC mixtures prepared with various dispersion energies were found to produce films with vastly different agglomeration characteristics, the differences of which were most profound at lower magnifications. Microscopy images at higher magnifications revealed complex geometries that were characterized using ImageJ particle analysis shape descriptor statistics. By tuning simulation parameters, comparable RVEs were generated via the stochastic modeling program.

- Chapter 4 presents a precise and repeatable method for the electromechanical characterization of physical CPC specimens for comparison to predictions from the stochastic modeling program. Multiple attempted experimental methods were found to be lacking, and the realization of the shortcomings of those methods are discussed in detail. A highly repeatable sample preparation method was realized by casting dogbone-shaped CPC specimens via flexible silicon molds. Internal conductive network characterization was achieved via the incorporation of carbon fiber tows at precise locations along the gauge length during the sample casting process. Dogbone-shaped specimens were then subjected to a variety of uniaxial tensile tests while monitoring their electrical properties. The electromechanical responses are compared directly to stochastic modeling program and analytical model predictions. Stochastic model parameters, such as the polymer barrier height and interparticle contact resistance, are adjusted to produce simulated predictions in agreement with the experimental data.

5.3. Recommendations for future work

The following bulleted list presents recommendations for future works inspired by the research presented in this dissertation and the experiences of the author.

- The final iteration of the stochastic modeling program was developed with the goal of modeling a CPC composed of a CB variety. This was accomplished by defining all CB elements in the model to have a spherical diameter equal to the average diameter reported by the manufacturer. From the TEM characterization images, the CB variety was found to be polydisperse. The architecture of the code was designed to allow for more complex systems to be modeled, such as systems containing polydisperse spherical elements. The influence of element polydispersity on the electromechanical properties of simulated CPCs can easily be quantified using the stochastic modeling program detailed in this dissertation.
- The fidelity of the final iteration of the stochastic modeling program was experimentally validated by the manufacture of CPC thin films containing a single variety of CB filler at a constant weight concentration. The thickness of the experimental films was minimized to reduce overall simulation times needed to produce RVEs for statistical comparisons. The model's fidelity should be explored further to validate the scalability of the predictive tool for materials of thicknesses greater than 2 micron. Additionally, other varieties of CB filler should be characterized, modeled, and experimentally examined to determine the model's ability to accurately represent other CB CPC compositions.
- The experimental characterization of CPC dogbone-shaped specimens presented in this dissertation was limited to simple uniaxial tensile tests to determine piezoresistive characteristics for stochastic model tuning. During such experiments, non-recoverable strain deformation and creep were observed. These phenomena were accompanied by

permanent changes in CPC conductivity and piezoresistivity. Understanding the sources of influence for these permanent changes in CPC conductive networks is crucial for the development of fatigue sensing CPC transducers. The high-fidelity RVEs generated by the stochastic model provide a direct approach to understanding such phenomena. Simulated RVEs should be adapted for finite element investigations of CPC plastic deformation and creep. Additional experimental efforts for quantifying fatigue influence on electromechanical properties of modeled CB CPCs will be necessary to support such numerical studies.

APPENDIX A - CPC ELECTROMECHANICAL CHARACTERIZATION DATA

Tabulated Experimental Piezoresistivity Data (Chapter 4)						
Mix Energy	**Sample No:**	**ΔR(ε) slope**	**ΔR(σ) slope**	**σ(ε) slope**	**Pristine R [kΩ]**	**Resistivity [Ω-m]**
100-kJ	14	8.209	5.40E-04	6.59E-05	332.8	0.2936
	17	7.531	5.75E-04	7.63E-05	438.5	0.3868
	18	8.116	4.87E-04	6.00E-05	404.3	0.3567
	19	7.428	4.95E-04	6.66E-05	430.6	0.3799
	20	7.900	4.84E-04	6.10E-05	269.4	0.2376
	21	6.694	3.98E-04	5.94E-05	157	0.1385
	22	8.512	4.62E-04	5.42E-05	273.5	0.2413
	23	9.781	4.10E-04	4.19E-05	213.1	0.1880
	24	8.473	4.10E-04	4.83E-05	187.6	0.1655
	25	7.460	4.25E-04	5.69E-05	254.9	0.2249
	Average	8.010	4.69E-04	5.90E-05	296.17	0.2613
	Std. Dev.	0.792	5.62E-05	9.20E-06	96.10	0.0848
	Std. Dev. (%)	9.88%	12.00%	15.57%	32.45%	32.45%
50-kJ	26	8.201	4.93E-04	6.01E-05	2431	2.1445
	27	9.878	5.20E-04	5.25E-05	1708	1.5023
	28	8.682	5.53E-04	6.37E-05	2388	2.1048
	29	10.216	5.51E-04	5.39E-05	2106	1.8578
	30	5.978	5.74E-04	9.59E-05	2529	2.2309
	31	8.441	5.39E-04	6.38E-05	2039	1.7987
	Average	8.566	5.38E-04	6.50E-05	2200	1.9398
	Std. Dev.	1.372	2.59E-05	1.45E-05	281.0	0.2490
	Std. Dev. (%)	16.02%	4.82%	22.32%	12.77%	12.83%

Figure 39 - Tabulated experimental data from uniaxial tensile tests of cast CPC specimens of varying dispersion characteristics, referenced in Section 4.2.

Bibliography

1. Giurgiutiu V (2015) Structural health monitoring of aerospace composites. Academic Press, London
2. Boller C (2009) Structural health monitoring: an introduction and definitions. Encycl Struct Heal Monit - Chapter 1. https://doi.org/10.1111/j.1743-6109.2005.20230.x
3. Ostachowicz W, Kudela P, Krawczuk M, Zak A (2015) Guided Waves in Structures for SHM: The Time-Domain Spectral Element Method. Academic Press, London
4. Giurgiutiu V (2014) Structural Health Monitoring with Piezoelectric Wafer Active Sensors. Elsevier
5. de Souza Rabelo D, Hobeck JD, Inman DJ, et al (2017) Real-time structural health monitoring of fatigue crack on aluminum beam using an impedance-based portable device. J Intell Mater Syst Struct 28:3152–3162. https://doi.org/10.1177/1045389X17705213
6. Nasrollahi A, Deng W, Ma Z, Rizzo P (2018) Multimodal structural health monitoring based on active and passive sensing. Struct Heal Monit 17:395–409. https://doi.org/10.1177/1475921717699375
7. Tang H-Y, Winkelmann C, Lestari W, La Saponara V (2011) Composite Structural Health Monitoring Through Use of Embedded PZT Sensors. J Intell Mater Syst Struct 22:739–755. https://doi.org/10.1177/1045389X11406303
8. Kersey AD, Davis MA, Patrick HJ, et al (1997) Fiber grating sensors. J Light Technol 15:1442–1463. https://doi.org/10.1109/50.618377
9. Alvarez-Botero G, Baron FE, Cano CC, et al (2017) Optical sensing using fiber bragg gratings: fundamentals and applications. IEEE Instrum Meas Mag 20:33–38.

https://doi.org/10.1109/MIM.2017.7919131

10. Okabe Y, Yashiro S, Kosaka T, Takeda N (2000) Detection of transverse cracks in CFRP composites using embedded fiber Bragg grating sensors. Smart Mater Struct 9:832–838. https://doi.org/10.1088/0964-1726/9/6/313

11. Mizutani T, Okabe Y, Takeda N (2003) Quantitative evaluation of transverse cracks in carbon fiber reinforced plastic quasi-isotropic laminates with embedded small-diameter fiber Bragg grating sensors. Smart Mater Struct 12:898–903. https://doi.org/10.1088/0964-1726/12/6/006

12. Wang D, Chung DDL (2013) Through-thickness piezoresistivity in a carbon fiber polymer-matrix structural composite for electrical-resistance-based through-thickness strain sensing. Carbon N Y 60:129–138. https://doi.org/10.1016/j.carbon.2013.04.005

13. Angelidis N, Khemiri N, Irving PE (2005) Experimental and finite element study of the electrical potential technique for damage detection in CFRP laminates. Smart Mater Struct 14:147–154. https://doi.org/10.1088/0964-1726/14/1/014

14. Swait TJ, Jones FR, Hayes SA (2012) A practical structural health monitoring system for carbon fibre reinforced composite based on electrical resistance. Compos Sci Technol 72:1515–1523. https://doi.org/10.1016/j.compscitech.2012.05.022

15. Baltopoulos A, Polydorides N, Pambaguian L, et al (2013) Damage identification in carbon fiber reinforced polymer plates using electrical resistance tomography mapping. J Compos Mater 47:3285–3301. https://doi.org/10.1177/0021998312464079

16. Nasir MA, Akram H, Khan ZM, et al (2015) Smart sensing layer for the detection of damage due to defects in a laminated composite structure. J Intell Mater Syst Struct 26:2362–2368. https://doi.org/10.1177/1045389X14554138

17. Nag-Chowdhury S, Bellegou H, Pillin I, et al (2016) Non-intrusive health monitoring of infused composites with embedded carbon quantum piezo-resistive sensors. Compos Sci Technol. https://doi.org/10.1016/j.compscitech.2016.01.004

18. Liang J-Z, Yang Q-Q (2018) Effects of carbon black content and size on conductive properties of filled high-density polyethylene composites. Adv Polym Technol 37:2238–2245. https://doi.org/10.1002/adv.21882

19. Paszkiewicz S, Szymczyk A, Zubkiewicz A, et al (2020) Enhanced Functional Properties of Low-Density Polyethylene Nanocomposites Containing Hybrid Fillers of Multi-Walled Carbon Nanotubes and Nano Carbon Black. Polymers (Basel) 12:1356. https://doi.org/10.3390/polym12061356

20. Mysiukiewicz O, Gospodarek B, Ławniczak P, Sterzyński T (2018) Influence of the conductive network creation on electrical, rheological, and mechanical properties of composites based on LDPE and EVA matrices. Adv Polym Technol 37:3542–3551. https://doi.org/10.1002/adv.22138

21. Czech Z, Pełech R, Kowalczyk A, et al (2011) Electrically conductive acrylic pressure-sensitive adhesives containing carbon black. PJCT 13:77–81. https://doi.org/10.2478/v10026-011-0053-2

22. Castro Martínez M, Hernández López S, Vigueras Santiago E (2015) Relationship between Polymer Dielectric Constant and Percolation Threshold in Conductive Poly(styrene)-Type Polymer and Carbon Black Composites. J Nanomater 2015:1–9. https://doi.org/10.1155/2015/607896

23. Albright T, Hobeck JD (2019) Stochastic modeling of composite strain and fatigue sensing elements. In: Wang K-W, Sohn H, Huang H, Lynch JP (eds) Sensors and Smart

Structures Technologies for Civil, Mechanical, and Aerospace Systems 2019. SPIE, p 42

24. Zheng Y, Li Y, Li Z, et al (2017) The effect of filler dimensionality on the electromechanical performance of polydimethylsiloxane based conductive nanocomposites for flexible strain sensors. Compos Sci Technol 139:64–73. https://doi.org/10.1016/j.compscitech.2016.12.014
25. Kim JH, Hong JS, Ishigami A, et al (2020) Effect of Melt-Compounding Protocol on Self-Aggregation and Percolation in a Ternary Composite. Polymers (Basel) 12:3041. https://doi.org/10.3390/polym12123041
26. SiIva MP, Cavalcanti SN, Alves AM, et al (2021) Evaluation of the rheological and electrical percolation of high-density polyethylene/carbon black composites using mathematical models. Polym Eng Sci 61:2105–2116. https://doi.org/10.1002/pen.25738
27. Zhu H, Wang F, Wang L, Wang Y (2018) Influences of compression cycles on piezocapacitive effect of carbon black filled silicone rubber composite. Sensors Actuators A Phys 271:192–200. https://doi.org/10.1016/j.sna.2017.12.059
28. Hernandez JA, Kedir N, Lim BH, et al (2020) An experimental study on the piezoresistive and mechanical behavior of carbon nanocomposites subject to high-rate elastic loading. Compos Sci Technol 198:108285. https://doi.org/10.1016/j.compscitech.2020.108285
29. Kumar V, Lee G, Singh K, et al (2020) Structure-property relationship in silicone rubber nanocomposites reinforced with carbon nanomaterials for sensors and actuators. Sensors Actuators A Phys 303:111712. https://doi.org/10.1016/j.sna.2019.111712
30. Brunella V, Rossatto BG, Scarano D, Cesano F (2021) Thermal, Morphological, Electrical Properties and Touch-Sensor Application of Conductive Carbon Black-Filled Polyamide Composites. Nanomaterials 11:3103. https://doi.org/10.3390/nano11113103

31. Li X, Deng H, Zhang Q, et al (2016) The effect of DBP of carbon black on the dynamic self-assembly in a polymer melt. RSC Adv 6:24843–24852. https://doi.org/10.1039/C5RA28118K

32. Dal Lago E, Cagnin E, Boaretti C, et al (2019) Influence of Different Carbon-Based Fillers on Electrical and Mechanical Properties of a PC/ABS Blend. Polymers (Basel) 12:29. https://doi.org/10.3390/polym12010029

33. Alves AM, Cavalcanti SN, Silva MP, et al (2021) Electrical, rheological, and mechanical properties copolymer/carbon black composites. J Vinyl Addit Technol 27:445–458. https://doi.org/10.1002/vnl.21818

34. Bertolini MC, Dul S, Lopes Pereira EC, et al (2021) Fabrication and characterization of piezoresistive flexible pressure sensors based on poly(vinylidene fluoride)/thermoplastic polyurethane filled with carbon black-polypyrrole. Polym Compos 42:6621–6634. https://doi.org/10.1002/pc.26327

35. Duan L, Spoerk M, Wieme T, et al (2019) Designing formulation variables of extrusion-based manufacturing of carbon black conductive polymer composites for piezoresistive sensing. Compos Sci Technol 171:78–85. https://doi.org/10.1016/j.compscitech.2018.12.009

36. Poudel A, Karode N, McGorry P, et al (2019) Processing of nanocomposites using supercritical fluid assisted extrusion for stress/strain sensing applications. Compos Part B Eng 165:397–405. https://doi.org/10.1016/j.compositesb.2019.01.098

37. Choi H-J, Kim MS, Ahn D, et al (2019) Electrical percolation threshold of carbon black in a polymer matrix and its application to antistatic fibre. Sci Rep 9:6338. https://doi.org/10.1038/s41598-019-42495-1

38. Wang Z, Guan X, Huang H, et al (2019) Full 3D Printing of Stretchable Piezoresistive Sensor with Hierarchical Porosity and Multimodulus Architecture. Adv Funct Mater 29:1807569. https://doi.org/10.1002/adfm.201807569

39. Tirado-Garcia I, Garcia-Gonzalez D, Garzon-Hernandez S, et al (2021) Conductive 3D printed PLA composites: On the interplay of mechanical, electrical and thermal behaviours. Compos Struct 265:113744. https://doi.org/10.1016/j.compstruct.2021.113744

40. Sekertekin Y, Bozyel I, Gokcen D (2020) A Flexible and Low-Cost Tactile Sensor Produced by Screen Printing of Carbon Black/PVA Composite on Cellulose Paper. Sensors 20:2908. https://doi.org/10.3390/s20102908

41. Wang Y, Sekine T, Takeda Y, et al (2021) Deep Eutectic Solvent Induced Porous Conductive Composite for Fully Printed Piezoresistive Pressure Sensor. Adv Mater Technol 6:2100731. https://doi.org/10.1002/admt.202100731

42. Devaraj H, Yellapantula K, Stratta M, et al (2019) Embedded piezoresistive pressure sensitive pillars from piezoresistive carbon black composites towards a soft large-strain compressive load sensor. Sensors Actuators A Phys 285:645–651. https://doi.org/10.1016/j.sna.2018.12.006

43. Zhou P, Liao Y, Li Y, et al (2019) An inkjet-printed, flexible, ultra-broadband nanocomposite film sensor for in-situ acquisition of high-frequency dynamic strains. Compos Part A Appl Sci Manuf 125:105554. https://doi.org/10.1016/j.compositesa.2019.105554

44. Liu K, Yu J, Li Y, et al (2019) Carbon Black from Diesel Soot for High-Performance Wearable Pressure Sensors. Adv Mater Technol 4:1900475. https://doi.org/10.1002/admt.201900475

45. Hu J, Yu J, Li Y, et al (2020) Nano Carbon Black-Based High Performance Wearable Pressure Sensors. Nanomaterials 10:664. https://doi.org/10.3390/nano10040664

46. Albright TB, Hobeck JD (2020) Development of Manufacturing and Characterization Methods for Carbon Black-Based Conductive Polymer Composite Sensors. In: Volume 3: Advanced Materials: Design, Processing, Characterization, and Applications. American Society of Mechanical Engineers

47. Narongthong J, Wießner S, Hait S, et al (2020) Strain-rate independent small-strain-sensor: Enhanced responsiveness of carbon black filled conductive rubber composites at slow deformation by using an ionic liquid. Compos Sci Technol 188:107972. https://doi.org/10.1016/j.compscitech.2019.107972

48. Kim JH, Hong JS, Ahn KH (2022) Secondary polymer-induced particle aggregation and its rheological, electrical, and mechanical effects on PLA-based ternary composites. J Rheol (N Y N Y) 66:275–291. https://doi.org/10.1122/8.0000366

49. Wu L, Yao D, Gao X, et al (2020) An efficient flexible strain sensor based on anhydride-grafted styrene-butadiene-styrene triblock copolymer/carbon black: enhanced electrical conductivity, sensitivity and stability through solvent swelling. Smart Mater Struct 29:125018. https://doi.org/10.1088/1361-665X/abc26d

50. Yi Y, Samara A, Wang B (2021) A new approach for an ultra-thin piezoresistive sensor based on solidified carbon ink film. J Mater Sci 56:607–614. https://doi.org/10.1007/s10853-020-05309-8

51. Zhu J, Wang H, Zhu Y (2018) A flexible piezoresistive carbon black network in silicone rubber for wide range deformation and strain sensing. J Appl Phys 123:034505. https://doi.org/10.1063/1.5006523

52. Liang T, Zou X, Pal RK, et al (2020) Tunable Electrical Properties of Embossed, Cellulose-Based Paper for Skin-like Sensing. ACS Appl Mater Interfaces 12:51960–51968. https://doi.org/10.1021/acsami.0c15073

53. Devaraj H, Giffney T, Petit A, et al (2018) The Development of Highly Flexible Stretch Sensors for a Robotic Hand. Robotics 7:54. https://doi.org/10.3390/robotics7030054

54. Stassi S, Cauda V, Canavese G, Pirri C (2014) Flexible Tactile Sensing Based on Piezoresistive Composites: A Review. Sensors 14:5296–5332. https://doi.org/10.3390/s140305296

55. Chen J, Zhu Y, Huang J, et al (2021) Advances in Responsively Conductive Polymer Composites and Sensing Applications. Polym Rev 61:157–193. https://doi.org/10.1080/15583724.2020.1734818

56. Zheng S, Huang S, Ren D, et al (2014) Preparation and characterization of isotactic polypropylene/high-density polyethylene/carbon black conductive films with strain-sensing behavior. J Appl Polym Sci. https://doi.org/10.1002/app.40686

57. Høyer H, Knaapila M, Kjelstrup-Hansen J, et al (2012) Individual strings of conducting carbon cones and discs in a polymer matrix: Electric field-induced alignment and their use as a strain sensor. J Polym Sci Part B Polym Phys 50:477–483. https://doi.org/10.1002/polb.23031

58. Cetin MS, Karahan Toprakci HA (2021) Flexible electronics from hybrid nanocomposites and their application as piezoresistive strain sensors. Compos Part B Eng 224:109199. https://doi.org/10.1016/j.compositesb.2021.109199

59. Grenquist EA (1931) The Dispersion of Gas Black and the Physical Properties of Rubber Mixtures. Rubber Chem Technol 4:29–38. https://doi.org/10.5254/1.3547475

60. Boonstra BB, Medalia AI (1963) Effect of Carbon Black Dispersion on the Mechanical Properties of Rubber Vulcanizates. Rubber Chem Technol 36:115–142. https://doi.org/10.5254/1.3539530

61. Huang J-C (2002) Carbon black filled conducting polymers and polymer blends. Adv Polym Technol 21:299–313. https://doi.org/10.1002/adv.10025

62. Shang S, Yue Y, Wang X (2016) Piezoresistive strain sensing of carbon black /silicone composites above percolation threshold. Rev Sci Instrum 87:. https://doi.org/10.1063/1.4973274

63. Luheng W, Tianhuai D, Peng W (2009) Influence of carbon black concentration on piezoresistivity for carbon-black-filled silicone rubber composite. Carbon N Y 47:3151–3157. https://doi.org/10.1016/j.carbon.2009.06.050

64. Moriche R, Prolongo SG, Sánchez M, et al (2015) Morphological changes on graphene nanoplatelets induced during dispersion into an epoxy resin by different methods. Compos Part B Eng 72:199–205. https://doi.org/10.1016/j.compositesb.2014.12.012

65. Akram S, Castellon J, Agnel S, et al (2021) Multilayer polyimide nanocomposite films synthesis process optimization impact on nanoparticles dispersion and their dielectric performance. J Appl Polym Sci 138:49715. https://doi.org/10.1002/app.49715

66. Nallabothula H, Bhattacharjee Y, Samantara L, Bose S (2019) Processing-Mediated Different States of Dispersion of Multiwalled Carbon Nanotubes in PDMS Nanocomposites Influence EMI Shielding Performance. ACS Omega 4:1781–1790. https://doi.org/10.1021/acsomega.8b02920

67. Al-Bahrani M, Cree A (2021) Micro-scale damage sensing in self-sensing nanocomposite material based CNTs. Compos Part B Eng 205:108479.

https://doi.org/10.1016/j.compositesb.2020.108479

68. Govindaraj P, Sokolova A, Salim N, et al (2021) Distribution states of graphene in polymer nanocomposites: A review. Compos Part B Eng 226:109353. https://doi.org/10.1016/j.compositesb.2021.109353

69. Ji SH, Lee D, Yun JS (2021) Experimental and theoretical investigations of the rheological and electrical behavior of nanocomposites with universal percolation networks. Compos Part B Eng 225:109317. https://doi.org/10.1016/j.compositesb.2021.109317

70. Sui G, Liu D, Liu Y, et al (2019) The dispersion of CNT in TPU matrix with different preparation methods: solution mixing vs melt mixing. Polymer (Guildf) 182:121838. https://doi.org/10.1016/j.polymer.2019.121838

71. Zare Y (2017) Evaluation of nanoparticle dispersion and its influence on the tensile modulus of polymer nanocomposites by a modeling method. Colloid Polym Sci 295:363–369. https://doi.org/10.1007/s00396-017-4016-x

72. Bakshi SR, Batista RG, Agarwal A (2009) Quantification of carbon nanotube distribution and property correlation in nanocomposites. Compos Part A Appl Sci Manuf 40:1311–1318. https://doi.org/10.1016/j.compositesa.2009.06.004

73. Jouault N, Dalmas F, Boué F, Jestin J (2012) Multiscale characterization of filler dispersion and origins of mechanical reinforcement in model nanocomposites. Polymer (Guildf) 53:761–775. https://doi.org/10.1016/j.polymer.2011.12.001

74. Toor A, So H, Pisano AP (2017) Improved Dielectric Properties of Polyvinylidene Fluoride Nanocomposite Embedded with Poly(vinylpyrrolidone)-Coated Gold Nanoparticles. ACS Appl Mater Interfaces 9:6369–6375.

https://doi.org/10.1021/acsami.6b13900

75. Suter M, Ergeneman O, Zürcher J, et al (2011) A photopatternable superparamagnetic nanocomposite: Material characterization and fabrication of microstructures. Sensors Actuators B Chem 156:433–443. https://doi.org/10.1016/j.snb.2011.04.078

76. Kang C, Xu J, Niu L, et al (2021) Quantitative evaluation of nanoparticle dispersion based on modeling methods and image analysis: A case study on <scp> nano-Sb $_2$ O $_3$ </scp> filled Poly (butylene terephthalate) composites. Polym Compos 42:3098–3113. https://doi.org/10.1002/pc.26042

77. Romyen N, Thongyai S, Praserthdam P (2010) Surfactant-dispersed carbon black in polyimide nanocomposites: Spectroscopic monitoring of the dispersion state in the polymer matrix. J Appl Polym Sci 115:1622–1629. https://doi.org/10.1002/app.31164

78. Verleysen E, De Temmerman P-J, Van Doren E, et al (2014) Quantitative characterization of aggregated and agglomerated titanium dioxide nanomaterials by transmission electron microscopy. Powder Technol 258:180–188. https://doi.org/10.1016/j.powtec.2014.03.010

79. Xie S, Harkin-Jones E, Shen Y, et al (2010) Quantitative characterization of clay dispersion in polypropylene-clay nanocomposites by combined transmission electron microscopy and optical microscopy. Mater Lett 64:185–188. https://doi.org/10.1016/j.matlet.2009.10.042

80. Fu X, Wang J, Ding J, et al (2013) Quantitative evaluation of carbon nanotube dispersion through scanning electron microscopy images. Compos Sci Technol 87:170–173. https://doi.org/10.1016/j.compscitech.2013.08.014

81. Yahya NZ, Rusop M (2012) Investigation on the Optical and Surface Morphology of Conjugated Polymer MEH-PPV:ZnO Nanocomposite Thin Films. J Nanomater 2012:1–4.

https://doi.org/10.1155/2012/793679

82. Voo R, Mariatti M, Sim L (2011) Properties of epoxy nanocomposite thin films prepared by spin coating technique. J Plast Film Sheeting 27:331–346. https://doi.org/10.1177/8756087911419745

83. Bunk JKG, Drechsler A, Friedel P, et al (2015) Nanoparticle Distribution in Three-Layer Polymer-Nanoparticle Composite Films: Comparison of Experiment and Theory. Part Part Syst Charact 32:123–131. https://doi.org/10.1002/ppsc.201400050

84. Yazdani H, Smith BE, Hatami K (2016) Multi-walled carbon nanotube-filled polyvinyl chloride composites: Influence of processing method on dispersion quality, electrical conductivity and mechanical properties. Compos Part A Appl Sci Manuf 82:65–77. https://doi.org/10.1016/j.compositesa.2015.12.005

85. Singh AR, Deshpande VD (2016) Processing and characterization of extruded PET and its r-PET and MWCNT nanocomposite thin films by spin coating. Bull Mater Sci 39:167–175. https://doi.org/10.1007/s12034-015-1116-4

86. Zaccardi F, Santonicola MG, Laurenzi S (2018) Quantitative assessment of nanofiller dispersion based on grayscale image analysis: A case study on epoxy/carbon nanocomposites. Compos Part A Appl Sci Manuf 115:302–310. https://doi.org/10.1016/j.compositesa.2018.10.003

87. Yourdkhani M, Hubert P (2013) Quantitative Dispersion Analysis of Inclusions in Polymer Composites. ACS Appl Mater Interfaces 5:35–41. https://doi.org/10.1021/am301459q

88. Shojaeiarani J, Bajwa DS, Stark NM (2018) Spin-coating: A new approach for improving dispersion of cellulose nanocrystals and mechanical properties of poly (lactic acid)

composites. Carbohydr Polym 190:139–147. https://doi.org/10.1016/j.carbpol.2018.02.069

89. Schneider S, Eppler F, Weber M, et al (2016) Multiscale dispersion-state characterization of nanocomposites using optical coherence tomography. Sci Rep 6:31733. https://doi.org/10.1038/srep31733

90. Carotenuto G, Her Y-S, Matijević E (1996) Preparation and Characterization of Nanocomposite Thin Films for Optical Devices. Ind Eng Chem Res 35:2929–2932. https://doi.org/10.1021/ie950721k

91. Yaklin MA, Duxbury PM, Mackay ME (2008) Control of nanoparticle dispersion in thin polymer films. Soft Matter 4:2441. https://doi.org/10.1039/b807565d

92. Quercia L, Loffredo F, Di Francia G (2005) Influence of filler dispersion on thin film composites sensing properties. Sensors Actuators B Chem 109:153–158. https://doi.org/10.1016/j.snb.2005.03.076

93. Abargues R, Abderrafi K, Pedrueza E, et al (2009) Optical properties of different polymer thin films containing in situ synthesized Ag and Au nanoparticles. New J Chem 33:1720. https://doi.org/10.1039/b900185a

94. Wong HC, Cabral JT (2010) Nanoparticle aggregation behaviour in polymer nanocomposites: bulk vs. thin films. J Phys Conf Ser 247:012046. https://doi.org/10.1088/1742-6596/247/1/012046

95. Albright TB, Hobeck JD (2021) High-fidelity stochastic modeling of carbon black-based conductive polymer composites for strain and fatigue sensing. J Mater Sci 56:6861–6877. https://doi.org/10.1007/s10853-020-05734-9

96. Feng Y, Zou H, Tian M, et al (2012) Relationship between dispersion and conductivity of

polymer nanocomposites: A molecular dynamics study. J Phys Chem B. https://doi.org/10.1021/jp305815r

97. Akram S, Castellon J, Kai Z, et al (2020) Dielectric properties and modeling of multilayer polyimide nanocomposite to highlight the impact of nanoparticles dispersion. IEEE Trans Dielectr Electr Insul 27:1238–1246. https://doi.org/10.1109/TDEI.2020.008697

98. Coupette F, Zhang L, Kuttich B, et al (2021) Percolation of rigid fractal carbon black aggregates. J Chem Phys 155:124902. https://doi.org/10.1063/5.0058503

99. Asylbekov E, Trunk R, Krause MJ, Nirschl H (2021) Microscale Discrete Element Method Simulation of the Carbon Black Aggregate Fracture Behavior in a Simple Shear Flow. Energy Technol 9:2000850. https://doi.org/10.1002/ente.202000850

100. Thostenson E, Li C, Chou T (2005) Nanocomposites in context. Compos Sci Technol 65:491–516. https://doi.org/10.1016/j.compscitech.2004.11.003

101. Torquato S (2002) Random Heterogeneous Materials. Springer New York, New York, NY

102. Torquato S, Stillinger FH (2010) Jammed hard-particle packings: From Kepler to Bernal and beyond. Rev Mod Phys 82:2633–2672. https://doi.org/10.1103/RevModPhys.82.2633

103. Jiao Y, Stillinger FH, Torquato S (2008) Modeling heterogeneous materials via two-point correlation functions. II. Algorithmic details and applications. Phys Rev E 77:031135. https://doi.org/10.1103/PhysRevE.77.031135

104. Donev A, Cisse I, Sachs D, et al (2004) Improving the Density of Jammed Disordered Packings Using Ellipsoids. Science (80-) 303:990–993. https://doi.org/10.1126/science.1093010

105. Afiqah N, Radzuan M, Sulong AB, Sahari J (2017) A review of electrical conductivity models for conductive polymer composite. Int J Hydrogen Energy.

https://doi.org/10.1016/j.ijhydene.2016.03.045

106. Stepashkina AS, Tsobkallo ES, Alyoshin AN (2014) Electrical conductivity modeling and research of polypropylene composites filled with carbon black. In: Journal of Physics: Conference Series

107. Soto M, Esteva M, Martínez-Romero O, et al (2015) Modeling percolation in polymer nanocomposites by stochastic microstructuring. Materials (Basel). https://doi.org/10.3390/ma8105334

108. Bao WS, Meguid SA, Zhu ZH, et al (2012) A novel approach to predict the electrical conductivity of multifunctional nanocomposites. Mech Mater. https://doi.org/10.1016/j.mechmat.2011.12.006

109. Matos MAS, Tagarielli VL, Baiz-Villafranca PM, Pinho ST (2018) Predictions of the electro-mechanical response of conductive CNT-polymer composites. J Mech Phys Solids. https://doi.org/10.1016/j.jmps.2018.02.014

110. Xiong ZY, Zhang BY, Wang L, et al (2014) Modeling the electrical percolation of mixed carbon fillers in polymer blends. Carbon N Y. https://doi.org/10.1016/j.carbon.2014.01.001

111. Consiglio R, Baker DR, Paul G, Stanley HE (2003) Continuum percolation thresholds for mixtures of spheres of different sizes. Phys A Stat Mech its Appl. https://doi.org/10.1016/S0378-4371(02)01501-7

112. Chen Y, Wang S, Pan F, Zhang J (2014) A numerical study on electrical percolation of polymer-matrix composites with hybrid fillers of carbon nanotubes and carbon black. J Nanomater. https://doi.org/10.1155/2014/614797

113. Essam JW (1980) Percolation theory. Reports Prog Phys 43:833–912.

https://doi.org/10.1088/0034-4885/43/7/001

114. Kirkpatrick S (1973) Percolation and Conduction. Rev Mod Phys 45:574–588. https://doi.org/10.1103/RevModPhys.45.574

115. Gao J-F, Li Z-M, Meng Q, Yang Q (2008) CNTs/ UHMWPE composites with a two-dimensional conductive network. Mater Lett 62:3530–3532. https://doi.org/10.1016/j.matlet.2008.03.053

116. Stauffer D, Aharony A (2018) Introduction To Percolation Theory. Taylor & Francis

117. Carmona F, Canet R, Delhaes P (1987) Piezoresistivity of heterogeneous solids. J Appl Phys 61:2550–2557. https://doi.org/10.1063/1.337932

118. Zhang X-W, Pan Y, Zheng Q, Yi X-S (2000) Time dependence of piezoresistance for the conductor-filled polymer composites. J Polym Sci Part B Polym Phys 38:2739–2749. https://doi.org/10.1002/1099-0488(20001101)38:21<2739::AID-POLB40>3.0.CO;2-O

119. Paredes-Madrid L, Matute A, Palacio C (2019) Understanding the effect of sourcing voltage and driving circuit in the repeatability of measurements in force sensing resistors (FSRs). Meas Sci Technol 30:115101. https://doi.org/10.1088/1361-6501/ab3307

120. Paredes-Madrid L, Palacio C, Matute A, Parra Vargas C (2017) Underlying Physics of Conductive Polymer Composites and Force Sensing Resistors (FSRs) under Static Loading Conditions. Sensors 17:2108. https://doi.org/10.3390/s17092108

121. Kalantari M, Dargahi J, Kövecses J, et al (2012) A New Approach for Modeling Piezoresistive Force Sensors Based on Semiconductive Polymer Composites. IEEE/ASME Trans Mechatronics 17:572–581. https://doi.org/10.1109/TMECH.2011.2108664

122. Ma HM, Gao X-L (2008) A three-dimensional Monte Carlo model for electrically

conductive polymer matrix composites filled with curved fibers. Polymer (Guildf) 49:4230–4238. https://doi.org/10.1016/j.polymer.2008.07.034

123. Law J, Rennie R (2015) Oxford Dictionary of Physics

124. Simmons JG (1963) Generalized Formula for the Electric Tunnel Effect between Similar Electrodes Separated by a Thin Insulating Film. J Appl Phys. https://doi.org/10.1063/1.1702682

125. Xu S, Rezvanian O, Peters K, Zikry MA (2011) Tunneling effects and electrical conductivity of CNT polymer composites. In: Materials Research Society Symposium Proceedings

126. Sun X, Song M (2009) Highly conductive carbon nanotube/polymer nanocomposites achievable? Macromol Theory Simulations. https://doi.org/10.1002/mats.200800091

127. Matsumoto M, Nishimura T (1998) Mersenne twister: a 623-dimensionally equidistributed uniform pseudo-random number generator. ACM Trans Model Comput Simul. https://doi.org/10.1145/272991.272995

128. Guennebaud G, Jacob B, others (2010) Eigen v3

129. Chi Chou P, J. Pagano N (1967) Elasticity : Tensor, Dyadic, and Engineering Approaches / P.C. Chou, N.J. Pagano.

130. Stukowski A (2009) Visualization and analysis of atomistic simulation data with OVITO–the Open Visualization Tool. Model Simul Mater Sci Eng 18:15012. https://doi.org/10.1088/0965-0393/18/1/015012

131. Manssen M, Weigel M, Hartmann AK (2012) Random number generators for massively parallel simulations on GPU. Eur Phys J Spec Top 210:53–71. https://doi.org/10.1140/epjst/e2012-01637-8

132. Lin Y, Wang F, Liu B (2018) Random number generators for large-scale parallel Monte Carlo simulations on FPGA. J Comput Phys 360:93–103. https://doi.org/10.1016/j.jcp.2018.01.029

133. Schneider CA, Rasband WS, Eliceiri KW (2012) NIH Image to ImageJ: 25 years of image analysis. Nat Methods 9:671–675. https://doi.org/10.1038/nmeth.2089

134. Donnet J-B, Bansal RC, Wang M-J (2018) Carbon Black. Routledge

135. Meakin P (1999) A Historical Introduction to Computer Models for Fractal Aggregates. J Sol-Gel Sci Technol 15:97–117. https://doi.org/10.1023/A:1008731904082

136. Morán J, Fuentes A, Liu F, Yon J (2019) FracVAL: An improved tunable algorithm of cluster–cluster aggregation for generation of fractal structures formed by polydisperse primary particles. Comput Phys Commun 239:225–237. https://doi.org/10.1016/j.cpc.2019.01.015

137. Mouhamad Y, Mokarian-Tabari P, Clarke N, et al (2014) Dynamics of polymer film formation during spin coating. J Appl Phys 116:123513. https://doi.org/10.1063/1.4896674

138. (2014) ASTM Standard D638-14. https://doi.org/https://dx.doi.org/10.1520/F1045-07